TECHNISCHE UNIVERSITÄT WIEN

DIPLOMARBEIT

Mechanical Bactericide by Biomimetics of the Nanopillars on Insect Wings

zur Erlangung des akademischen Grades

Diplom-Ingenieur

im Rahmen des Studiums

Biomedical Engineering - UE 066 453

eingereicht von

Richard W. van Nieuwenhoven

Matrikelnummer 1652322

Ausgeführt am Institut für Angewandte Physik
der Fakultät für Physik der Technischen Universität Wien

Betreuung
Associate Prof. Dipl.-Ing. Dr. techn. Ille C. Gebeshuber

Vienna, October 19, 2022 _____ _____
(Unterschrift Verfasser) (Unterschrift Betreuerin)

Contents

1 Abstract

1.1 Abstract

The antibacterial properties of cicada wings originate from hexagonal pillar-like nanostructures with species-dependent heights of approximately 330 nanometers and a tip spacing of about 188 nanometers. These multi functional nanostructures are also superhydrophobic and self-cleaning. This diploma thesis presents investigations of two New Zealand cicada species *Amphipsalta cingulata* and *Kikihia scutellaris*, the Austrian dragonfly *Sympetrum striolatum* as well as an US American cicada species *Magicicada septendecim* with various methods such as Atomic Force Microscopy, Scanning Electron Microscopy, and bacterial tests with live-dead staining. The surfaces investigated comprise the cicada wings themselves, negative replicas of the wings made with the molding material Polyvinyl siloxane and positive replicas in various resins. The main focus lies in establishing low-cost bioreplication techniques for the transfer of the antibacterial properties to man-made surfaces such as hospital surfaces, medical instruments, smartphone displays and door handles. A recent publication of Senevirathne and co-workers support my findings where I see challenges in using the nanopillars as bactericides.

1.2 Kurzfassung

Die antibakteriellen Eigenschaften von Zikadenflügeln beruhen auf hexagonal angeordneten säulenartigen Nanostrukturen mit artabhängigen Höhen von etwa 330 Nanometern und einem Spitzenabstand von etwa 188 Nanometern. Diese multifunktionalen Nanostrukturen sind außerdem superhydrophob und selbstreinigend. Diese Diplomarbeit stellt Untersuchungen an zwei neuseeländischen Zikadenarten *Amphipsalta cingulata* und *Kikihia scutellaris*, der österreichischen Libelle *Sympetrum striolatum* sowie einer US-amerikanischen Zikadenart *Magicicada septendecim* mit diversen Methoden wie Rasterkraftmikroskopie, Rasterelektronenmikroskopie und Bakterientests mit Lebend-Tot-Färbung. Die untersuchten Oberflächen umfassen die Zikadenflügel selbst, Negativabdrücken der Flügel aus dem Formstoff Polyvinylsiloxan und Positivabdrücken in verschiedenen Harzen. Das Hauptaugenmerk liegt auf der Entwicklung kostengünstiger Bioreplikationstechniken zur Übertragung der antibakteriellen Eigenschaften auf künstlich hergestellte Oberflächen wie Krankenhausoberflächen, medizinische Instrumente, Smartphondisplays und Türgriffe. Eine aktuelle Veröffentlichung von Senevirathne und Mitarbeitern unterstützt meine Zweifle an der Verwendung von Nanosäulen als Bakterizide.

2 Introduction

Nature has had billions of years experience in finding solutions for an uncountable amount of problems, where we have just started to scratch the surface. These solutions created recursive new problems to solve in an endless cycle of new natural-inventions, like the arms race (on the micrometer scale) in between bacteria and their virus foes [HWF20]. The resulting balance that nature presents us today is remarkably fragile and stable at the same time but it is always self sustaining in itself. Humankind can learn so much from Nature's solutions to base our future more on local resources and less dependent on scarce resources and energy intensive procedures.

Julian Vincent noted "*Biomimetics is the technological outcome of the act of borrowing or stealing ideas from nature*" [Vin01].

Probably biomimetics is as old as humankind, even if it is challenging to prove individual cases that date back that long (Fig. 3). One of the legends of the invention of the umbrella which dates back to approx. 2000 before the current era (BCE). By this legend, big lotus leaves worn on children's heads inspired the creation of the umbrella, so raindrops rolled down from the convex side.

One of the most prominent scientists in early history was Leonardo da Vinci (1452–1519). His keen observations of Nature lead to various studies on how to imitate Nature's ingenuity. For example, the "flying machines" sheets were among his most ingenious inventions, even if it took another few hundred years before the vision went into realisation (Fig. 2)[Vin80].

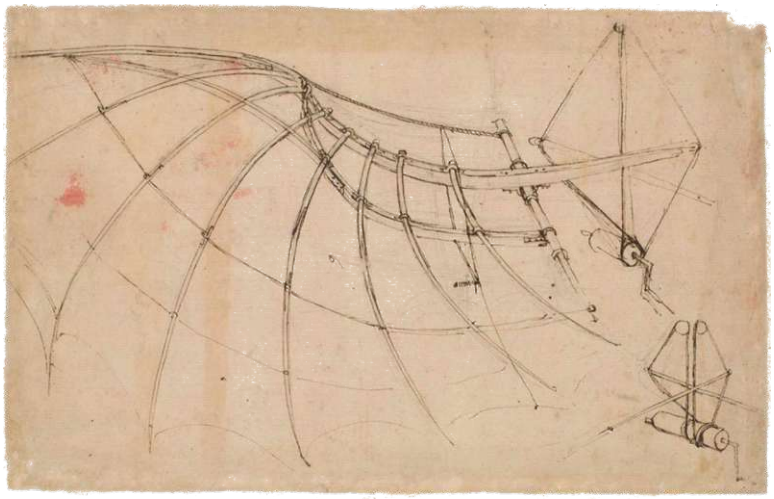

Fig. 2: Recto sheet 858 (from the Sketches of Flying Machines) of the 12 Volume Codex Atlanticus (Atlantic Codex) dating from 1478 to 1519, written by Leonardo da Vinci [Vin80].

Fig. 3: The ancient umbrella a biomimetic innovation [Chi13]?

Technological developments went more in another direction during the industrial revolution, allegiantly to surpass the possibilities nature offers. However, conservative technologies came at a price by ignoring the ecological costs of resources and sustainability. Only in recent history the concept of biomimetics became more and more prominent. Otto Schmitt reintroduced this concept in 1957 by changing the standard view of biophysics by approaching problems from their biological side [Vin+06]. Schmitt used the term "biomimetic" in the title of one of his papers in 1969 [Sch69]. The term "Biomimicry" appeared as early as 1982 [Mer82]. Biomimicry was popularized by scientist and author Janine Benyus in her 1997 book "Biomimicry: Innovation

Inspired by Nature" [Ben97]. Benyus added the focus on sustainability as one of the motivators for biologically inspired design. The biomimetics term is used in this diploma thesis as an umbrella term for all biologically inspired design phrases. The interested reader is referred to [DG13] for further reading on the various terms.

In modern times biomimetics slowly began its revival. A famous modern example of the return to biomimetics is the invention inspired by the seeds of the burdock plant. It was Nature's ingenius solution to transport the seeds to new breading grounds by hooking them up to the fur of passing animals. The massive amount of minuscule hooks can hold the seeds attached to any hairy material (Fig. 5). George de Mestral used this idea as an inspiration for his Velcro invention that is now part of our every day lives [Mes55]. The vast applications of this relatively simple biomimetic example are almost unimaginable.

Fig. 4: Stickybot walks vertically on windows [Aut+06]

Fig. 5: The minuscule hooks of Burdock seeds.

The fantastic properties of gecko feet inspired many researchers. Micrometer-sized lamellae with nano-substructures utilize the van der Waals forces (a weak attraction and repulsions force between atoms, molecules, and surfaces) to let the feet stick to the surface. The ingenuity of the lamella solution shows itself when the gecko wants to detach its feet. Almost without any force, the gecko can detach his feet again. The successful imitation of the gecko feet allows robots, like Stickybot in Fig. 4, to walk vertically on windows [Aut+06]. With the advancement of this technique, many more applications will be found for the gecko feet adhesion/detachment principle.

Biomimetics applications slowly enter every field of our lives, even in outer space Nature's solutions are the more effective solutions. So it is no wonder that the gecko feet now also found their way to outer space: the Gecko-Adhesive Gripper for force-free gripping in outer space [Cau+20]. In outer space, especially the forceless release is extremely helpful because of the weightless environment. As illustrated in Fig. 6, perching experiments conducted with the flight gecko gripper integrated onto an Astrobee unit at NASA Ames Research Center granite table facility [Cau+20].

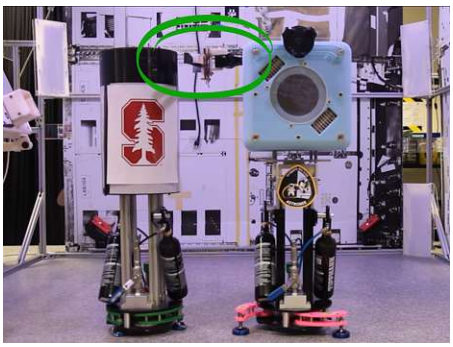

Fig. 6: Gecko-inspired adhesive grippers on the Astrobee Robotic Ground Test Bed [Cau+20]

2.1 Motivation

In 2020, my master studies in Biomedical Engineering at TU Wien were nearing finalization. In search of a research project on the topic of living materials, I met professor Ille C. Gebeshuber. She proposed a biomimetics project based on the bactericidal properties of cicada wings. The subject is another aspect of the wonders of Nature, so my agreement was just a formality.

2.2 Research animal ethics

As society changes, the focus on many topics changes. One of these focusing topics is animal welfare. In the last millennia, animal welfare has grown from a small minority topic to a much-discussed topic in the center of society. Science has had an ambivalent relation to animal welfare over history. Over 50 years ago, the 3Rs (Replacement, Reduction, and Refinement) principles were established in science. Many individuals helped to fill the 3Rs with life. Russell and Burch published the principles in "The Principles of Humane Experimental Technique" [RB59]. The 3Rs provide a framework for performing more humane animal research.

The global climate change debate opened a wide field of environmental topics for the broad public. The topic of animal self-awareness and the cognitive capability to suffer pain entered general public discussions. As more research was done on the cognitive capabilities of animals, many aspects of animal behavior and social life make it more and more challenging to draw an exact line separating the animals by different levels of cognitive awareness.

Insects were almost automatically excluded from this discussion and seen as automates with predictable behavior. Nevertheless, studies show that also these separations are not as clear as expected [BB20]. Insects are capable of learning [Duk08] and can have subjective experiences [KB16]. Though if insects cognitively feel pain is still not known [Ada16].

The precautionary principle in this diploma thesis is to assume that insects are sentient beings. As a prerequisite for this diploma thesis, it was agreed that no living beings would be killed.

This made specimen collection a challenge of its own. In Nature, insects are recycled extremely fast because of their high nutrient value. However, they can be collected at sites where many insects die, like lamps and windows. See below for a description of how the specific specimen were collected without killing the living insects for our study.

2.3 Mechanical bactericidal properties of insect wings

Insect wings are extensions of the exoskeleton. The evolution of insect wings is interestingly still in debate. Veins strengthen the fragile and ultra-light wing membrane. Strengthening inter vein connections creates cells of various sizes. Insect wings are still extremely light but strong enough for insect flight. For most winged insects, wings are crucial for survival and, therefore, need protection. Humidity, dust and dirt can make the wings useless for flying, so evolution of insects lead to protective hydrophobic or even superhydrophobic wing surface properties [WNB96][Wat+08][WCW10][Dar59].

2.3.1 Nanostructures on insect wings

The nanostructures of insect wings differ between species. The wings and the nanostructures are transparent. The nanostructures are only revealed with high resolution microscopy techniques. The nanostructures reported on cicada wings are mainly hexagonally ordered pillars. These pillars are mostly slightly cone shaped, with a diameter of around 100 nm at the base and around 50 nm at the top. Their height varies from 100 nm up to 400 nm. The center-to-center

distance of the hexagonally ordered pillars is around 188 nm. These pillars are assumed to be responsible for the high contact angle [Wat+08] and so responsible for the (super)hydrophobicity.

2.3.2 (Super)Hydrophobic wing surface

(Super)Hydrophobic surfaces already give good protection against bacterial infections based on anti-biofouling mechanisms. Biofouling describes the process when organisms like bacteria attach and propagate on the material. Biofouling occurs primarily in places where water (droplets) can persist. The (super)hydrophobic surfaces also protect the surface against the attachment of dust and dirt. The self-cleaning properties that are so induced by the (super)hydrophobicity will also keep the wings mostly free of building bacteria colonies.

2.3.3 Mechanical bactericidal mechanisms

The mechanical bactericidal properties were discovered a few years after the discovery of the nanopillars by Elena P. Ivanova [Iva+12]. She showed that the penetration of the nanopillars ruptured the bacteria membrane by keeping the force between the atomic force microscope (AFM, see section 3.2) cantilever tip and a bacterium resting on the wing surface constant. In a time span of five minutes, the bacterium slowly sank before suddenly sinking 200 nm down. Ivanova showed that the rupture of the bacteria membrane could explain the sudden sinking of the bacteria.

Three mechanisms were known that can kill the bacteria mechanically. A significant chemical component of the nanopillars is diverse fatty acids (C10-C19, the number after the capital 'C' stands for the number of carbon atoms contained in the polymer tail of the fatty acids) [Iva+17][Iva+13b]. Apart from the bactericidal effect of the fatty acids themself, the fatty acids have an adhesive effect on the membrane of gram-negative bacteria because their membrane is exposing a lipid layer, see section 3.5. The adhesion of the bacteria membrane to the nanopillars is the prerequisite for the different bactericidal mechanisms to function.

The adhesion starts on the top of the nanopillar and pulls the bacteria membrane over the nanopillars downward along the nanopillar wall. The resulting tension in the membrane can cause the nanopillars to penetrate through the membrane Fig. 7a.

The second interpretation is that during the downward movement along the nanopillar walls of the bacteria membrane, the membrane over-stretches in the valley between the nanopillars, causing the membrane of bacteria to lose its integrity and rupture Fig. 7b.

The third known possibility uses the self-propelled or imposed motion of the nanopillars (for example, by the vibration of the wings). Alternatively, when the bacterium has an imposed movement over the nanopillars. Areas of the membrane adhere to the tips of the highest nanopillars that move back and forth relative

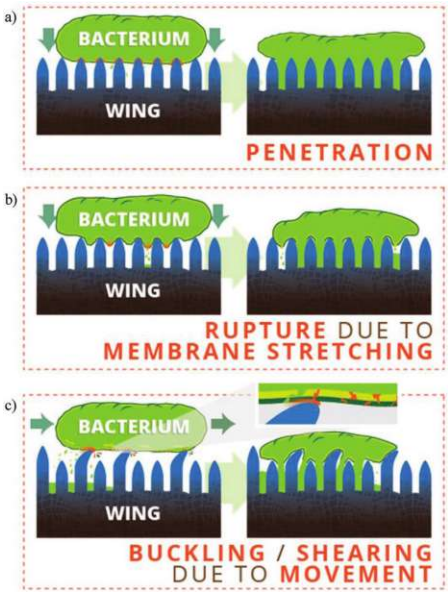

Fig. 7: The different killing mechanisms currently known [Rom+20] © Jessica Román-Kustas (CC BY-NC-ND 4.0). a) Penetration of the bacterial membrane by the nanopillars. b) Rupture of the over-stretched membrane between the nanopillars. c) Tearing of the membrane by relative motion.

to the bacterial membrane. The relative motion tears open the membrane around the adhered nanopillar Fig. 7c.

3 Methods

3.1 Species

The wings of four insect species were included in this study, and the selection of the species was made by availability. Especially in the natural environment, dead insects are very fast recycled. The collection of already dead specimens is, therefore, somewhat tricky.

3.1.1 Dragonfly *Sympetrum striolatum* - Common Darter

Previous articles reported dragonfly species with antibacterial wing properties [Ban+17] on gram-positive bacteria (see 3.5) whose membrane is harder to penetrate with nanopillars [Iva+13a]. The common darter (*S. striolatum*) was included in this study. It is one of the most common dragonflies in Europe, occurring anywhere where there are rivers, ponds and lakes with available still water for breeding.

Fig. 8: *S. striolatum*

3.1.2 Cicada *Amphipsalta cingulata* - Clapping Cicada

This diploma thesis includes three cicadas species, first the clapping cicada (*Amphipsalta cingulata*) is the largest cicadas native in New Zealand with the speciality that this species prefers to sing in sunny places. Johann Christian Fabricius was the first to describe the species in 1775 [Fab75].

Fig. 9: *A. cingulata*

3.1.3 Cicada *Kikihia scutellaris* - Lesser Bronze Cicada

the Lesser Bronze Cicada (*Kikihia scutellaris*) is also native in New Zealand, but it prefers to sing mostly in shaded areas in contrast to other cicada species that mostly prefer sunny places. Francis Walker first described the species in 1850 [LFL10].

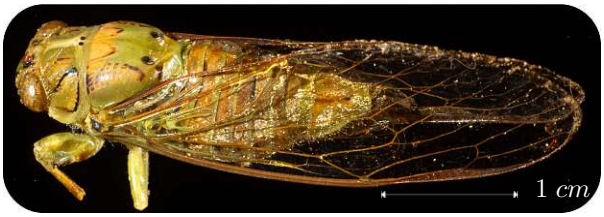

Fig. 10: *K. scutellaris*

3.1.4 Cicada *Magicicada septendecim* - Pharao Cicada

The *S. striolatum*, *K. scutellaris* and *A. cingulata* species were collected at the start of this diploma thesis. In late spring 2021, the famous 17-year periodical Pharao Cicada (*Magicicada septendecim*), native to Canada and the United States, emerged from the ground synchronously in tremendous numbers and swarmed in a biologically unique event.

Fig. 11: *M. septendecim* adapted from [FCS07]

3.1.5 Cleaning the wing surface

Cleaning the insect wing surfaces of dust, fungi, and other particles that were deposited during the collection and transport of the probes was initially a demanding prerequisite. The procedure was challenging because the wings are so fragile. Cleaning wings with water has the problem that the wing will not submerge into the water because of the (super)hydrophobicity of the surface. Cleaning with acetone (which would allow the wings to submerge) led to the suspicion that the surface was influenced because the shininess was reduced after the washing procedure. Isopropanol did not seem to affect the wings of the cicadas, but some of the other materials lost some of their shininess after washing. Verification of intact nanopillars with AFM techniques is burdensome. Only desisted water was used for the cleaning if cleaning was necessary at all. Especially the dragonfly wings are so fragile that no washing was feasible without destroying the wing.

3.1.5.1 Ultrasonic bath

In multiple situations, an ultrasonic bath (Sonorex RK 102 H, Bandelin, Berlin, Germany) possibly improved the results (for example, removing air bubbles from resin or other molding and casting materials). Nevertheless, in the end, the ultrasonic bath is only used to wash the cicada wing pieces (see section 4.13.2). Distilled water or isopropanol was used as a cleaning medium. The dragonfly's wings could not withstand an ultrasonic bath, the wings collapsed and the membrane between the veins dissolved.

3.1.6 Sectioning homogeneous wings pieces

Wings are scarce goods, so careful and economical handling is necessary. Five mm round wing pieces were the optimal configuration for the experiments while at the same time minimizing the expenditure. An ideally shaped round scalpel (5 mm BP-50F BIOPSY PUNCH of kai medical, Solingen, Germany) worked best on a hard surface to section the wing into as many homogeneous pieces as possible.


Fig. 12: 5 mm BP-50F BIOPSY PUNCH of kai medical, Solingen, Germany. 95 mm in length.

3.2 AFM - Atomic force microscope

In this diploma thesis, the main instrument for scanning the topology of the insect wings is the atomic force microscope (AFM) in tapping mode. The AFM uses a sharp tip on the end of a microscopic cantilever to raster scan the topology of the sample surface. The cantilever oscillates near its resonance frequency. The short-time interactions of the topmost atoms in the tip with the sample are used to reconstruct the topology of the sample with only minimum interaction with the surface. AFM tapping mode allows for measurements with the least destructive force. The AFM scans also showed an "adverse viscoelastic" behavior using contact mode. The composition of the nanopillars probably causes the "adverse viscoelastic" behavior, so this diploma thesis uses tapping mode for all AFM images.

Most investigations were performed with an MFP-3D-BIO AFM (Asylum Research, Oxford Instruments plc) because the more accessible chamber enables a faster switching time between different samples. However, some scans used the Cypher ES (Asylum Research, Oxford Instruments plc, Abingdon, United Kingdom) AFM. The tip used in all scans were BudgetSensors® Tap300-G (resonance frequency 300 kHz; force constant 40 N/m; cantilever made of uncoated monolithic Silicon).

3.2.1 AFM image processing

Often AFM scan representations are made with exaggerated z-axis, which can lead to misinterpretations. For example, when the nanopillars are represented with a standard generated image in Gwyddion like in Fig. 13[NK12].

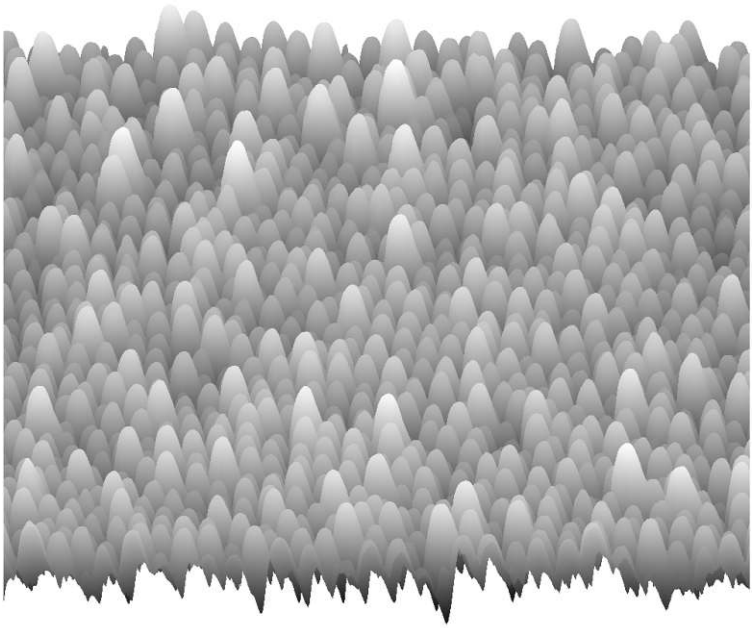

Fig. 13: The standard Gwyddion [NK12] 3D representation of an *K. scutellaris* wing surface scan. The x-y base size is 5×5 µm^2 with a maximum height in z-direction of 300 nm.

The nanopillars look exceptionally high here, but when inspecting the z scale, one can see that lengths on the x-axis and y-axis are on another scale as on the z-axis. The coloring enhances the contrast of the pillars, and the combination of the adaptions gives a distorted representation of the surface prone to misinterpretation. A more natural representation the human mind can more easily interpret would be a 3D reconstruction of the surface Fig. 14.

Fig. 14: Basic blender™representation of *K. scutellaris* wing surface scan. Created from the same scan data as Fig. 13 with a base size of 5×5 µm^2 and a maximum height in z-direction of 300 nm [Mic15].

Representing 3D objects is most easily done using the STL (Standard Triangle Language) format. In this format, the object is split into interconnected triangular planes between marker points on the object. Gwyddion [NK12](2.59) can export an STL representation, but not as a solid object. Gwyddion can also export the AFM scans to numeric ASCII matrices (8 significant

digits). These numeric ASCII matrices containing the topology data of the scan can be directly read by Matlab[MAT20].

The AFM scan data is converted to an STL object using a Matlab [MAT20] script written during this diploma thesis that creates triangles between the data points, as illustrated in Fig. 15.

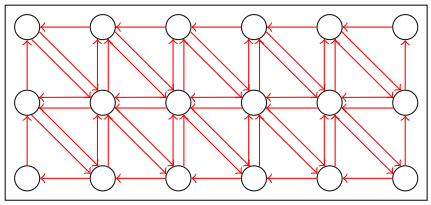

Fig. 15: The AFM scan points are identified as triangle corner points for interconnecting the entire surface with triangles drawn here from a top view.

Additionally, the bottom, just under the deepest point, a square plane is generated. The sides are filled up with triangles running around the base, closing the gap between the surface and the bottom of the object. Many rendering software packages can create realistic images of STL objects. This diploma thesis uses the open-source 3D rendering software blender™ (Fig. 16) to create a realistic representation of the wing surface [Mic15].

Fig. 16: The blender™open-source 3D rendering software package was used to visualize the STL object.

3.2.2 AFM image scanning artefacts

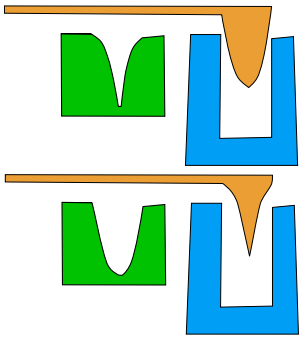

Fig. 17: Green is the scan of the blue valley with the orange tip.

The maximum slope an AFM cantilever tip can detect depends on several factors [Cle+96]. The main factor is that the cantilever tip is not a single point but some variance of a cone (depending on the specifications). A sample with a slope with a steeper angle than the tip cone will cause measurement artifacts by detecting the material with the sides of the tip. A particular problem of the nanopillar wing structure is that individual nanopillars obstruct the cantilever movement while scanning neighboring pillars. The AFM can not distinguish between the sharp tip point detecting the probe accurately and the base of the tip passing a steep vertical structure on the sample, like the nanopillar wall when scanning the valley between the pillars. The maximum measurable slope steepness is also dependent on the slope orientation (relative to the scanning direction). In Fig. 17, the green represents the AFM scan of the blue valley. The green valley walls represent the AFM tip's inverse form and do not represent the wall of the sample. The cantilever's inclination angle will accordingly add other artifacts to the scanned valley walls.

3.2.3 Extracting topology data from AFM scans

The AFM scans have to be interpreted to describe the nanopillar topology. This is best done with automated algorithms.

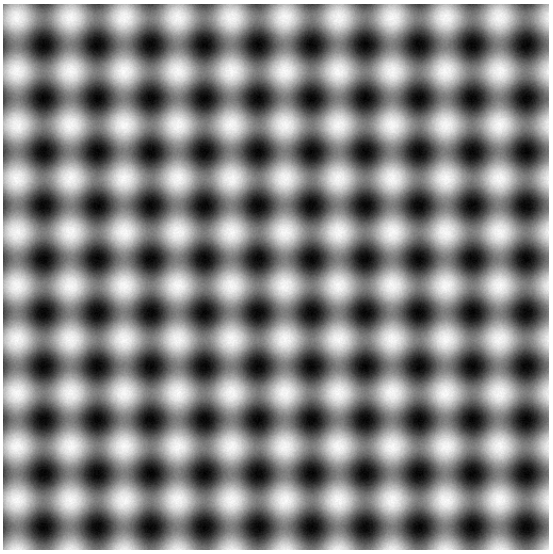

Fig. 18: Generated sample structures as PNG file (5×5 µm^2).

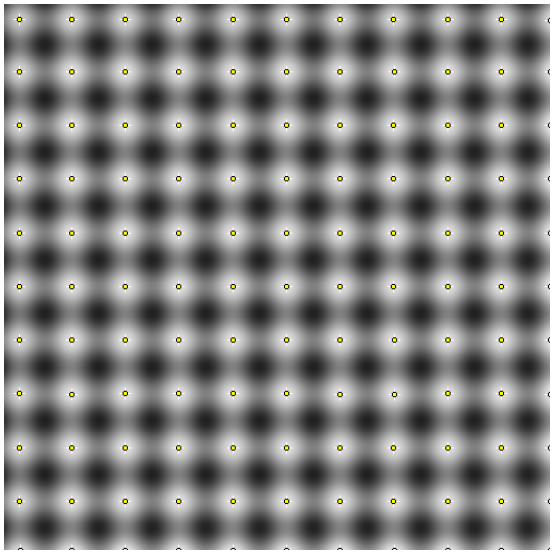

Fig. 19: Same as scan Fig. 18 but with FFT bandpass filter and marked maxima found by Fiji.

The Asylum AFMs generate files in the IGOR Pro Binary Wave format (IBW). The software package Fiji [Sch+12] (designed for biological-image analysis) was used already for many other tasks, though Fiji can not import IBW files. The software package Gwydion[NK12] (designed for scanning probe microscopy data processing) can read IBW scans, whereas detecting the

top center of the pillars for statistical measurements did not give the expected results. This study's functions, for example, detecting the nanopillar tops, seemed to work better with Fiji. So Gwydion was used to export the raw topological data to ASCII format in 8 significant digits and a PNG image that was thereafter imported in Fiji. The raw AFM data is still rather noisy for the nanopillar top detection. Therefore the Fast-Fourier-Transform (FFT) bandpass filter was applied to the scan using structure size between 3 and 30 pixels with 5% tolerance (Fig. 19). FFT Filtering will generate smooth nanopillar surfaces that can support the Fiji Process→find maxima... process. The result of finding maxima with "Point Selection" and prominence bigger than 18 are the selected pillar center-point coordinates. These center-point coordinates were exported to CSV with save-as→XY-coordinates.

The python script (see section 7.2.1) has been used to calculate the average distance to the nearest three other nanopillars. Note that only three instead of the six neighboring pillars were used to reduce the influence of missing nanopillars and nanopillars at the sides and corners of the AFM scan. The calculated data is then represented in the results section of this document with Pgfplots in Latex [Tan19].

3.2.4 Nanopillar height estimation

During a 5×5 µm^2 scan, the deepest point can be assumed as the minimum deepness of the valleys between the nanopillars. At the deepest point, the orientation of the pillars was likely such that the cantilever tip could sink deep between the structures without neighboring pillars disturbing the movement. Note that the so-measured deepness is just a minimum. The valleys could be considerably deeper without the AFM showing any difference (see Fig. 17). The "false" deepness will not affect the height distribution because the real deepness is just an offset to the maximum AFM deepness. The SEM micrographs show no lower structures for the cicada between the pillars that the AFM could have missed. The SEM geometry reproduction of the pillars shows very similar heights as on AFM images, just with an offset.

3.3 SEM - Scanning electron microscopy

Scanning Electron Microscopy (SEM) generates a topological micrograph by raster scanning the surface of a sample with a focused beam of electrons. Recording the electron interactions with the sample produces the micrograph representation.

The SEM micrograph scanning was performed using the University Service Centre for Transmission Electron Microscopy facilities, Vienna University of Technology, Austria (operator Karin Whitmore). The microscopes used were a Scios 2 DualBeam and a FEI Quanta 250 FEG (both from Thermo Fisher Scientific GmbH, Waltham, Massachusetts, U.S.). All samples were mounted on the specimen holder with double-sided adhesive carbon tape (Thermo Fisher Scientific GmbH, Waltham, Massachusetts, U.S.) and sputtered with a 4 nm Gold/Palladium layer.

3.3.1 SEM reconstruction of pillar geometry

Scanning Electron Microscopy (see 3.3) micrograph of the nanopillars show the steep walls. The actual geometry of the nanopillars can be reconstructed from detailed SEM micrographs by assuming that the nanopillar looks the same from all sides. Because the inclination angle of the nanopillars on SEM micrographs can be estimated, the original structure can be reproduced, whose projection will produce the representation seen on the SEM micrographs. The reverse projection to the original geometry is made individually for the different wing surfaces.

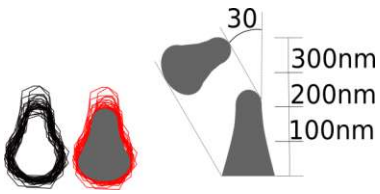

Fig. 20: nanopillar geometry reproduction in SEM

3.4 Bacterial strains

There are countless bacteria species and many strains with different properties and capabilities for every species [TSG96]. Bacteria can adapt very fast to changing environments, triggering the development of new strains. The high adaptability of bacteria is why it is so important not to interrupt antibiotic treatments. Every bacterium that survives the treatment can be the basis of a new antimicrobial resistance (AMR) bacteria strain. World Health Organization (WHO) defined AMR as a global threat to human health in 1998 [NSS22]. Finding a mechanical antibacterial mechanism would prevent most bacteria methods from becoming resistant because resistance to a mechanical antibacterial surface would need significant changes to the membrane of the bacteria.

Two leading categories of bacteria (gram-negative and gram-positive) are distinguished mainly over their membrane composition [Gre78]. This diploma thesis selected one bacteria species of both categories to test the wing surface antibacterial properties.

3.5 Gram-negative bacteria

The gram-negative bacteria have two lipid bilayers (Fig. 23). Between these two membranes, there is a thin peptidoglycan layer. Moreover, the outer membrane contains lipopolysaccharides in its outer leaflet and phospholipids in the inner leaflet. We use *Escherichia coli* (Fig. 21) as a representative. The strain DSM 5698-0416-001 was acquired from Leibniz Institute DSMZ-German Collection of Microorganisms and Cell Cultures GmbH, in a freeze-dried state.

The outer membrane of gram-negative bacteria can directly interact with the nanopillars. Previous studies show that the gram-negative category is more sensitive to the adhesion to the nanopillars.

3.6 Gram-positive bacteria

The gram-positive bacteria family have only a single lipid bilayer (Fig. 23), but a thick peptidoglycan layer protects the lipid bilayer. This protection could hinder the adhesion to the nanopillars, making it more difficult for the pillars to penetrate the membrane [Has+12].

This diploma thesis uses *Staphylococcus aureus* (Fig. 22) as a representative for the gram-positive family. The strain DSM 1104-1019-001 was also acquired from DSMZ-German Collection of Microorganisms and Cell Cultures GmbH, in a freeze-dried state.

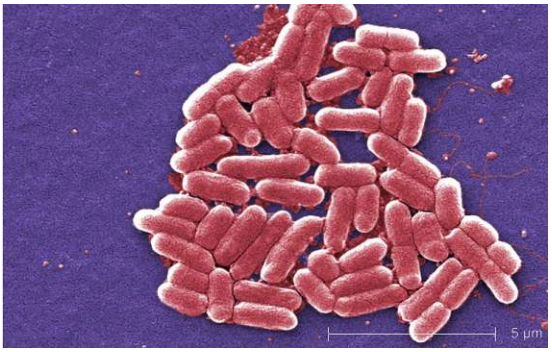

Fig. 21: The gram-negative *E. coli* [Car21]

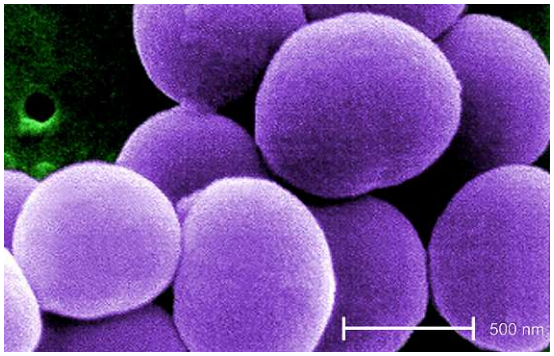

Fig. 22: The gram-positive *S. aureus* [AC01]

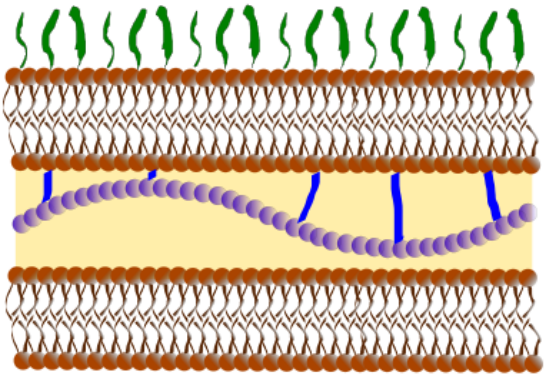

Fig. 23: Gram-negative membrane

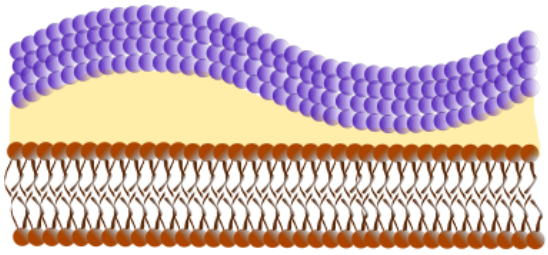

Fig. 24: Gram-positive membrane

3.7 Bacterial growth

A constant concentration of bacteria is crucial to compare bacteria adhesion and statistics of living and dead bacteria. Bacteria proliferate by division. If there are enough nutrients in the surrounding of a bacterium, the bacterium will enter a division cycle. In a bacteria culture as a whole, bacterial proliferation is called growth. The bacterial growth follows a typical LiveCycle [Hal+13]. Harvesting of the bacteria for experiments was done at the end of the exponential phase. The classical method to observe the bacteria concentration is the OD_{600} method.

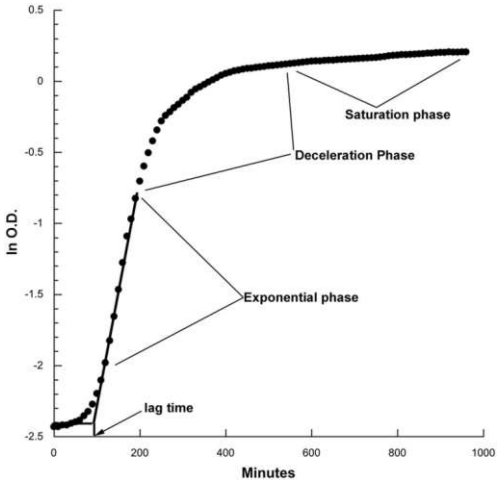

Fig. 25: Typical bacterial growth curve [Hal+13]. $ln(OD)$ plotted versus *time*

OD_{600} describes the optical density of a 10 mm thick bacteria solution at a wavelength of 600 nm. The OD_{600} is a standard used to indicate bacteria culture's bactericidal density and growth state. Every OD_{600} analysis instrument will give slightly different values depending on many parameters. To get objective values, one needs to calibrate the instrument values. Because all analyses were performed with the same instrument, no exact cali-

bration was necessary. OD_{600} values are measured using a BioTek EL800 plate reader (The Lab World Group, Hudson, MA, U.S.) (Fig. 26).

3.7.1 Bacteria concentration

The extraction point describes the point on the growth curve (Fig. 25) where the concentration of the bacteria reaches the desired concentration for a specific experiment. This diploma thesis uses the extraction point $ln(OD_{600} = 0.5/0.6) = -0.7/-0.5$, measured with a BioTek EL800 Fig. 26. Singular wells of a 96-well plate filled with 100 µl bacteria solution. OD_{600} defines the light obstruction through one cm medium. The 100 µl bacteria solution fills the well only to 3.5 mm thickness, so a correction factor of 2.9 must be installed ($\frac{10}{3.5} = 2.9$).

Fig. 26: BioTek EL800 plate reader (The Lab World Group, Hudson, MA, U.S.)

$OD_{600} = 0.040$ was measured, with the EL800, for a well filled with 100 µl medium without bacteria. For example, if the EL800 measures 0.208 for a well, the reference of 0.040 was subtracted and then multiplied with the correction factor of 2.9, which gives us an overall OD_{600} value of 0.371. The target bacteria concentrations values for this diploma thesis are $\frac{0.50}{2.9} + 0.040 = 0.212$ for OD_{600}=0.5 and $\frac{0.60}{2.9} + 0.040 = 0.247$ for OD_{600}=0.6 and messured with 100 µl bacteria solution in the wells of the EL800 plate reader.

3.7.2 Fluid growth medium

Bacteria need an environment where they can find nutrients and migrate. Some bacteria have propulsion, and other bacteria are moved by their environment. This diploma thesis uses bacteria in a fluid environment (medium) to test the antibacterial properties of the nanopillars. The medium gives the bacteria space to live and provides them with all nourishment needed to survive and proliferate. This diploma thesis uses a standard recipe for the fluid medium (also called LB medium) to grow the bacteria. LB-media are mostly based on the recipe (a water solved mixture of yeast, sodium chloride and Tryptone which is a variety of peptides formed by the digestion of casein) published in 1951 by Giuseppe Bertan [Ber51].

amount	ingredient
10 gram	Tryptone
10 gram	NaCl
5 gram	yeast extract
1000 ml	distilled watter

Table 1: LB medium ingredients.

The yeast extract provides the organic components, including the needed vitamins, to nourish the bacteria. At the same time, Tryptone provides the essential amino acids for the growing bacteria. The sodium chloride is provided for the osmotic balance.

After mixing the ingredients in a glass bottle, the bottle was disinfected by autoclaving (heat treatment 125 °C degrees and at 1.3 bar pressure) for 30 minutes. The LB medium was stored for the duration of the diploma thesis in a 4 °C temperature storage room.

3.7.3 Thermomixer with heat block

Bacteria in liquid cultures need oxygen and free space to proliferate. Both are provided by shaking the suspension constantly. The shaking also constantly redistributes the nutrients and avoids bacterial settlement on the bottom of the suspension container. A bottom settlement would result in local nutrient reduction and eventually cause bacterial death. Shaking also prevents bacterial clumping, ensuring prolific homogeneous bacterial reproduction. The temperature was kept at the ideal prolific bacterial reproduction temperature of 37 °C.

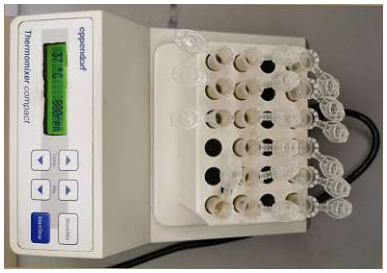

Fig. 27: Termomixer (25x17cm)

A Thermomixer Compact 5350 (Eppendorf SE, Hamburg, Germany) provides these ideal growth parameters with an included heat block to ensure a constant temperature. The Thermomixer can simultaneously cultivate 24 Eppendorf tubes® (Eppendorf SE, Hamburg, Germany) of 1.5 ml.

3.7.4 Bacteria multiplication

The acquired bacteria were not delivered ready for use. They had to be defrosted and multiplicated to create enough ground stock for all experiments. Therefore, 7 ml LB medium was heated to 37 °C. The ampoule (a sealed glass container) with the bacteria stock was broken using a small heat shock, and the pellet from the ampoule was added to the 37 °C LB medium. Incubation of the bacteria in the Thermomixer for six hours until the logarithmic phase measured with an Optical density of $OD_{600} = 0.7$ (see 3.7) was reached.

The bacteria were stored in cryo state at −50 °C (and −80 °C depending on availability) to have them readily available for the experiments.

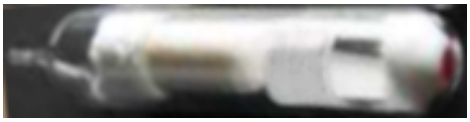

Fig. 28: Dry frozen ampoule (6 cm in length)

Fig. 29: 1.8 ml CryoTubes™(5 cm in length)

Bacteria die by forming ice crystals when they are directly frozen. For protecting the bacteria mixture in the cryo state, a frost protection agent is necessary by adding a one-to-one mixture of glycerol and PBS (Phosphate-Buffered-Saline). The frost protection mixture is also heated to 37 °C. After mixing the frost protection agent one-to-one with the grown bacteria culture, the culture is portioned in 1.0 ml per 1.8 ml CryoTubes™, Nunc™ (Thermo Fisher Scientific, Waltham, Massachusetts, USA) and stored in a -50 °C and a -80 °C freezer.

3.7.5 Bacteria reactivation

For reactivation of cryo-stored bacteria, 1.0 ml of the frozen bacteria were slowly heated to 37 °C. The cryo-stored bacteria were first fluidized in a 4 °C chamber to reduce the temperature shock. Nine tubes of 1.5 ml each filled with 1.3 ml LB medium are heated to 37 °C in the Thermomixer during the fluidization process.

For multiplying, 100 µl of the fluidized bacteria culture were pipetted to each of the nine 1.5 ml LB medium-filled tubes. The tubes are uncovered to provide air to the bacteria and

left for incubation in the 37 °C Thermomixer at 800 rpm for a few hours until the desired concentration was reached, slightly covered with a sheet to partly hinder evaporation.

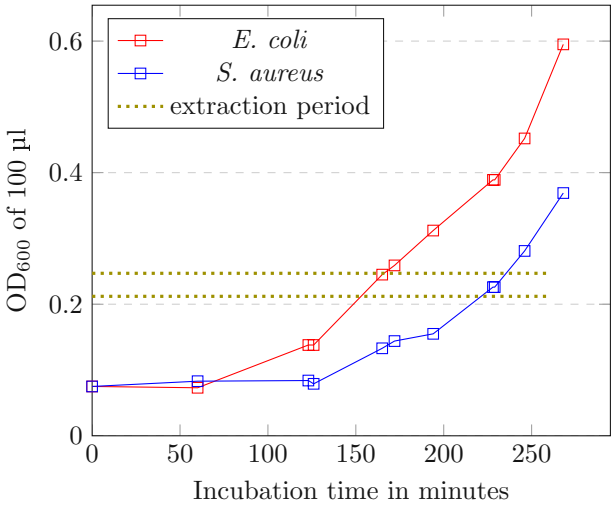

Fig. 30: *E. coli* and *S. aureus* incubation in LB-medium (periodic OD_{600} measurements on 100 µl volume). The green dotted line marks the extraction period/concentration.

A constant bacterial density is needed to get comparable test results, so the vaporized LB medium must be replaced in such a way that the concentration is in the target range of chapter 3.7.1. Much better than adding LB media to reduce the concentration is reaching the target range ($OD_{600} \approx 0.230$) directly. Therefore the specific strain growth curves are essential (Fig. 30).

The growth speed varies for every strain and bacteria species. The growth curves of the *E. coli* and the *S. aureus* are measured to have an estimate for the timing of the test runs. The target range is marked on the vertical axis. To harmonize the test timings as well as possible, the growth of the *S. aureus* had to start 70 minutes before the *E. coli*. After 140 minutes, the periodic (5 to 10 minutes) measurements can start. As soon as the target range is reached, the bacteria are immediately used in the live-dead experiments.

3.7.6 Poly-L-Lysin slides

Every bacterial strain and experiment will have different survival ratios in particular experimental conditions. An inert test surface is needed to exclude different influences responsible for a lower survival ratio other than the wing surface itself. The test surface must be without bactericidal properties, allowing the bacteria to adhere. Poly-L-Lysin-coated slides (E63410-01 Science Services GmbH, Munich, Germany) are transparent as the wings themself. The bacteria can easily adhere to the Poly-L-Lysin coating. One Poly-L-Lysin-coated slide with living bacteria and one where the bacteria will be methanol-killed after incubation accompanies every live-dead experiment. Comparing the survival ratios of the bacteria on the Poly-L-Lysin-coated slides to the survival ratios of bacteria on the wing samples gives a good indication of the antibacterial properties of the wing surface.

3.7.7 Selected bacteria stains

Live-dead staining was performed with propidium iodide (PI) (Sigma-Aldrich, Merck SA, Germany) and bisbenzimide Hoechst 33343 (Hoechst) (Sigma-Aldrich, Merck SA, Germany), both

obtained from Merck KGaA (Darmstadt, Germany). PI is a nucleic acid stain that does not permeate intact membranes and therefore stains only dead cells in which the integrity of the membranes is damaged. In comparison, Hoechst is a DNA stain which is able to pass intact cell membranes.

Both dyes were used as the protocols state. To obtain a stock solution, PI powder was dissolved in water [1 mg/ml]. In the experiments, this stock solution was further diluted in PBS to 40 µl/ml [Cia+88][Sci21a]. Hoechst was initially dissolved in water [0.5 mg/ml] and, for usage, diluted in PBS with 25 % methanol to 6 µl/ml [Cia+88][Sci21b]. Methanol was used as a fixation to improve the stability of the stained samples [MCL84].

3.7.8 Developed bacteria staining procedure

For staining bacteria, the recommended PI concentration is 1 µg/ml with an incubation time of 5 to 15 minutes [Sci21a].

Hoechst has a recommended staining concentration of 0.1 to 12 µg/ml with an incubation time of 10 to 30 minutes [Sci21b]. 0.5 mg Hoechst is dissolved in 0.5 ml PBS and kept in cryostat stock for later use.

In preparation 40 µl Propidium iodide was added to 1 ml PBS and 12 µl Hoechst, in solution (1 mg/ml), separately to 750 µl PBS and 250 µl ethanol.

Every specimen manipulation (such as the 5 mm wing disk) could disturb the experiment. Black 3D printed removable containers attached to glass slides as an incubation chamber reduce the need for handling the specimen. The staining solutions are light sensitive and protected by black 3D printed container top covers that allow air transfer but block out all light Fig. 31 (see section 3.7.9 for the description of the light blocking).

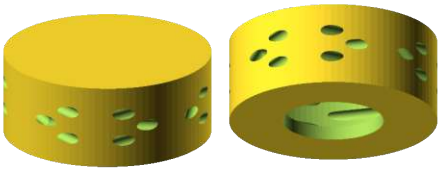

Fig. 31: 3D view of the container cover, diameter 3 cm

After incubation, the holder was emptied with a micropipette at the side of the compartment and immediately refilled with 110 µl of the PBS/Propidium iodide solution. The 15 minutes incubation time would cause the staining of the dead bacteria that were still attached to the surface. The solution in the compartment was light-sensitive after this step! The staining would bleach when exposed to ambient light, so the compartment had to be covered with the container top whenever possible. The ambient light during the procedure was reduced to an absolute minimum.

The subsequent washing step was performed using 110 µl pure PBS to remove the spare Propidium iodide. The bacteria dying during the fixation after this step would not be stained anymore. The last washing and fixating were done with 110 µl PBS/Hoechst/methanol solution. Note that the methanol will kill the bacteria and keep them in place. The solution is left in the compartment for 30 minutes to give the staining process enough time. As a final step, the sample was washed one last time using distilled water.

The incubation chamber breaks from the slide with a small amount of force at the notch on the side. A few drops of Fluoromount-G™ (00-4958-02, Thermo Fisher Scientific GmbH, Waltham, Massachusetts, U.S.) on top of the sample will conserve the specimen for later examination under the microscope.

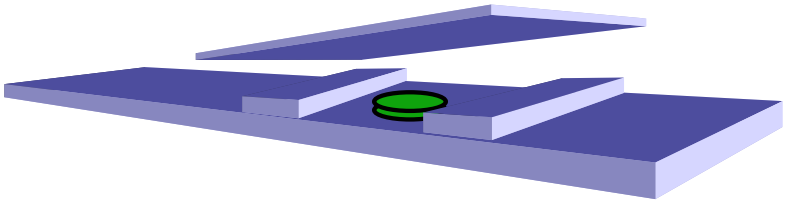

Fig. 32: The specimen (indicated with green color) was sealed between the glass slide and the coverglass with glass pieces as distancers. Front and back distancers were removed for illustration.

Depending on the thickness of the specimen, pieces of glass slides or small coverslips were used as distances around the specimen (Fig. 32). The coverslip is glued to the distancer using five µl nail polish. Both sides of the coverslip were sealed using nail polish to prevent the Fluoromount-G™ from evaporating.

3.7.9 Development of incubation containers

For the different experiments, specific utensils were required to optimize the procedures and make optimal use of the sparse insect wings at our disposal. This diploma thesis used the Elegoo Mars® printer to produce these utensils.

The 3D design was made with OpenSCAD®, an excellent scripting environment to program printable 3D models.

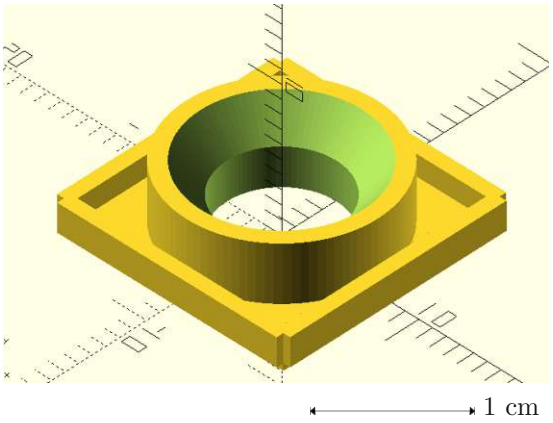

Fig. 33: Incubation container, inner diameter 7 mm. Can hold 350 µl incubation fluid.

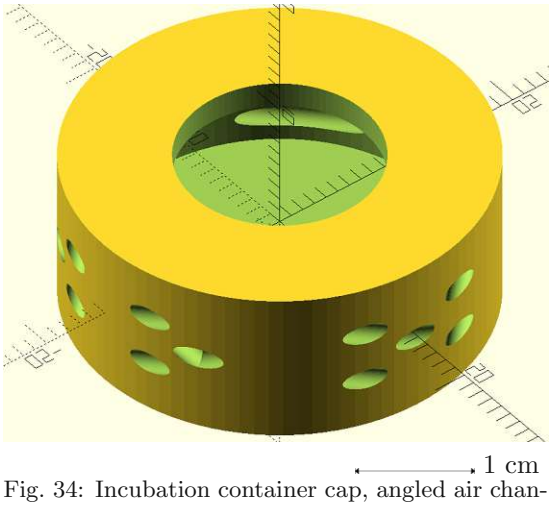

Fig. 34: Incubation container cap, angled air channels allow ventilation without light penetration.

The most important parts were the incubation containers Fig. 33. They had to be slightly wider than the standard wing sample. The amount of incubation liquid should be at least so much that it will not evaporate during the incubation period and not so much so that the connection to the slide will be in danger of leaking by saturation. The container must be mountable on a microscope slide around the tested specimen (such as a 5 mm wing disk). The specimen should stay mounted to the same place on the slide during the testing procedure. Every handling of the sample could disturb the results. A slight edge on the side of the container allows using a lever to remove the glued container from the microscope slide. A wide bottom plate allows an expansive gluing area so the space between the container and the specimen can be firmly closed.

After incubation, several staining steps are necessary. During these steps, special care has been taken to protect the specimen and staining liquid against bleaching (because of exposure to light) Fig. 35. Special caps on top of the containers were designed to ensure good air ventilation and minimal light penetration (Fig. 34). The ventilation holes enter the cap at a very steep angle and offer only a multi-reflection path for the light to enter. The container and the light-protecting cap were printed using black resin to block as much light as possible. The script to generate the models is available in the apendix 7.1.1.

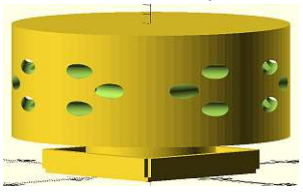

Fig. 35: Incubation container protected against light penetration.

3.7.10 Live-dead experiment setup

The same procedure is used for *E. coli* and *S. aureus* as the same LB medium (chapter 3.7.2) can be used to incubate them. The growth curve (Fig. 25) is slightly different but not significantly.

The 5 mm diameter samples are very light, so they must be fixated on the microscope slides. 5 µl nail polish or double adhesive tape can hold the sample without disturbing the experiment.

Fig. 36: Fixed wing sample (5 mm)

The samples all have thicknesses between 0.2 mm and 2 mm (casting), so a cover-slip (very thin glass cover to give the microscope a flat layer of even thickness) can not cover the probe plainly. Because for fluorescence microscope, the sample faces down to the optics, a cover-slip is mandatory to protect the optics. For this reason, we use a stack of mini cover-slips (glued together with nail polish) as distancers to the height of the sample on both sides of the probe.

Fig. 37: Sample holder (14 mm) glued on slide

The 3D printed sample holder with a 7 mm diameter inner compartment is placed just around the sample. The compartment is now filled with 350 µl bacteria solution with $OD_{600} = 0.6$. In this study, we selected an incubation time of one hour at room temperature in ambient light. Other studies used a wide range of incubation times of up to 18 hours.

Fig. 38: Sample holder (14 mm) filled

3.8 Confocal fluorescence microscopy

Confocal laser scanning microscopy (CLSM) is a technique for optimizing resolution and contrast using a spatial pinhole to obscure out-of-focus light. A three-dimensional image can be reconstructed by focusing separate images at different depths (z-stack). This imaging technique also allows us to find the wing surface in the z-stack more efficiently. The surface of the wing or the replica is seldom plain but slightly tilted or bent. The images in this diploma thesis were all made using 3 or 5 z-stack images, depending on the focus range necessary.

3.8.1 Live-dead microscopy

The fluorescence imaging was performed with an IX73 inverted microscope (Olympus Corporation, Tokyo, Japan) at the Department of Dermatology and a Zeiss LSM 880 Airyscan (Carl Zeiss AG, Oberkochen, Germany) and the Core Facility Imaging, both at the Medical University of Vienna.

Sample preparation and staining were performed at the TU Wien. The stained samples (wrapped in aluminum foil for light protection) were transported to the darkroom and analyzed with the confocal fluorescence microscope as fast as possible. Because samples have different thicknesses, the z-stack top and bottom focus points are registered manually. The microscope will then focus multiple layers between the registered focus points.

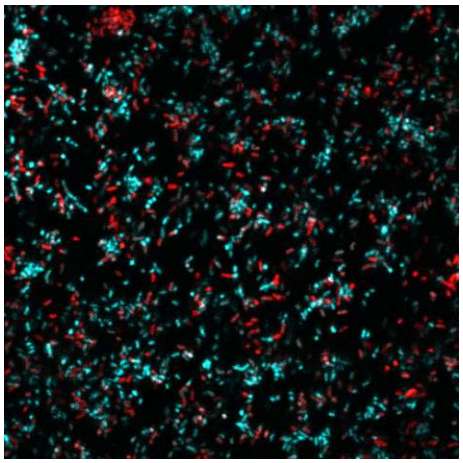

Fig. 39: Composite of live and dead *E. coli* image channels of 212x212 µm^2

At least three layers in the selected wavelengths are needed to get a good focus on the irregular surface. The bright-field pictures give a good indication of which z-layer is the sample surface for the different parts of the field of view. In tilted images, the focused level can spread over multiple z-layers. Statistical live-dead counting of the bacteria is done with the three red-cyan-brightfield image channels in the z-stack at the corresponding surface Fig. 39. During recording, fields of view have been selected that show clear bacteria occupied surfaces, preferably without disturbances. Multiple imaging spots, preferably five per sample, are selected randomly, whereas fields of view that contain visible veins or where the wing surface was damaged were ignored.

The magnification is selected so that singular bacteria are visible and a field of view that is as wide as possible. Multiple tests show that a C Plan-Apochromat 63x/1.40 objective (Carl Zeiss AG, Oberkochen, Germany) with a camera magnification so that the resulting image has between 100 and 110 µm side length is the best for visualization of bacteria. Note that this was a late realization in the course of this diploma thesis, and many of the images were made with other objectives. However, the camera magnification was always corrected in such a way that the resulting image has between 100 and 110 µm resolution.

The Olympus Viewer ImageJ Plugin version 2.3.1 [Cor] is needed for Fiji to import the recorded IX73 images seamlessly. This Olympus Viewer plugin needs a native Windows or macOS environment. Linux distributions can use the plugin in a standard Wine (windows emulation) environment. The images of the LSM-880 are supported directly by Fiji.

Therefore the IX73 images have a side length of 106.7 µm and a resolution of 1024 pixels. As the bacteria have a size of 600 nm (*S. aureus*) up to 2 µm (*E. coli*) they occupy areas with a diameter of 6 to 20 pixels. The LSM 880 images also had a resolution of 1024 pixels but a side

length of 103.6 µm. The bacteria size is nicely resolvable, and hundreds of bacteria still fit in the field of view.

3.8.2 Live-dead statistic analysis

The fluorescence images of stained bacteria had to be interpreted to obtain statistical data about the viability status of bacteria connected to the nanopillars. Different software packages and Fiji-plugins can do automated cell counting [Gri15]. However, detecting single bacteria connected in clusters was not satisfactory (Fig. 40).

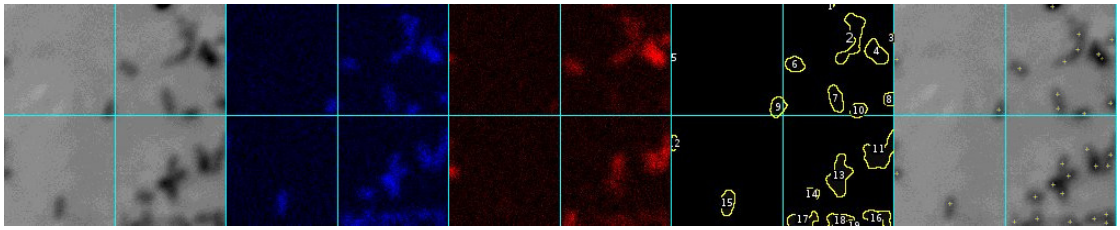

Fig. 40: From left to right, the same sample with *E. coli* in brightfield (a), Hoechst stained (b), PI stained (c), Automatic counting (d), and to the right manual counting (e). Some of the marked spots in the automatic counting image (d, 18 *E. coli* bacteria) compared to the same positions in the bright field image (a) are multiple bacteria. Manual counting (e) resulted in this same area to 29 *E. coli* bacteria.

The alternative is to do manual counting with support Fiji-plugins. Manual counting is a very error-prone and time-consuming procedure. Therefore a statistical protocol was developed to surpass the problems of manual counting. The first step of this procedure is to select the technically best images for the counting process of one sample.

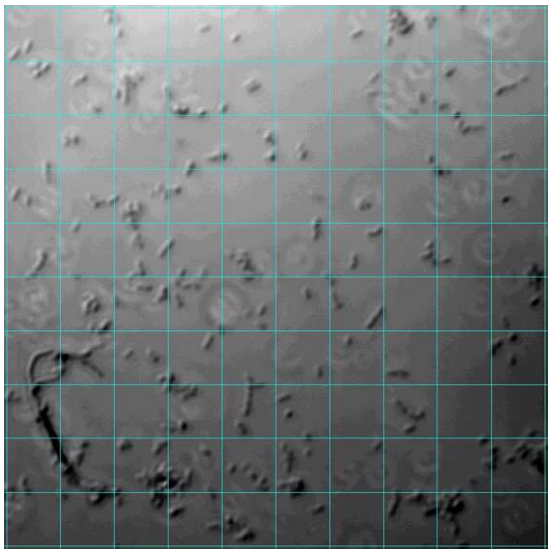

Fig. 41: *E. coli* bacteria on *K. scutellaris* wing replica gritted with Fiji to 10 by 10 counting areas of 100 µm^2.

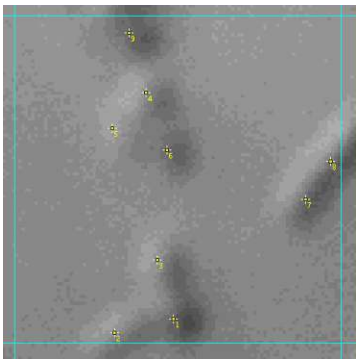

Fig. 42: Single 100 µm^2 grid from Fig. 41 of *E. coli* bacteria on *K. scutellaris* wing replica with markers pinpointing single bacteria.

Five random spot images with 100×100 µm^2 sizes were set as a recommendation, whereas sometimes, a reduction to three images was necessary because of the poor technical quality of the images. In the second step, these images were now divided into 10x10 counting areas (gritted) using the Fiji tool "Analyse→Tools→Grid..." using line grid areas of 100 µm^2 (Fig. 41).

The grids were placed centered on the image. Adding randomization would bring no further advantage because the image position is already random.

To obtain a statistically valid killing ratio for every image, a random selection of manually analyzed 100 grit fields over the specimen images (the resulting 300 to 500 grid areas) gives a valid reference to counting living and dead bacteria [Mut+17]. The third step is to select from these grid areas 100 randomly for counting. For good randomization, the website https://www.random.org/ has been used to generate sets of random numbers based on the atmospheric noise [Haa99]. Depending on the number of images, a set of 100 numbers was selected from a range of 1 to 300 to 500. Every grid was assigned individual numbers from left to right and top to bottom. The images were ordered sequentially and assigned to hundreds of the number sets. So the random number 342 represents the grid area in the third image on the fourth row, the second grid.

The random numbers were sorted for pragmatic reasons. This way, the grid areas are counted per image. Step four is to visually view one grid after the other and mark the positions of each bacterium by comparing the bright field image with the Hoechst and PI stained image Fig. 42.

The PI intensity determined if the bacteria were dead or alive. The staining is not exact, so some living bacteria can still show some staining. The border intensity is taken from the dead- and live reference slide, where the distinguishably is best visible. By comparing the PI intensity of each bacterium with the dead reference, the number of dead bacteria of all previously marked bacteria was added to a spreadsheet and stored in comma-separated values format (CSV)[Sha05] format so pgfplots [Feu11] latex package can be used for data analysis, see Figs. 43 to 45.

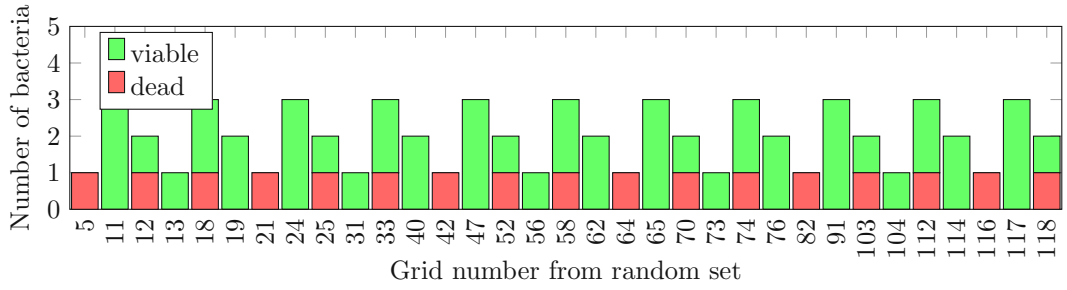

Fig. 43: Example of grid areas counted grid 0 until including 33

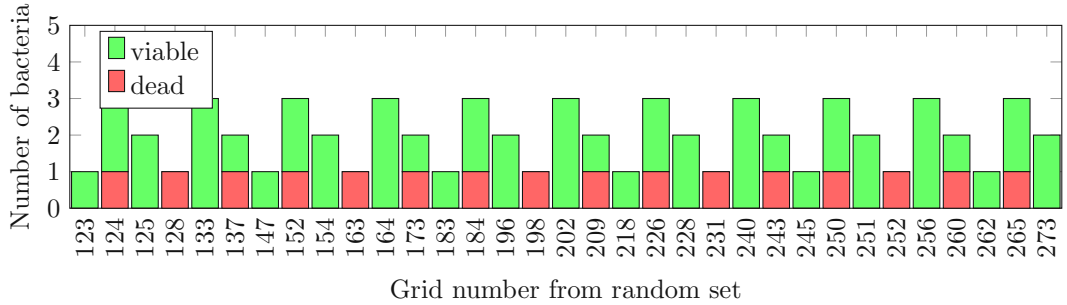

Fig. 44: Example of grid areas counted grid 34 until including 66

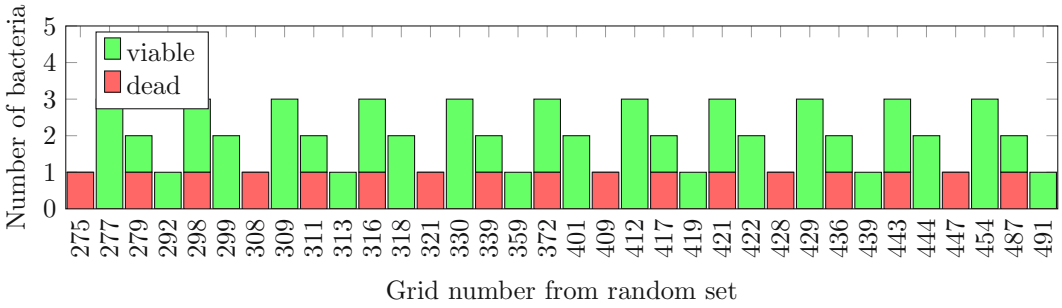

Fig. 45: Example of grid areas counted grid 67 until including 100

The random numbers of this example were generated for five images, where grids 5 to 91 are on image one, grids 103 to 198 on image two, etc. On x-axis-axis are the selected random grid numbers sequentially, and on the y-axis are the total number of bacteria in the grid. The green part of the cumulative bar represents the living bacteria, and the red part the dead bacteria. The data was split into three diagrams for better visibility.

Comparing this data between two different surfaces is difficult, so another representation was necessary to make the data comparable. The violin plots give a good impression of the distribution of the live vs. dead numbers in the grids (see Fig. 46) which represents the data from Figs. 43 to 45. Because bacteria tend to cluster, the distribution is not normal.

A box plot is a graphical representation of numerical data's locality, spread and skewness via their quartiles. A kernel density plot is a graph showing a dataset's distribution of values. A violin plot represents a combination of a box plot and a kernel density plot, which shows extremes in the data.

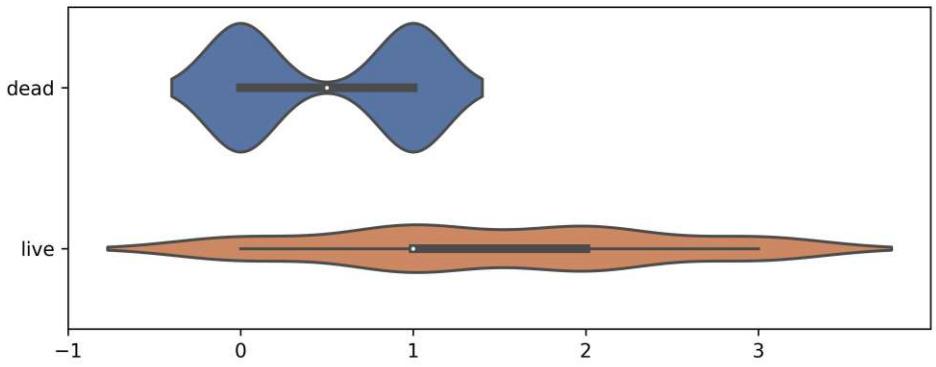

Fig. 46: Because the counting data of the image is generated periodically, the dead plot shows the belly at zero and at one. As the bellies have the same width, the frequencies of one and zero occurrences are equal. The live plot shows that the one and two events are equal in occurrence, as are the zero and three events, but these have only half of the occurences.

The violin plots of this diploma thesis were generated using pyton [VD09] scripts (see appendix 7.2.2) and utilizing the seaborn[Was21] and Matplotlib[Hun07] libraries. The CSV data from the experiments are processed in one run to generate a violin plot showing the dead and viable bacteria together in one plot (Fig. 46).

3.8.3 Protocol for counting bacteria in the layer directly above the nanopillars

Just before the end of the 60 minutes incubation cycle and just before the staining starts, 20 µl of the bacteria-containing fluid is extracted from the bottom of the incubation container (where the heads of the nanopillars are positioned.

The concentration of a droplet collected there with a pipette (FOUR E's scientific) represents the concentration of the area just above the nanopillars. The droplet of 20 µl is transferred to a 15×15 mm^2 cover slide.

A second cover slide is then positioned on top of the droplet. 20 µl solution just completely fills the area between the two cover slides without spilling. Brightfield images of the area between the cover slides were made with a Zeiss LSM 880 Airyscan and were used to do the counting with Fiji [Sch+12].

The bacterial clustering did not disturb the automatic counting results in this experiment because the single flat layer between the coverslips and the swimming bacteria did not cluster as much as the attached bacteria. The counting was done automatically using the build-in "find maxima" after applying filter-maximum with a radius of 5 pixels and an FFT bandpass filter using structure size between 3 and 40 pixels with 5% tolerance twice to remove the background shading.

3.8.4 Development scaffolds for control

Most resins have in their liquid state some form of toxic chemicals, notably VOCs (volatile organic compounds)[Men07]. Even when fully cured, a certain toxicity from not cured resin leftovers or decomposed UV-over-exposed resin will be present. Curred UV resin ages like most other polymer-based synthetic materials through UV light and become brittle.

The replicas in this diploma thesis were made out of UV-resin with some undefined intrinsic toxicity. A reference scaffold was 3D printed with micrometer-sized pillars. Live-dead experimental data with this scaffold will enable us to remove intrinsic toxicity from the data.

A five mm diameter disk with as small as possible pillar structures but not small enough to induce bactericidal properties was used as a scaffold. Initial models were designed using OpenSCAD® and printed with an Elegoo Mars® (Stereolithography (SLA)-based 3D printer). The details this 3D printer can theoretically print are on the scale of 50 µm (representing the pixel size of the internal screen). A newly available Phrozen Sonic Mini 8K® 3D Printer in the IAP institute at TU Wien can reproduce finer details in the range of 22 µm.

STL models, with details so close to the pixel size of the 3D printer scutter screen (UV exposure mask), become interpolated and challenging to realize (Fig. 47). Micrometer detailed models need to be aligned to the borders of the pixels on the scutter screen of the 3D printer. This alignment is not controllable in consumer versions of the slicer software Chitubox®[22a].

The Chitubox® printing files consist of a series of UV-mask images that control the shutter screen. A PNG image represents every layer of the STL in the sliced model. They are used to expose every individual layer in series. The 3D print tool UVTool can read, edit and write the sliced model data that the SLA-3D-printers use [22b]. UVTool gives us hereby direct access to the pixels of the SLA-3D-printer shutter screen.

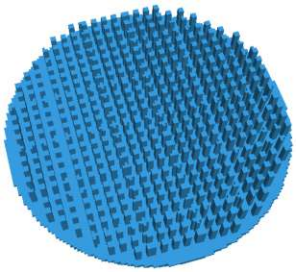

Fig. 47: STL object with 5 mm disks with 150 µm pillars rendered by chitubox.

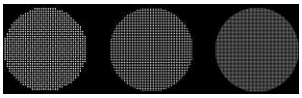

Fig. 48: Generated pillar image, exact usage of the pixels to generate the pillars.

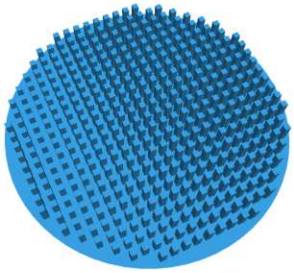

Fig. 49: Generated pillar image with 5 mm disks with 150 µm pillars rendered by chitubox.

A program was written to generate these PNG images directly without going over an STL object intermediate (Fig. 48), allowing the individual pillars to be represented by optimal and constant pixel arrangements. Tests showed that the minimal stable arrangement is a square of 4 by 4 pixels, allowing stable pillars of 250 µm in height. On the Elegoo Mars® this technique resulted in $200 \times 200 \times 100$ µm pillars and on the Phrozen Sonic Mini 8K® printer it resulted in $66 \times 66 \times 100$ µm pillars. The smallest successful pillar samples were used to do the reference live-dead tests.

The resulting scaffolds give the bacteria enough opportunities to evade the shear stresses that would flush them away during the staining procedure. The scaffolds are from the same resin as the wing surface replicas, so they can be used to verify the consequences of the resin toxicity.

3.9 Nanomolding - Reproducing the nanostructure

Previous studies in our group (by Sigrid Zobl [Zob18]) performed on butterflies showed that Polyvinyl siloxane (PVS, Coltène President The Original Extra light body, Altstätten, CH) can be used to obtain inexpensive stamps for nanosized structures such as the nanostructures that are responsible for structural colors on certain butterfly wing scale. The paste is intended for dental impressions and captures details even at the nanoscale.

This diploma thesis will evaluate simulator techniques for the insect wings and additionally use the alternative version "PRESIDENT The Original Xtra light" purchased from direct Österreich. The "Xtra light" version promises even more detailed molds.

This diploma thesis uses photopolymer resin as a material to build replicas. Compared to a two-component resin, the advantages of a photopolymer resin are control and extension of the time for the curing process and the fact that trapping of air bubbles inside was drastically reduced because no mixing procedure was necessary.

3.9.1 Casting forms

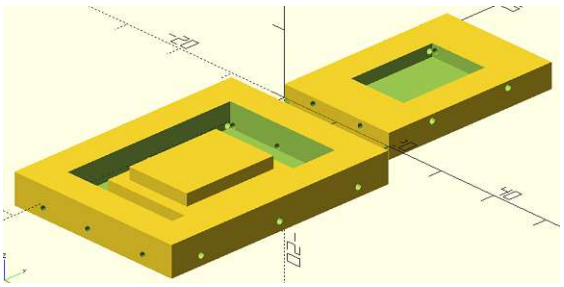

Fig. 50: Left the inverse resin casting form and right the PVS casting form. Scales are in mm.

Regular replica negatives were created using a replica form. The wing specimen was put in the center of the basin. The freshly mixed PVS was poured on top of the wing piece and filled out the form by the weight of the slides that are put on top of the PVS to add pressure to the forming process. The holes in the corners were included in the design to hinder bubbles from forming on the edges. The air and the extra PVS can escape the form through these holes. This replica-negative creation method results in a clean rectangle form of the negative.

For the resin replica, there is a similar form. However, the resin would bind with the 3D printed form because it was made of the same resin. This form had to be constructed using PVS that would not bind to the hardened resin. Therefore an inverse model was designed, which was used as a casting form for PVS. This PVS form fits around the replica-negative, so the resin can be poured safely over the replica-negative without spilling. The script to generate the models is available in the appendix 7.1.2.

3.9.2 Development of PVS negative replica techniques

Regular Polyvinylsiloxane (PVS) curring at room temperature takes 4 to 5 minutes. This short period leaves little time to enclose the nanopillars of the cicada wing surfaces. Cooling the PVS slows down the curing period so that the time to adapt and align to the surface of the master increases ([Zob18]). Reducing the temperature during the casting and curing process to 4 °C will prolong the duration of the fluidity phase to 30 to 70 minutes.

The Xtra light body PVS needed 25 minutes of curring time (at 4 °C) to reach a gumlike consistency and 40 minutes to cure eventually. Likewise, at 40 minutes, the light body PVS

reaches a similar gumlike consistency. After another 30 minutes, the PVS curing process ended.

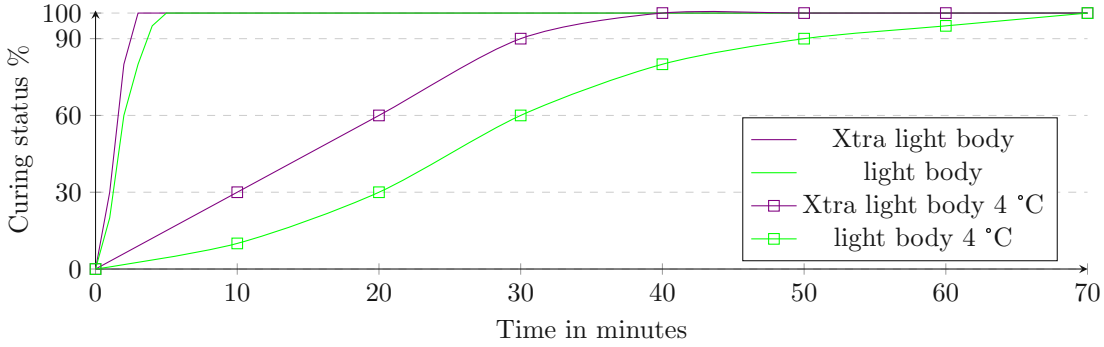

Fig. 51: Comparing the curing process of Polyvinylsiloxane at 20 and 4 °C

The negative replica stayed at 4 degrees for another 6 hours to ensure that the curing was completed in-depth. After extraction from the 4-degree chamber, the negative replica was left to adapt slowly to room temperature for another 6 hours.

The negative replica was made by placing the 5 mm circular wing fragment in a 3D printed casting form (see section 3.9.1). A blob of PVS was poured on top of the wing fragment and slightly pressed down by the weight of a stack of 6 glass microscope slides. The casing form and the glass slides on the top will guarantee a regular flat rectangular negative replica for better handling. The top glass slide will also hinder the detachment of the sample during the curing and shrinking process (PVS shrinks minimally during the curing process).

Fig. 52: Casting form with the inserted negative replica, the circular wing specimen (5 mm diameter) is still attached.

The wing specimen was carefully removed using tweezers from the side without touching the negative. If wing fragments stick to the negative replica, they will stick to the first cast positive replica.

3.9.3 Development of resin casting techniques

A photopolymer resin (Elegoo ABS-Like LCD UV-curing photopolymer rapid resin, GE-EL-3D-005, Elegoo, Shenzhen, China) was used as a molding material to obtain positive impressions (replicas). For imprinting, the PVS negative replica (the green PVS part in Fig. 52) was mounted on a hard surface using double-sided tape. Around the negative replica, the PVS casting form was also placed on the double-sided tape (the purple PVS part in Fig. 52).

Photopolymer Resin is carefully spread over the whole mold in a sheet using a Syringe to avoid bubbles. The procedure must occur in a dark room, so the resin does not start curring. For practical reasons, after casting the resin onto the PVS template, a cover slip for microscope slides was placed on top of the resin droplet to make the replica as thin as possible. For the first six hours, the photopolymer resin was protected from light. During this period, residual air bubbles had enough time to leave the resin interfacing with the nanopillar interface, which could otherwise disturb the curing process.

As a next step, the resin was put in shaded daylight for another three hours to start a slow curing process. Finally, the curing process was completed under UV light (UniTak3D UV Light Hardening Lamp, wavelength 405 nm, Shenzhen Redrex Technology Co. Ltd., Shenzhen, China). One second of UV light at a 30 cm distance interspaced with 30 seconds of cooling time for 5 minutes.

The coverslip is permanently connected to the resin. The negative replica is removed by pulling the mold from the side away from the coverslip with tweezers. The impression is now perfectly positioned on a 0.5 mm thick podium that can easily be broken and sculptured to the needs of further experiments. Sculpturing the impression requires special care because the amount of UV light makes the material very brittle.

4 Results and Discussion

4.1 *Sympetrum striolatum* - Common Darter Dragonfly

According to the research ethics in our group, specimens must be collected without killing individuals 2.2. At the end of the season (October 2020), the dragonflies tried to collect heat from the streets on the Donau-Insel in Vienna (Austria). The fast sundowns and cold nights probably hindered the specimens from finding a safe place for the night. So in the morning, a number of individuals on the side of the street did not survive the night. The wings of *S. striolatum* are extremely fragile. The cells of these wings are tiny, and the angles between the cells are steeper than those of the cicadas (compare Fig. 53 to Fig. 60).

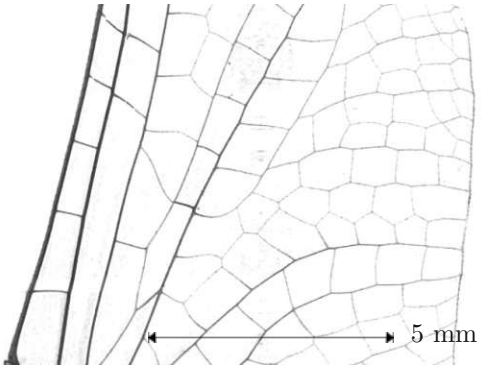

Fig. 53: *S. striolatum* wing Micro-CT.

The first AFM analysis of their wing surface lets us suspect this species does not have the hoped-for properties. No nanopillars could be found on the surface of the *S. striolatum* wings.

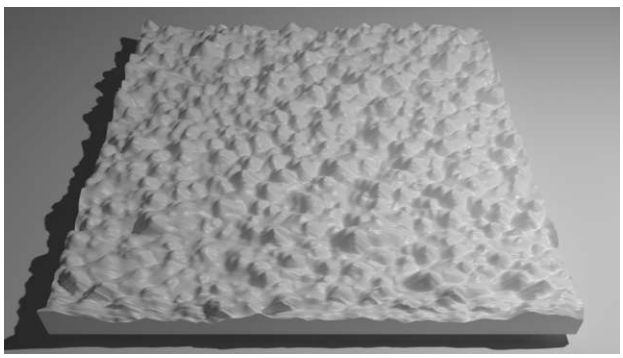

Fig. 54: *S. striolatum* wingsurface AFM image. Size 5000×5000 nm^2.

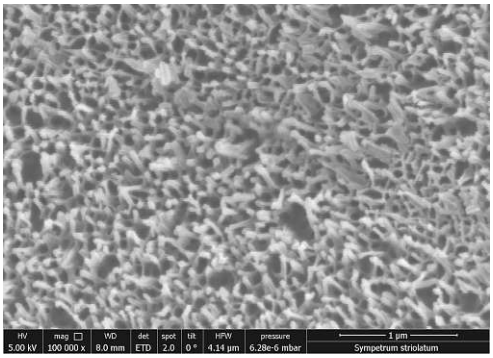

Fig. 55: SEM micrograph of the *S. striolatum* wing surface structure. Scale bar 1 µm.

A later verification (Fig. 54) showed that the images were distorted because the dragonfly wings are so fragile that an ultrasonic cleaning bath already destroys the wing compartments, and isopropanol dissolves the wing compartments completely.

The second problem is that the wing compartments of the dragonfly are so small (around one mm^2), fragile, and interconnected with relatively strong veins with microscale hooks. The AFM cantilever holder will likely touch the veins (or hooks) during the scanning process. The results are distorted scans. One needs to arrange the probe perfectly in line with the cantilever holder to scan an intact wing compartment or do specific sample preparation.

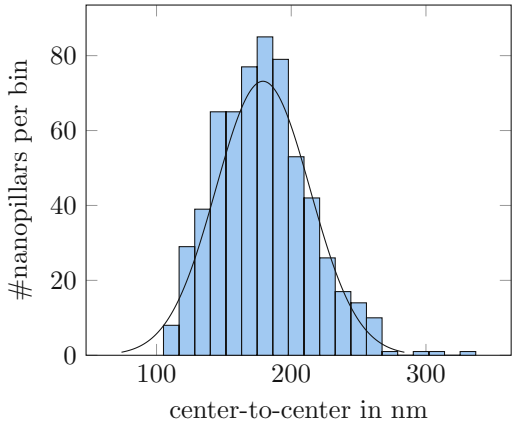

Fig. 56: Histogram of *S. striolatum* center-to-center nanopillar distance distribution with a mean of 179 nm, a σ of 35 nm and 613 counted nanopillars.

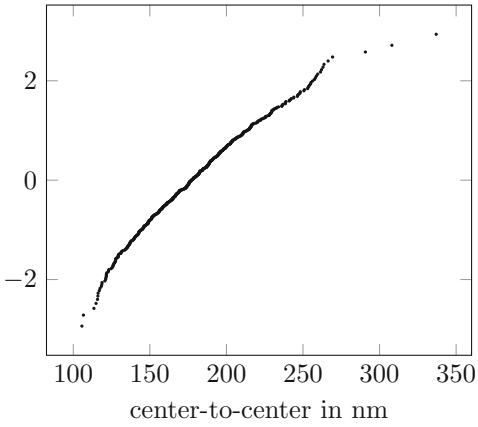

Fig. 57: Q—Q plot of the *S. striolatum* center-to-center nanopillar distance distribution of Fig. 56.

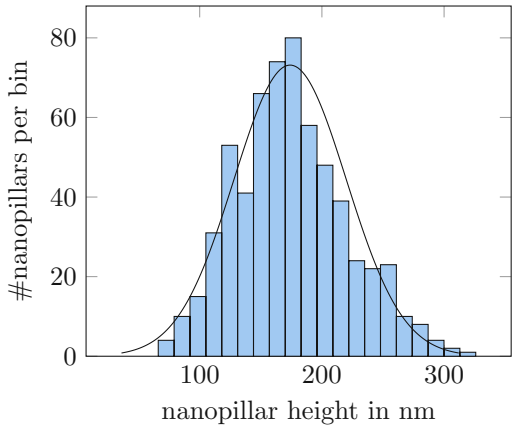

Fig. 58: Histogram of *S. striolatum* nanopillar height distribution with a mean of 174 nm, a σ of 46 nm and 613 counted nanopillars.

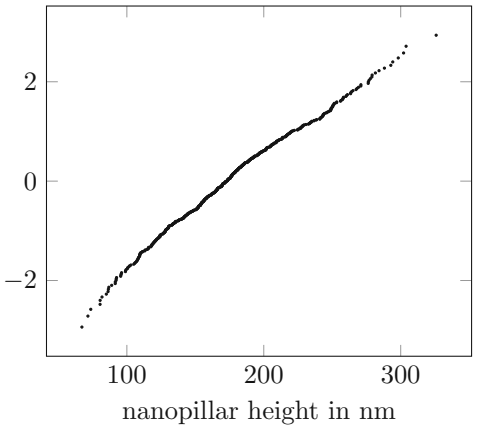

Fig. 59: Q—Q plot of the *S. striolatum* nanopillar height distribution of Fig. 58.

The surface shows an irregular pillar pattern. The pillars differ strongly in height (Fig. 58). The standard deviation is $\sigma = 46$ nm with an average pillar height of 174 nm. The distribution is nearly normal, as seen in the Q—Q plot (quantile-quantile plot, where a straight line indicates a normal distribution) plot Fig. 59, just the lower heights are a little underrepresented. The patterning of the pillar positions is very random as in Fig. 56 the standard deviation is again very large.

The SEM micrograph Fig. 55 reveals why the AFM had difficulty scanning the dragonfly wing surface, and the pillars are more like thin hairs. Imprinting techniques are, at the least, challenging to realize based on such a surface. These thin hair pillars are why the dragonfly wings were excluded from further imprinting experiments.

4.2 *Amphipsalta cingulata* - Clapping Cicada

David Marshall (from the Ecology and Evolutionary Biology Department of the University of Connecticut) was in New Zealand when we contacted him to collect specimens. He collected the species in New Zealand on the apartment terrace, where the light probably attracted the cicadas because they died near the light source. David Marshall kindly identified the specimens (as *A. cingulata*) and sent them to Vienna by postal service.

The wings of *A. cingulata* are more robust than the wings of the dragonfly. The veins are thicker (especially the top vein, which is massive in comparison) than the dragonfly veins, and the cells in the wing are larger.

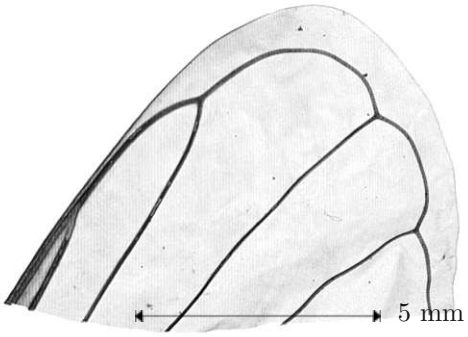

Fig. 60: *A. cingulata* wing Micro-CT.

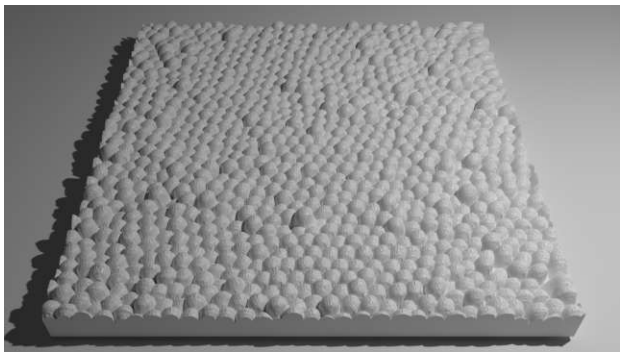

Fig. 61: *A. cingulata* wing surface AFM image. Size 5000×5000 nm^2.

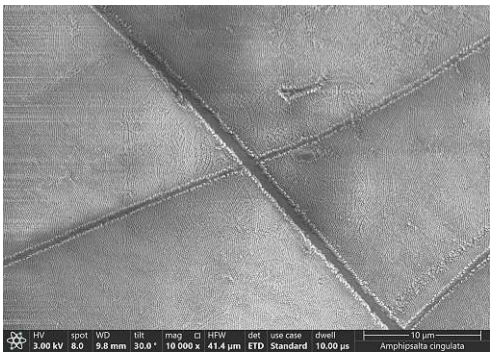

Fig. 62: SEM micrograph of the *A. cingulata* wing surface. Scale bar µm.

The AFM (Fig. 61) and SEM (Fig. 62) micrographs show a very regular structuring of nanopillars on the wings. The wings are far more regular than the wings of the dragonfly (Fig. 8). The veins are more rigid than the veins of the dragonfly, and the membrane fabric feels more stable. Ultrasonic cleaning and careful use of isopropanol did not change the wing surface in a detectable way.

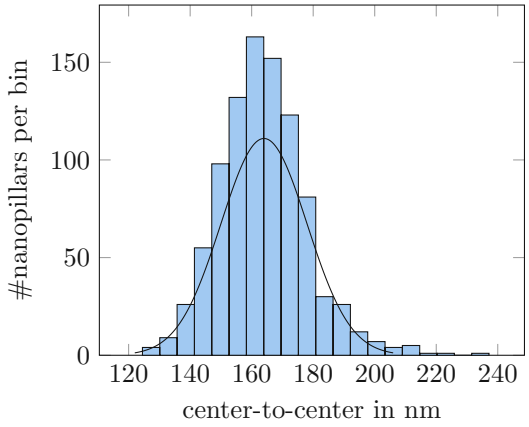

Fig. 63: Histogram of *A. cingulata* center-to-center nanopillar distance distribution with a mean of 164 nm, a σ of 14 nm and 930 counted nanopillars.

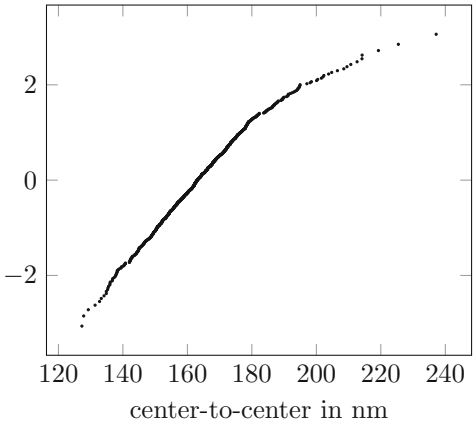

Fig. 64: Q−Q plot of the *A. cingulata* center-to-center nanopillar distance distribution of Fig. 63.

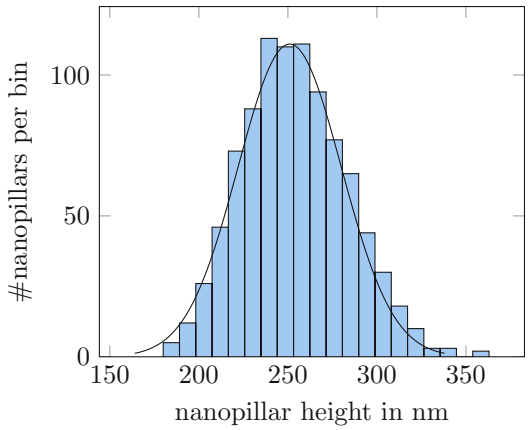

Fig. 65: Histogram of *A. cingulata* nanopillar height distribution with a mean of 251 nm, a σ of 29 nm and 930 counted nanopillars.

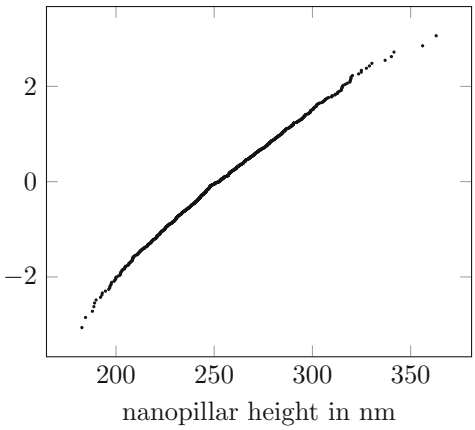

Fig. 66: Q−Q plot of the *A. cingulata* nanopillar height distribution of Fig. 65.

The regular structure can also be seen in Fig. 65, where the height distribution is displayed. The nanopillars are on average 251 nm high, with a standard deviation of only $\sigma = 29$ nm. Because of the regular hexagonal positioning of the pillars, the distribution of the center distance has a very low value of $\sigma = 14$ nm around a mean of 164 nm distance between the centers of two pillars (Fig. 63). As the Q−Q plot indicates these two distributions (Fig. 66 and Fig. 64) are also near normal.

The geometry of the pillars can be reproduced by averaging the projection of the pillars in a SEM micrograph (Fig. 68).

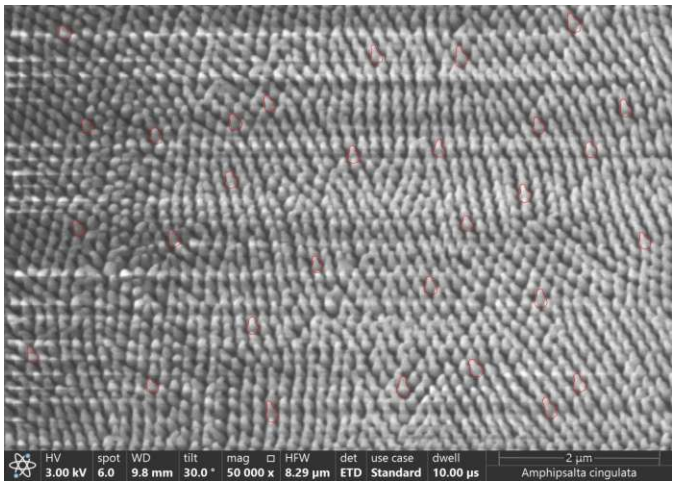

Fig. 67: *A. cingulata* nanopillar geometry.

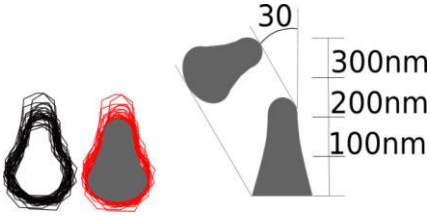

Fig. 68: *A. cingulata* collected nanopillar geometry from Fig. 67.

By drawing the circumference of random pillars in the SEM micrograph. These circumferences are aligned on top of each other. now an average structure can be estimated. The SEM micrograph is made from a 30 deg angle. Based on our assumption that the nanopillars looks the same from all sides the original structure can be reproduced. The projection seems accurate because the estimated average height of ca. 250 nm is compatible with the pillar height of the AFM measurments.

4.3 *Kikihia scutellaris* - Lesser Bronze Cicada

The *K. scutellaris* were collected along with the *A. cingulata* in New Zealand.

The *K. scutellaris* wings are the most promising ones in this diploma thesis because the nanopillars are the most prominent ones.

Fig. 69: *K. scutellaris* wing surface AFM image. Size 5000×5000 nm^2.

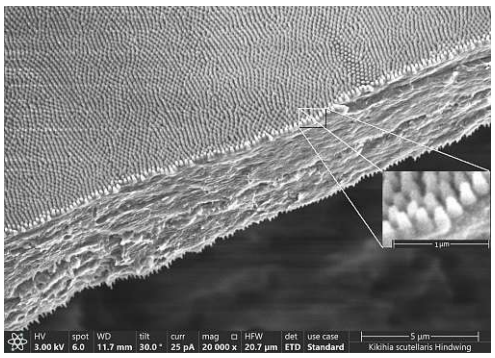

Fig. 70: SEM micrograph of the *K. scutellaris* wing surface.

The nanopillars on the wings of *K. scutellaris* are normally distributed around 241 nm with standard divination of $\sigma = 42$ nm.

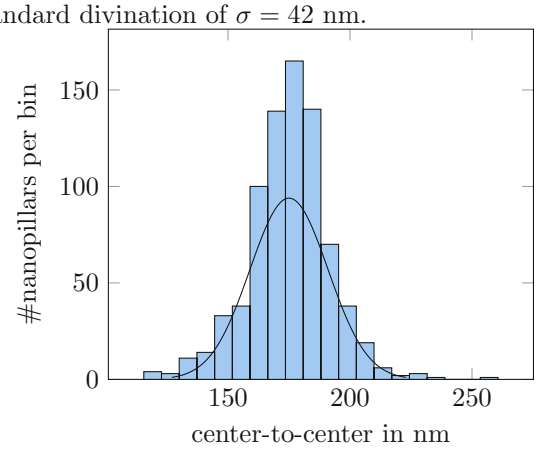

Fig. 71: Histogram of *K. scutellaris* center-to-center nanopillar distance distribution with a mean of 175 nm, a σ of 16 nm and 787 counted nanopillars.

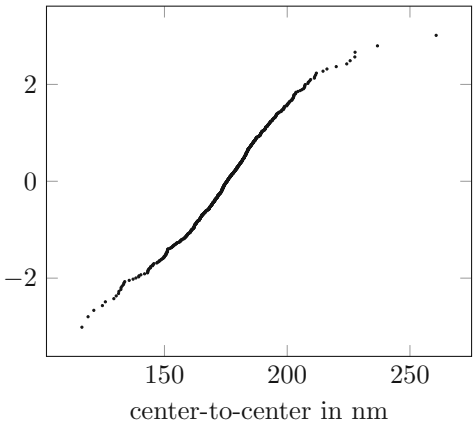

Fig. 72: Q—Q plot of the *K. scutellaris* center-to-center nanopillar distance distribution of Fig. 71.

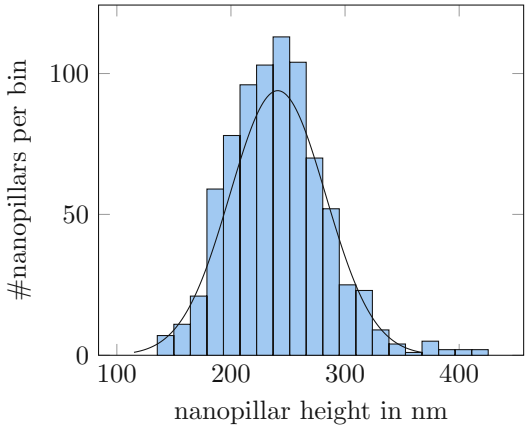

Fig. 73: Histogram of *K. scutellaris* nanopillar height distribution with a mean of 241 nm, a σ of 42 nm and 787 counted nanopillars.

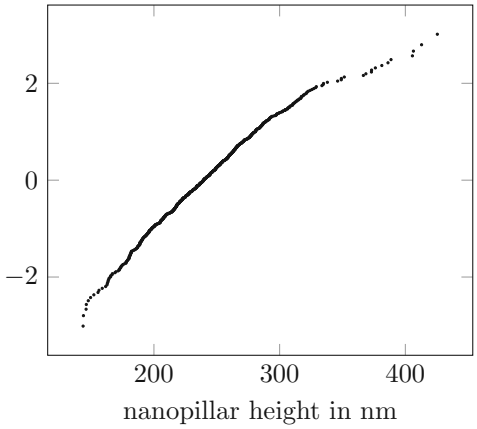

Fig. 74: Q—Q plot of the *K. scutellaris* nanopillar height distribution of Fig. 73.

The detailed SEM micrographs of the *K. scutellaris* nanopillars were used to reproduce the actual geometry of the pillars. The same projection technique was used to reproduce the pillars of *A. cingulata*. The reproduction looks accurate when comparing the geometry with the bottom side seen in Fig. 62 and comparing the resulting height with the height distribution.

Fig. 75: *K. scutellaris* nanopillar geometry

4.3.1 Successful UV resin replica

The replication of the nanopillar structure was successful Figs. 76 and 77. The full height was replicated. Nevertheless, the form of the nanopillars is different compared to the biological template. The replica nanopillar form interferes less with the AFM tip. The AFM tip can reproduce the valleys better because of the reduced tip artifacts (Fig. 17). The different temperatures in the replication process could explain the alternative form of nanopillars. The PVS negative replica was produced at 4 °C and the UV resin was cured at room temperature. If the PVS expanded a little in the warmer temperature, this would cause a narrowing of the inverse nanopillars.

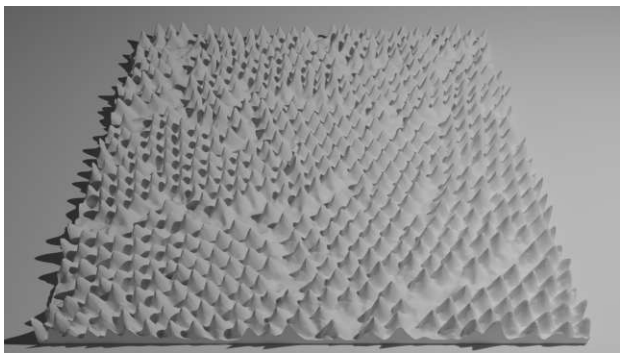

Fig. 76: *K. scutellaris* replica wing surface AFM image. Size 5000×5000 nm^2.

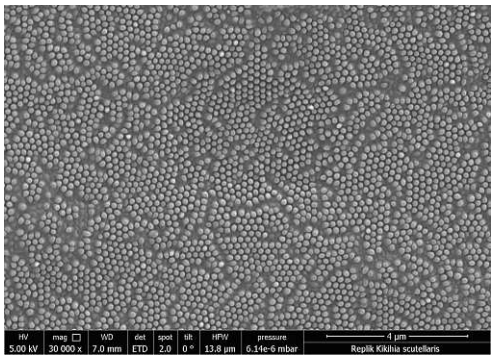

Fig. 77: SEM micrograph of the *K. scutellaris* replica surface. Scale bar 4 µm.

There are missing nanopillars. This diploma thesis did not verify why these pillars were

missing. The nanopillars could have been damaged during the replication technique, or the UV-resin could not fill the cavity because of an air bubble.

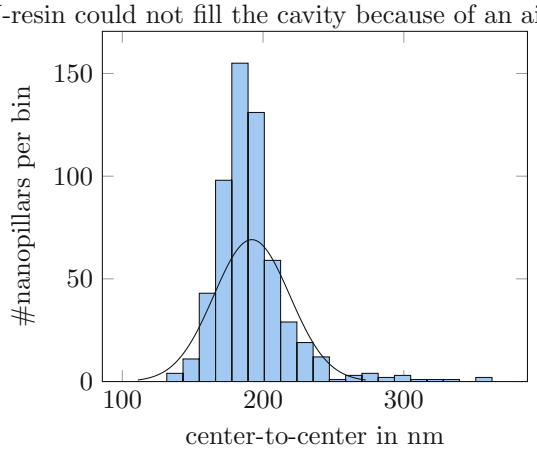

Fig. 78: Histogram of *K. scutellaris* replica center-to-center nanopillar distance distribution with a mean of 192 nm, a σ of 27 nm and 579 counted nanopillars.

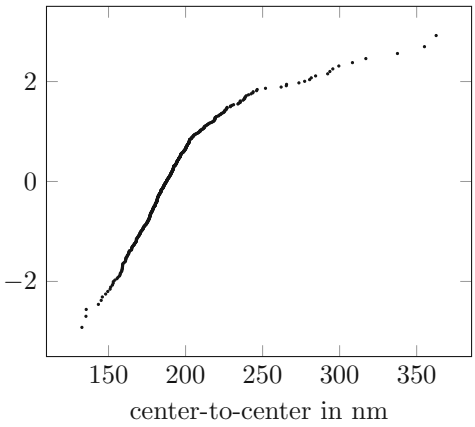

Fig. 79: Q−Q plot of the *K. scutellaris* replica center-to-center nanopillar distance distribution of Fig. 78.

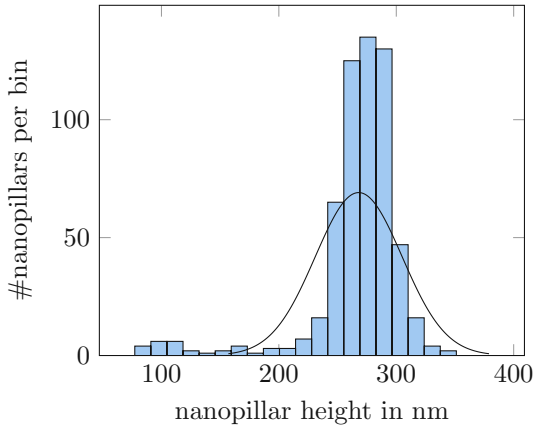

Fig. 80: Histogram of *K. scutellaris* replica nanopillar height distribution with a mean of 268 nm, a σ of 37 nm and 579 counted nanopillars.

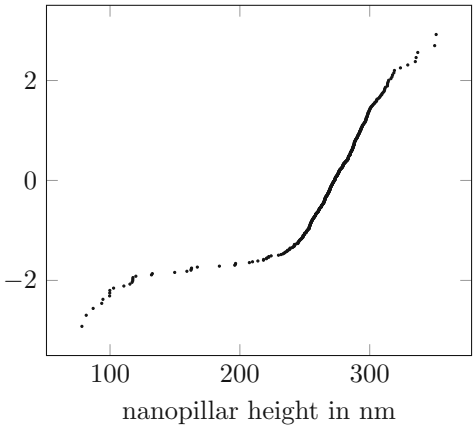

Fig. 81: Q−Q plot of the *K. scutellaris* replica nanopillar height distribution of Fig. 80.

Especially in the histogram of the nanopillar height of the replica, one can see (Fig. 80) that there is a group of shallow nanopillars around 100 nm that could have been the nanopillars that were damaged during the replication process. These shallow nanopillars are also responsible for the Fig. 81 Q−Q plot, indicating a non-normal distribution because the line in the Q−Q plot is not a strait diagonal line.

4.4 Cicada *Magicicada septendecim* - Pharao Cicada

Julia Fisher helped collect the dead insect wings after their mating ceremony in Arlington, Verginia, USA. The wings were sent to Vienna by postal service and so could, in July 2021, be included in this study.

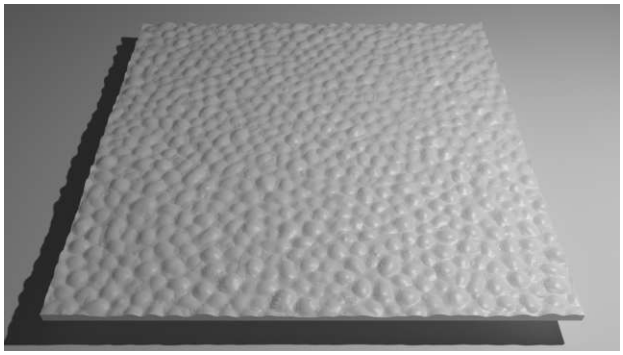

Fig. 82: *M. septendecim* wing surface AFM image. Size 5000×5000 nm^2.

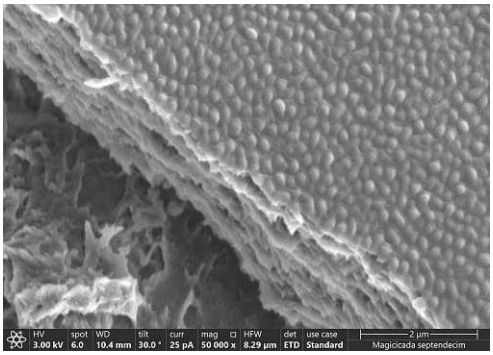

Fig. 83: SEM micrograph of the *M. septendecim* wing surface. Scale bar 2 µm.

The nanopillars on the wings of *M. septendecim* are very low. They are more of a bubbly structure. The hills are just 59 nm high with a standard deviation of $\sigma = 12$ nm (Fig. 86). The surface is completely covered but does not show the (hexagonal) patterning. The mean distance between the hills is 178 nm with a relatively large standard deviation of $\sigma = 23$ nm (Fig. 84). The hill height and center-to-center distance follow nearly a normal distribution and are visible in the Q–Q plot(Fig. 87 and Fig. 85).

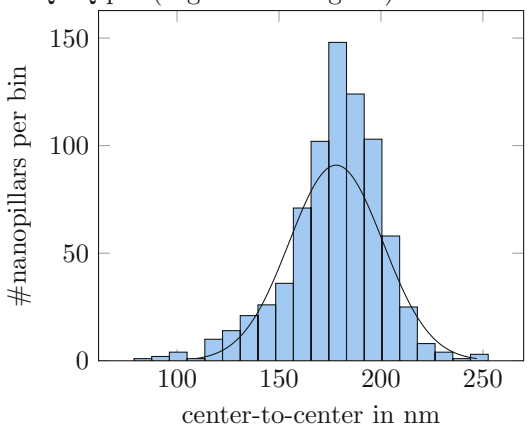

Fig. 84: Histogram of *M. septendecim* center-to-center nanopillar distance distribution with a mean of 178 nm, a σ of 23 nm and 762 counted nanopillars.

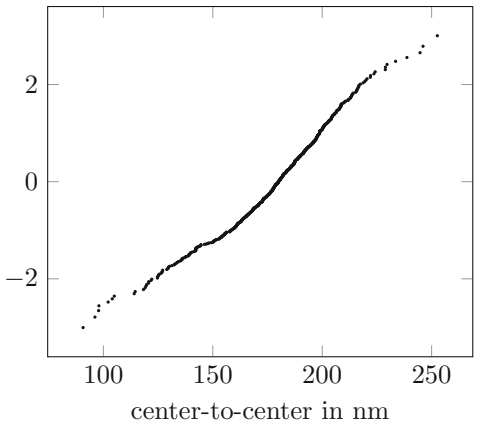

Fig. 85: Q–Q plot of the *M. septendecim* center-to-center nanopillar distance distribution of Fig. 84.

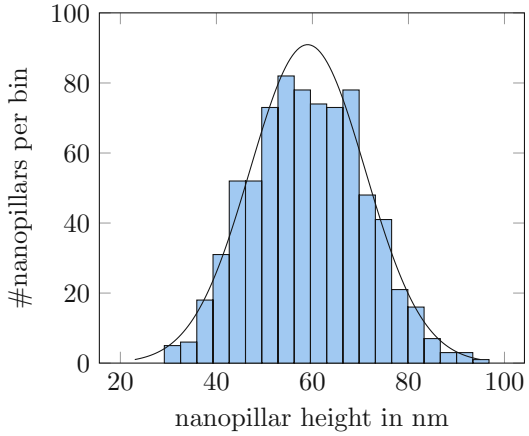

Fig. 86: Histogram of *M. septendecim* nanopillar height distribution with a mean of 59 nm, a σ of 12 nm and 762 counted nanopillars.

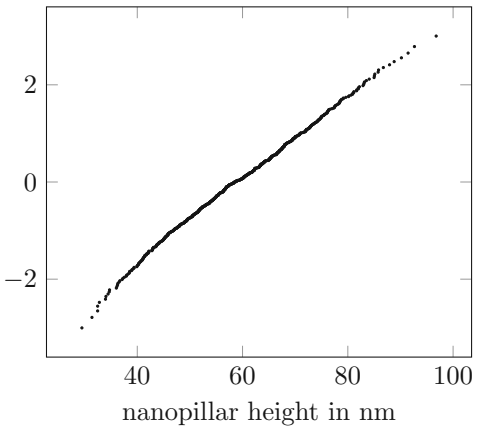

Fig. 87: Q—Q plot of the *M. septendecim* nanopillar height distribution of Fig. 86.

4.4.1 Direct molds

The low pillars of the Pharao Cicada inspired us to the idea of creating a direct resin mold by putting a drop of UV-Resin directly on a fragment of a wing. The sample rested in the dark for the night (for a minimum of 6 hours). That enabled the resin to sink deep between the nanopillars. The next day the resin was hardened by exposure to sunlight. The hardened resin did not adhere to the wing sample and disconnected from the wing almost without force. This technique is no option for high pillars as the forces triggered by curring (heat and shrinking) would break the nanopillar structure.

Fig. 88: *M. septendecim* mold AFM image. Size 5000×5000 nm^2.

Fig. 89: *M. septendecim* virtual imprint AFM image. Size 5000×5000 nm^2.

The AFM scan (Fig. 88) of the mold showed a good reproduction of the inverted nanopillars. To get an impression what the nanopillars reproduced with this stamp would ideally look like, the inverted representation can be calculated. The inverted AFM image (Fig. 89) was made by inverting the values of Fig. 88 before generating the 3D image representation.

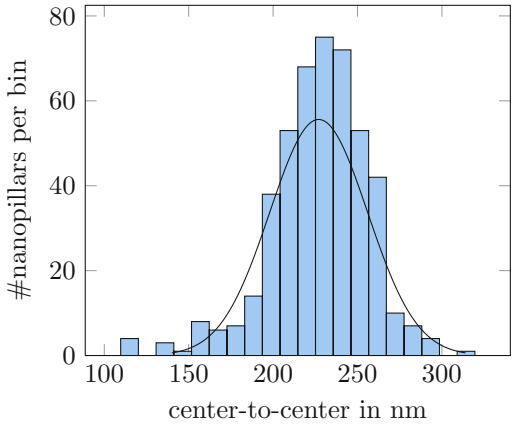

Fig. 90: Histogram of *M. septendecim* replica center-to-center nanopillar distance distribution with a mean of 227 nm, a σ of 29 nm and 466 counted nanopillars.

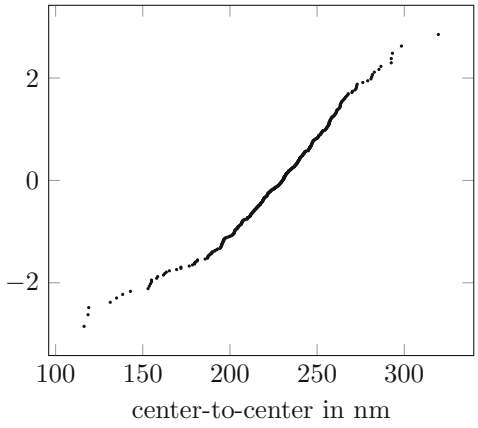

Fig. 91: Q—Q plot of the *M. septendecim* replica center-to-center nanopillar distance distribution of Fig. 90.

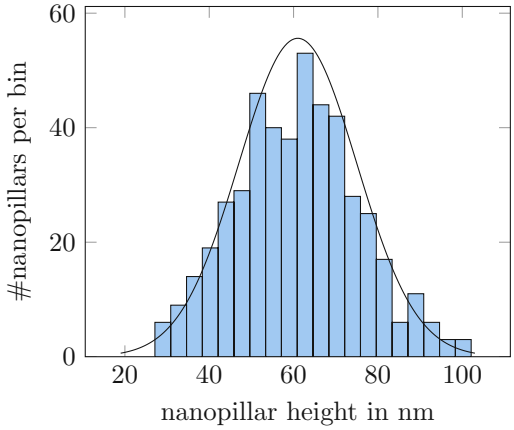

Fig. 92: Histogram of *M. septendecim* replica nanopillar height distribution with a mean of 61 nm, a σ of 14 nm and 466 counted nanopillars.

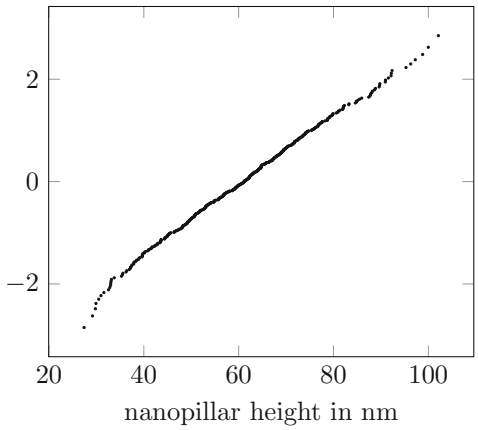

Fig. 93: Q—Q plot of the *M. septendecim* replica nanopillar height distribution of Fig. 92.

Most prominently, the topology of the pillars is different from the wing scan. The AFM artifacts of holes differ from pillars (see Fig. 17). The topology in the image could be misleading. Another point is that the algorithm (section 3.2.3) makes small pillars more challenging to detect. The center-center pillar distance could be reproduced relatively well. The missing (not detected) nanopillars (466 nanopillars per 25 µm^2 instead of 762) could explain the difference.

4.5 *E. coli* survival on wing surface

Determining the quality of the produced replica depends on the antibacterial effect of the wing surface itself. The original wing surface had to be quantified. Furthermore, a control was needed to differentiate the effect of the nanopillars from non-structured surfaces. A Poly-L-Lysin prepared microscope slide and the scaffold represented the controls.

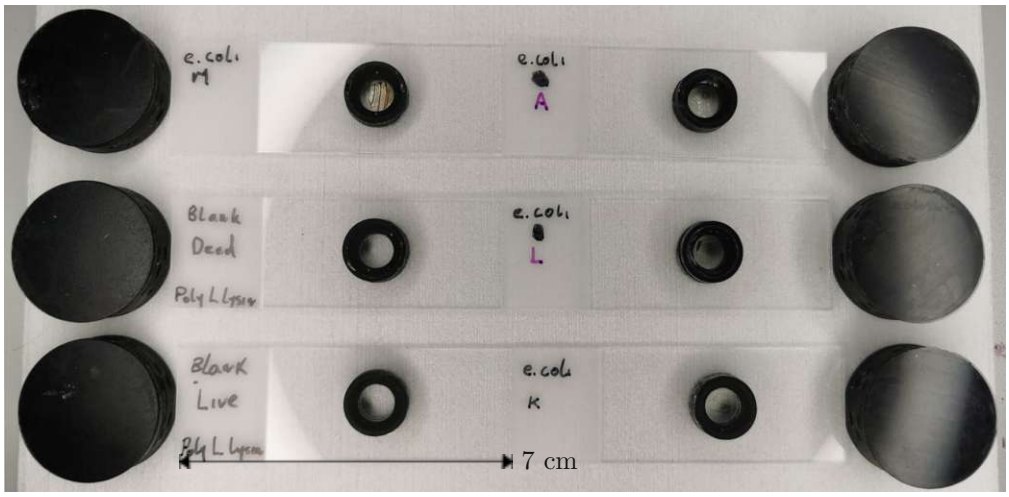

Fig. 94: The first stage of the *E. coli* live-dead experiment, 7 cm glass microscope slides with 5 mm wing disks in attached incubation containers and ready-to-use container caps (light protection). At this stage of the experiments, the containers did not yet have the extended bottom that improved the handling later on.

The 5 mm round wing pieces of every investigated species were mounted on the test slides (see Fig. 94), as described in chapter 3.7.10. The containers are filled with the *E. coli* bacteria solution (100 µl OD_{600} = 0.229) and incubated for one hour. After staining, the slides are wrapped in aluminum foil to protect the setup against bleaching. Note that the "living" denotation meant (in the context of this study) that the bacteria were viable until the fixation in the staining procedure. The methanol ingredient of the last staining step kills the bacteria. The *E. coli* experiments in this diploma thesis were documented with detailed images. The detailed data is omitted from the following chapters for readability reasons but is available on demand (nieuwenhoven@iap.tuwien.ac.at).

4.5.1 Viable *E. coli* on Poly-L-Lysin slides

On the reference Poly-L-Lysin slides the viable *E. coli* were viable as expected.

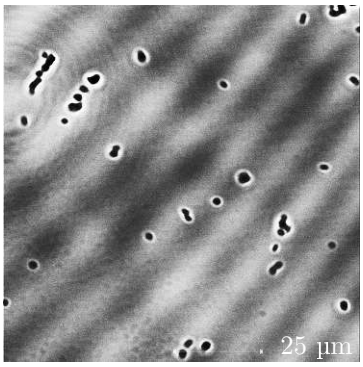

Fig. 95: Bright field (dead and viable) scan of the heat-killed *E. coli* on a Poly-L-Lysin slide. Imaged with CLSM (see 3.8).

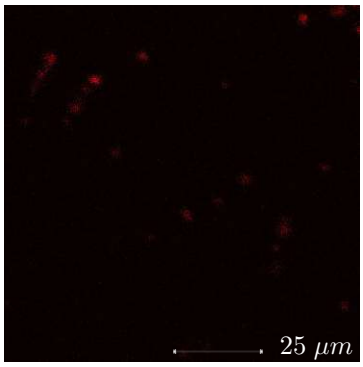

Fig. 96: PI stained (dead) scan of the heat-killed *E. coli* on a Poly-L-Lysin slide. Imaged with CLSM (see 3.8).

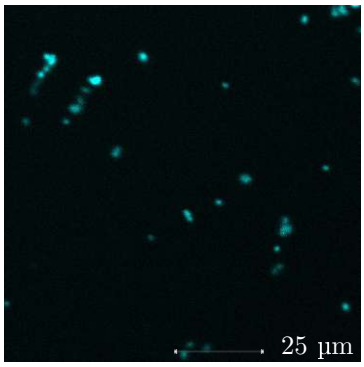

Fig. 97: Hoechst stained (viable) scan of the heat-killed *E. coli* on a Poly-L-Lysin slide. Imaged with CLSM (see 3.8).

As can be seen in Figs. 95 to 97, the majority of the bacteria are living. The light PI staining of some bacteria could have had multiple reasons, from PI leftovers during the fixation to bacteria where PI penetrated the intact membrane. Staining is a statistical process with gray zones.

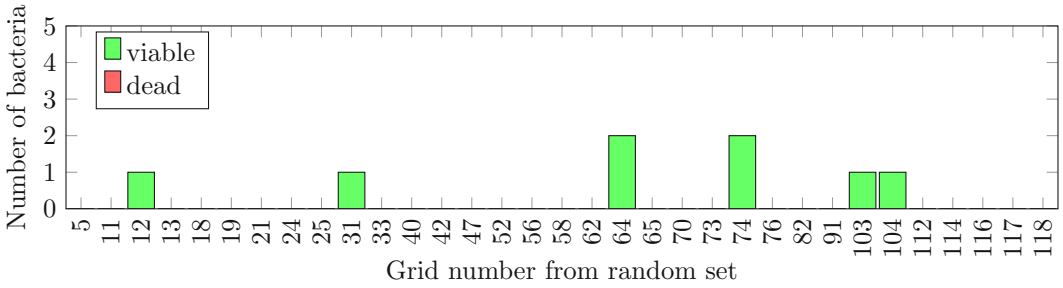

Fig. 98: Reference # of viable and dead *E. coli* viability per 10×10 µm^2 grid area on a Poly-L-Lysin microscope slide with viable *E. coli*, counted grid 0 until including 33

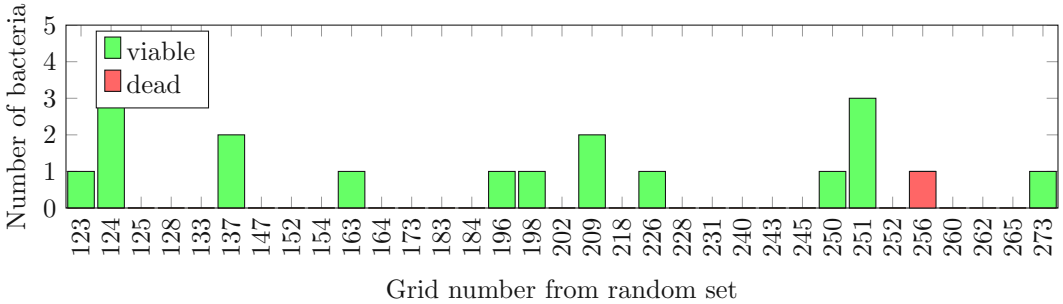

Fig. 99: Reference # of viable and dead *E. coli* viability per 10×10 µm^2 grid area on a Poly-L-Lysin microscope slide with viable *E. coli*, counted grid 34 until including 66

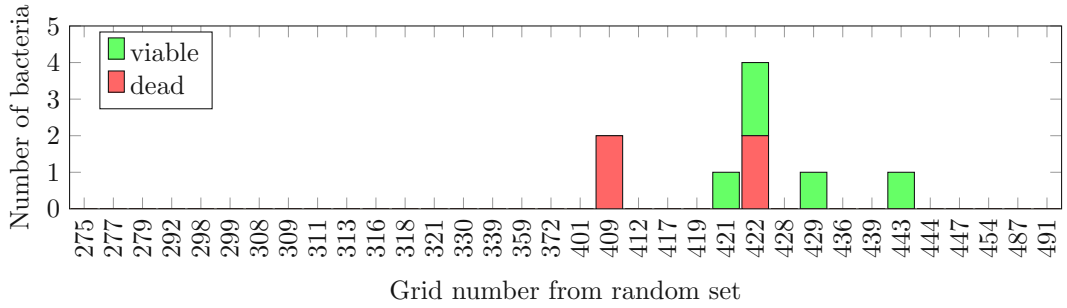

Fig. 100: Reference # of viable and dead *E. coli* viability per 10×10 µm^2 grid area on a Poly-L-Lysin microscope slide with viable *E. coli*, counted grid 67 until including 100

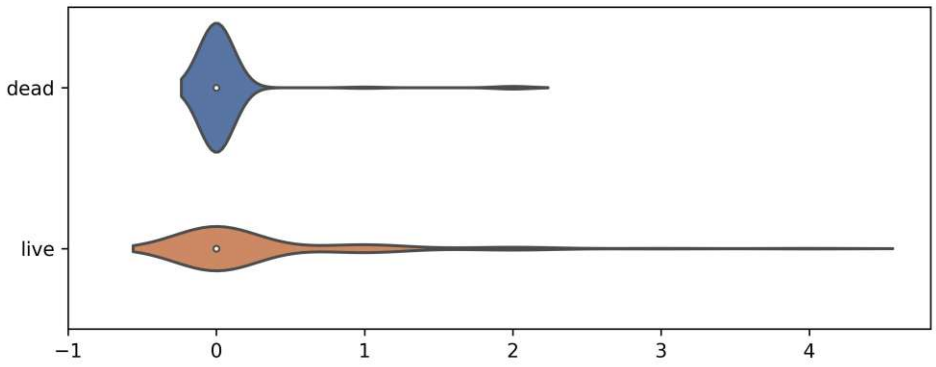

Fig. 101: Reference # of viable and dead *E. coli* per 10×10 µm^2 grid area on a Poly-L-Lysin microscope slide with viable *E. coli*.

Dead *E. coli* per 10×10 µm^2 average: 0.05, σ: 0.30, standard error of the mean (SEM): 0.03.
Live *E. coli* per 10×10 µm^2 average: 0.31, σ: 0.71, SEM: 0.07.

4.5.2 Dead *E. coli* on Poly-L-Lysin slides

The slides with the killed bacteria showed the expected result.

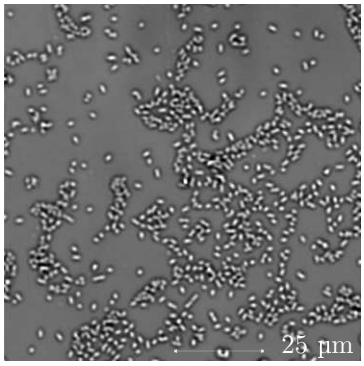

Fig. 102: Bright field (dead and viable) scan of the heat-killed *E. coli* on a Poly-L-Lysin slide. Imaged with CLSM (see 3.8).

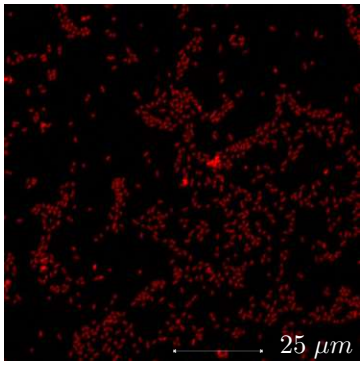

Fig. 103: PI stained (dead) scan of the heat-killed *E. coli* on a Poly-L-Lysin slide. Imaged with CLSM (see 3.8).

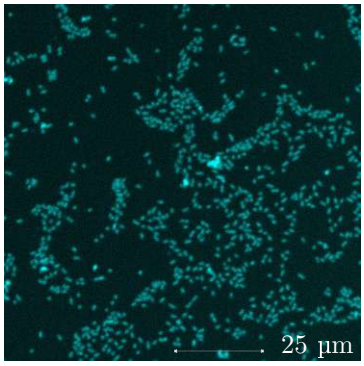

Fig. 104: Hoechst stained (viable) scan of the heat-killed *E. coli* on a Poly-L-Lysin slide. Imaged with CLSM (see 3.8).

The bacteria were heat-killed by heating the slide for two minutes at 95 °C. Near all *E. coli* did not survive the procedure, as can be seen in Fig. 103 where almost all bacteria are PI stained (only bacteria with a damaged membrane were stained with PI).

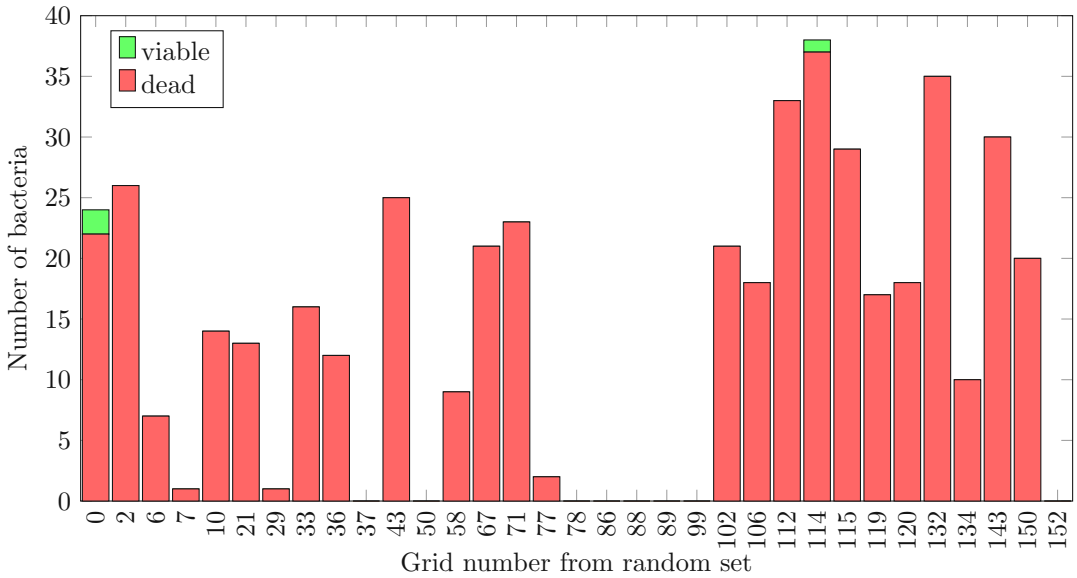

Fig. 105: Reference *E. coli* viability after killing counted grid 0 until including 33

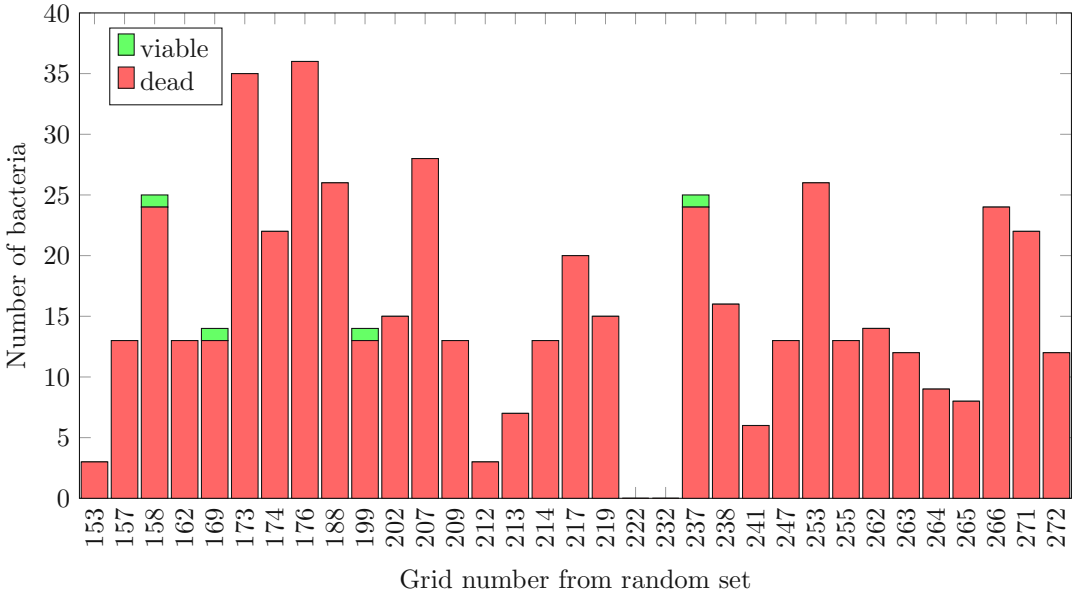

Fig. 106: Reference *E. coli* viability after killing counted grid 34 until including 66

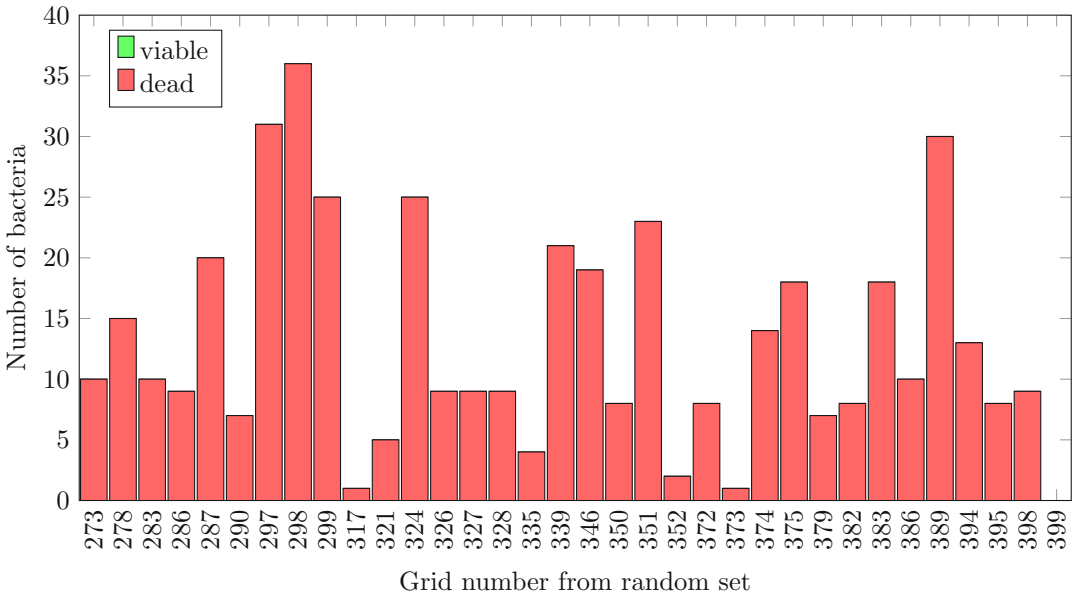

Fig. 107: Reference *E. coli* viability after killing counted grid 67 until including 100

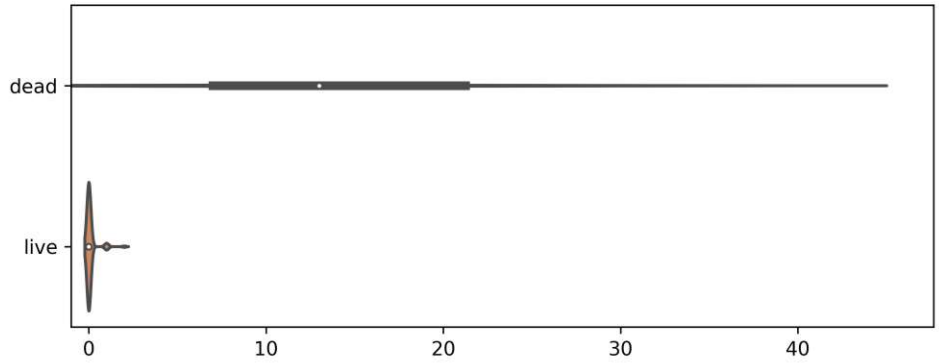

Fig. 108: Reference # of viable and dead *E. coli* per 10×10 µm^2 grid area on a Poly-L-Lysin slide with killed *E. coli*.

Dead *E. coli* per 10×10 µm^2 average: 14.13, σ: 10.06, SEM: 1.01. Live *E. coli* per 10×10 µm^2 average: 0.07, σ: 0.29, SEM: 0.03.

4.5.3 Viability of *E. coli* on *A. cingulata* wing surface

The wing surface of the *A. cingulata* killed bacteria, as can be seen by the PI stained bacteria in Figs. 109 to 111.

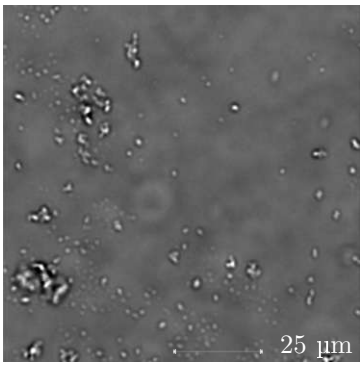

Fig. 109: Bright field (dead and viable) scan of *E. coli* on the *A. cingulata* wing surface. Imaged with CLSM (see 3.8).

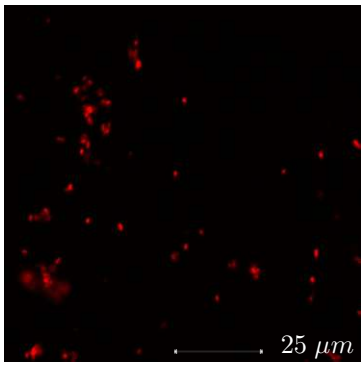

Fig. 110: PI stained (dead) scan of *E. coli* on the *A. cingulata* wing surface. Imaged with CLSM (see 3.8).

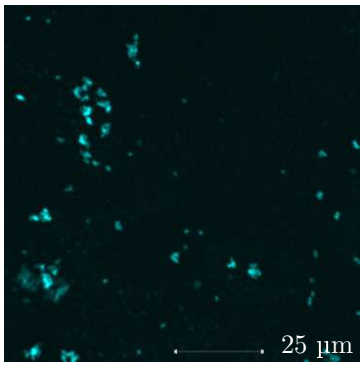

Fig. 111: Hoechst stained (viable) scan of *E. coli* on the *A. cingulata* wing surface. Imaged with CLSM (see 3.8).

Not all bacteria were eliminated, but many of the bacteria did not survive contacting the wing surface. Another interesting problem of this diploma thesis shows up, why are some areas so highly populated and others so sparsely (see Fig. 114)?

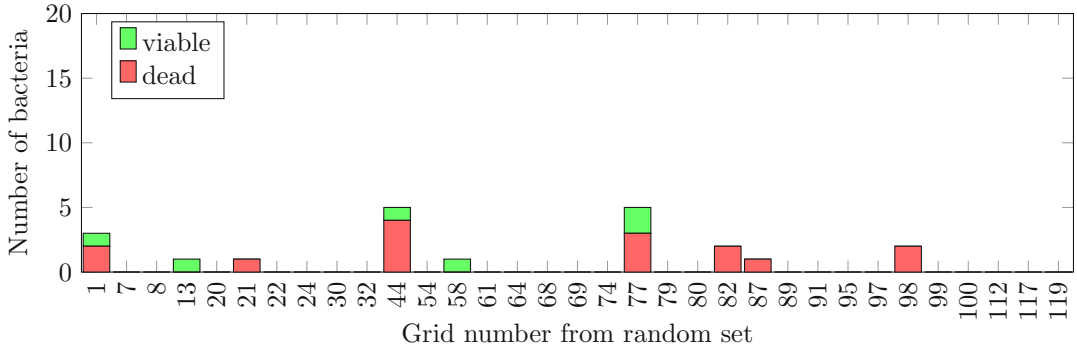

Fig. 112: Reference *E. coli* viability on a *A. cingulata* wing counted grid 0 until including 33

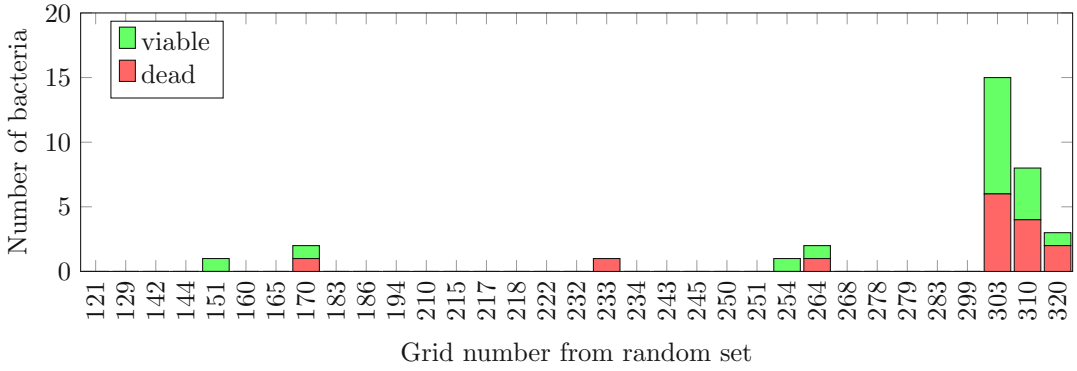

Fig. 113: Reference *E. coli* viability on a *A. cingulata* wing counted grid 34 until including 66

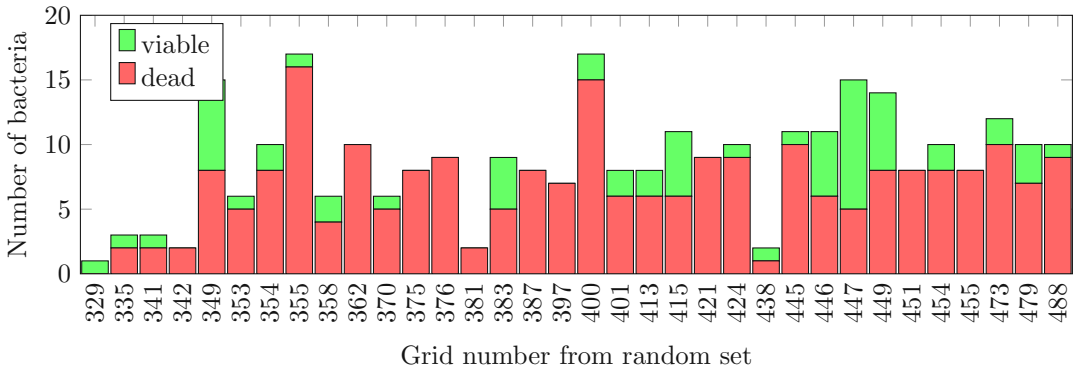

Fig. 114: Reference *E. coli* viability on a *A. cingulata* wing counted grid 67 until including 100

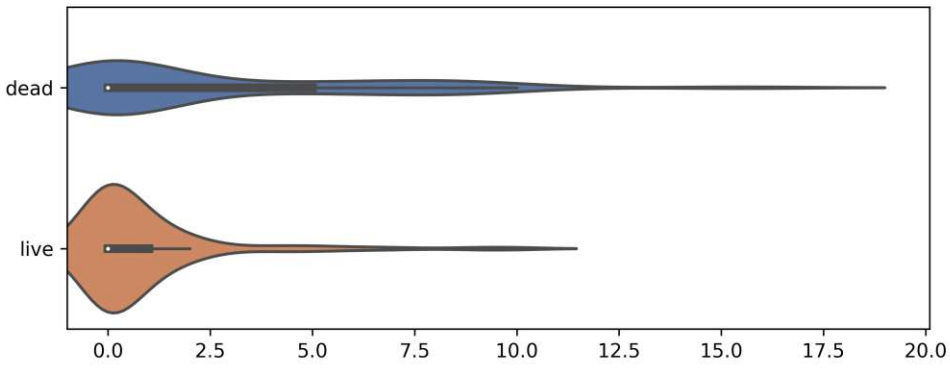

Fig. 115: # of viable and dead *E. coli* per 10×10 µm^2 grid area on a *A. cingulata* wing.

Dead *E. coli* per 10×10 µm^2 average: 2.62, σ: 1.83, SEM: 0.18. Live *E. coli* per 10×10 µm^2 average: 0.88, σ: 3.77, SEM: 0.38.

4.5.4 Viability of *E. coli* on *M. septendecim* wing surface

The wing surface of the *M. septendecim* also kills bacteria, as can be seen in Figs. 116 to 118.

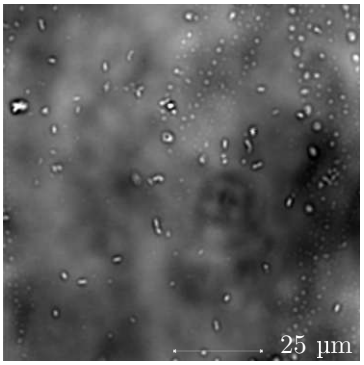

Fig. 116: Bright field (dead and viable) scan of *E. coli* on the *M. septendecim* wing surface. Imaged with CLSM (see 3.8).

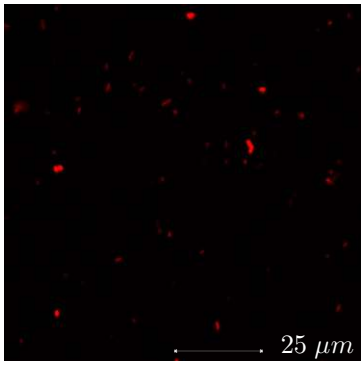

Fig. 117: PI stained (dead) scan of *E. coli* on the *M. septendecim* wing surface. Imaged with CLSM (see 3.8).

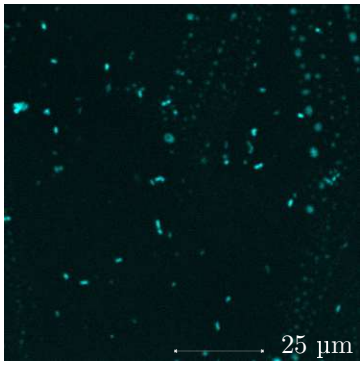

Fig. 118: Hoechst stained (viable) scan of *E. coli* on the *M. septendecim* wing surface. Imaged with CLSM (see 3.8).

Nevertheless, there were viable bacteria on the wing surface. As expected, the low nanopillars did not kill as effectively as the higher pillars of the *A. cingulata*. Because of the very shallow nanopillars, other factors could influence the antibacterial properties of the *A. cingulata* wing surface.

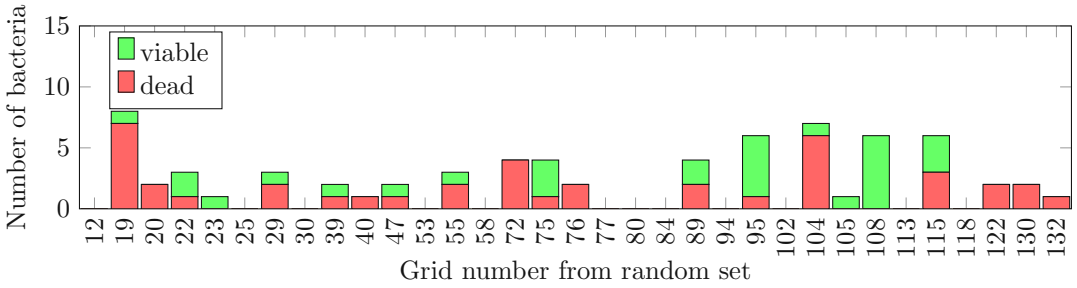

Fig. 119: Reference *E. coli* viability on a *M. septendecim* wing counted grid 0 until including 33

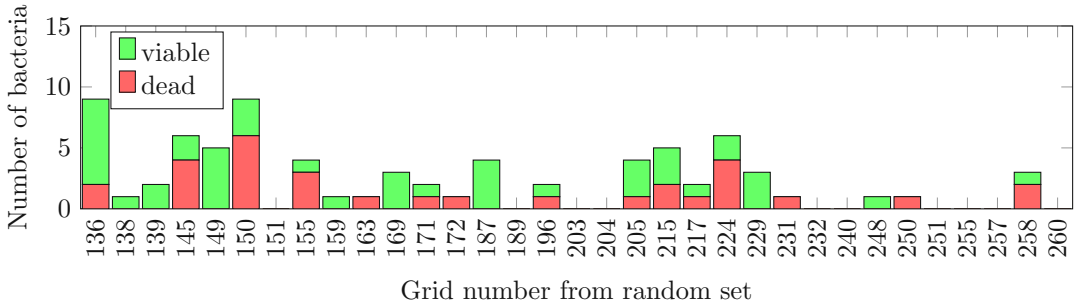

Fig. 120: Reference *E. coli* viability on a *M. septendecim* wing counted grid 34 until including 66

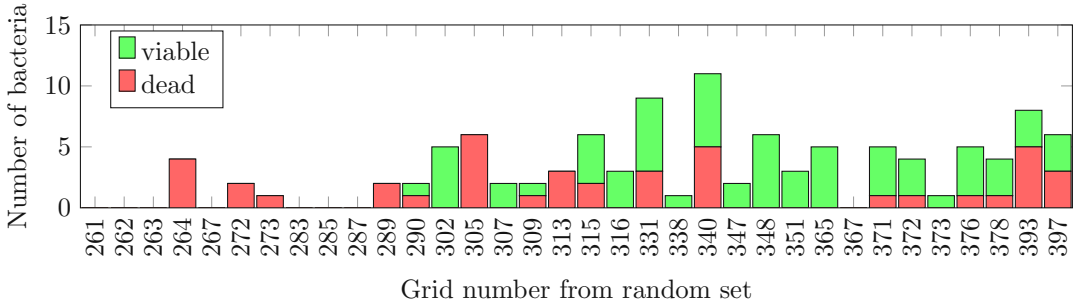

Fig. 121: Reference *E. coli* viability on a *M. septendecim* wing counted grid 67 until including 100

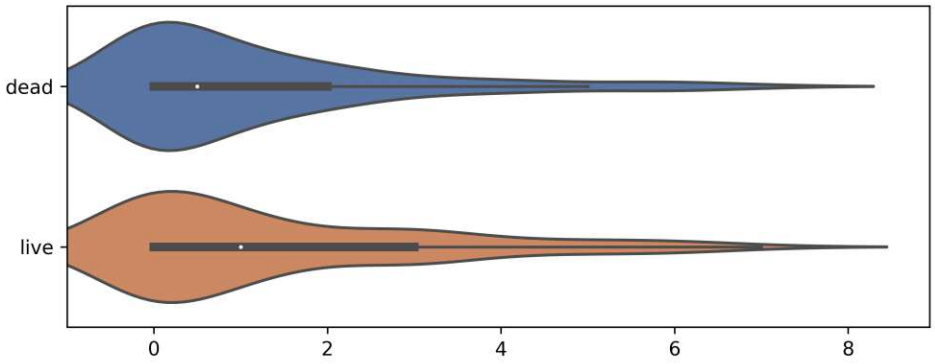

Fig. 122: # of viable and dead *E. coli* per 10×10 µm^2 grid area on a *M. septendecim* wing.

Dead *E. coli* per 10×10 µm^2 average: 1.14, σ: 1.62, SEM: 0.16. Live *E. coli* per 10×10 µm^2 average: 1.40, σ: 1.81, SEM: 0.18.

4.5.5 Viability of *E. coli* on *K. scutellaris* wing surface

The wing surface of the *K. scutellaris* definitely kills bacteria, as can be seen in Figs. 123 to 125.

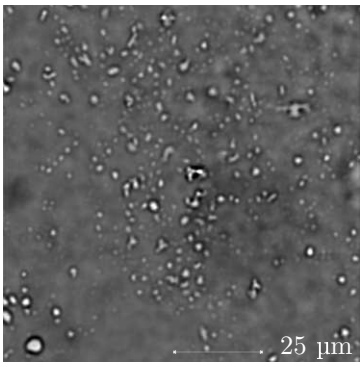

Fig. 123: Bright field (dead and viable) scan of *E. coli* on the *K. scutellaris* wing surface. Imaged with CLSM (see 3.8).

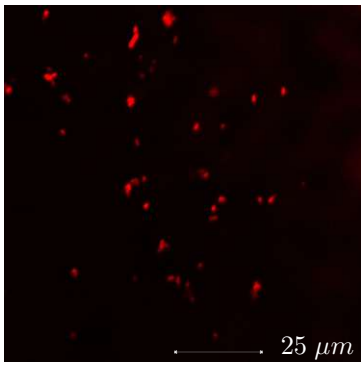

Fig. 124: PI stained (dead) scan of *E. coli* on the *K. scutellaris* wing surface. Imaged with CLSM (see 3.8).

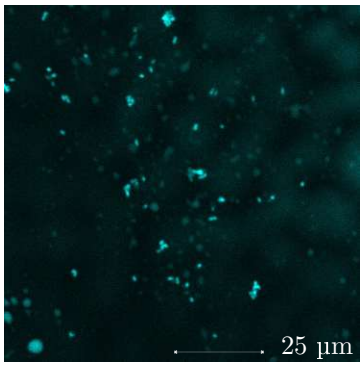

Fig. 125: Hoechst stained (viable) scan of *E. coli* on the *K. scutellaris* wing surface. Imaged with CLSM (see 3.8).

Strangely there survived more bacteria than expected. Because of the high nanopillars, the expectation was that the wings of the *K. scutellaris* were the most deadly ones. This indicates that the tests should be repeated a number of times to rule out any coincidental lower pillars.

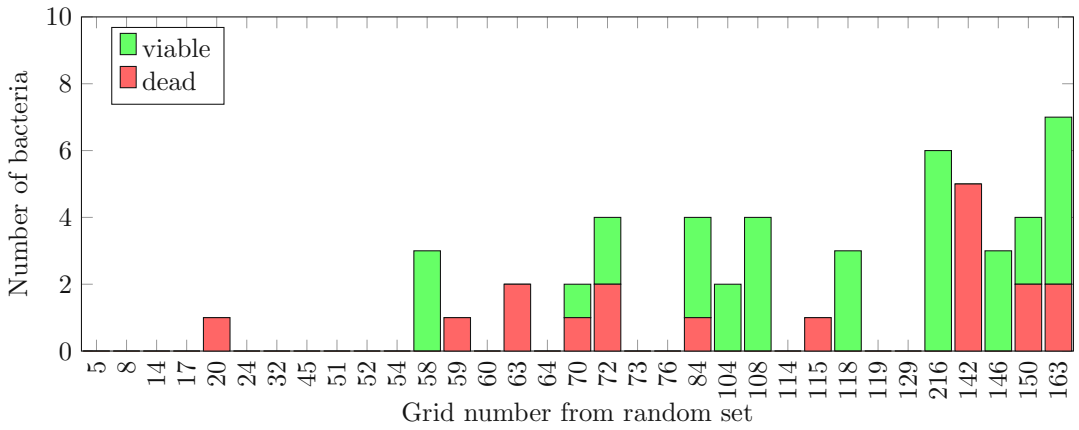

Fig. 126: Reference *E. coli* viability on a *K. scutellaris* wing counted grid 0 until including 33

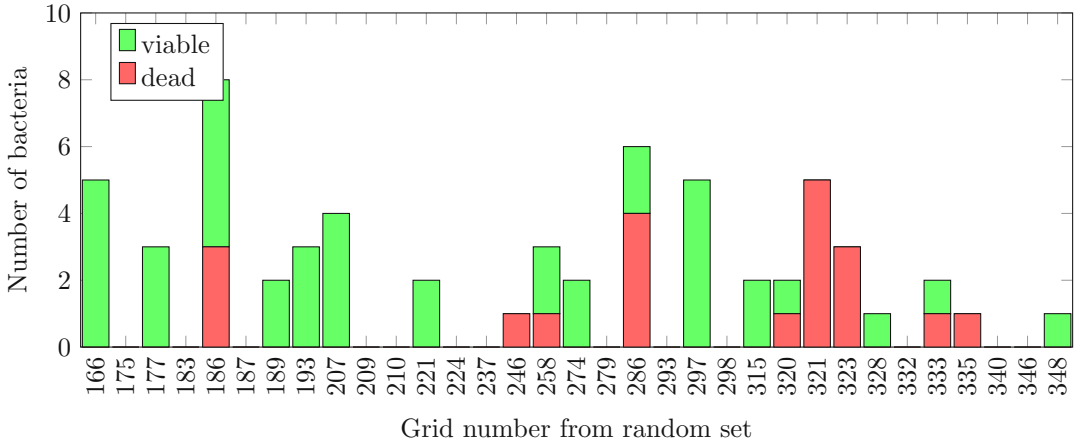

Fig. 127: Reference *E. coli* viability on a *K. scutellaris* wing counted grid 34 until including 66

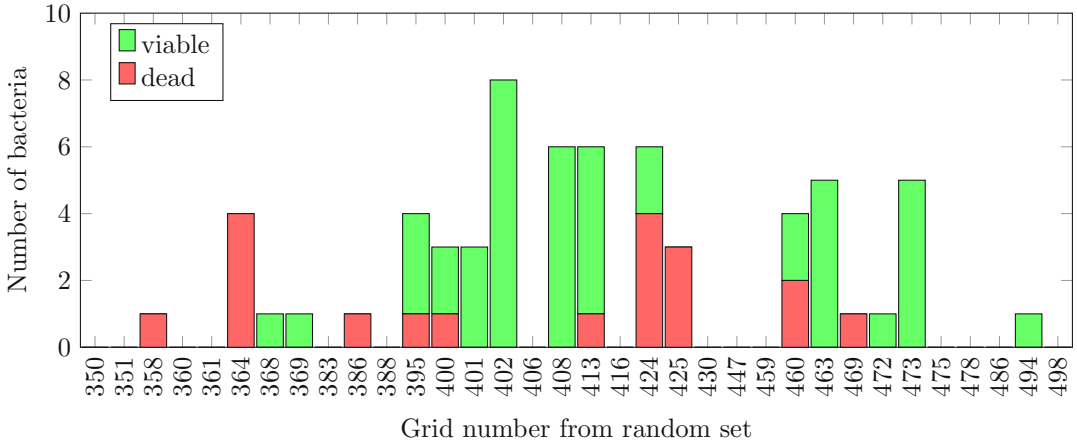

Fig. 128: Reference *E. coli* viability on a *K. scutellaris* wing counted grid 67 until including 100

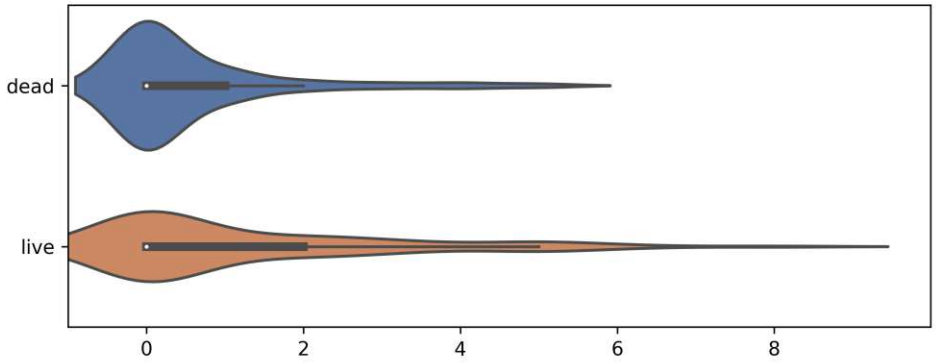

Fig. 129: # of viable and dead *E. coli* per 10×10 µm^2 grid area on a *K. scutellaris* wing.

Dead *E. coli* per 10×10 µm^2 average: 0.57, σ: 1.14, SEM: 0.11. Live *E. coli* per 10×10 µm^2 average: 1.20, σ: 1.82, SEM: 0.18.

4.5.6 Viability of *E. coli* on *S. striolatum* wing surface

The wing surface of the dragonfly *S. striolatum* definitly kills bacteria, as can be seen in Figs. 130 to 132.

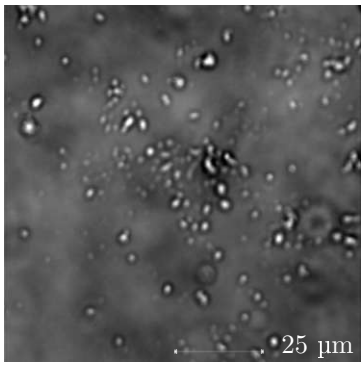

Fig. 130: Bright field (dead and viable) scan of *E. coli* on the *S. striolatum* wing surface. Imaged with CLSM (see 3.8).

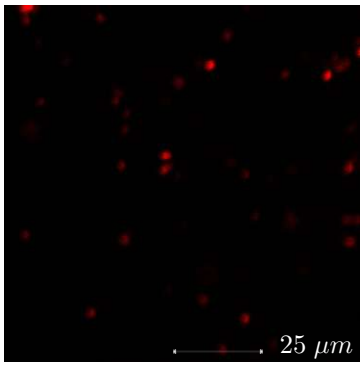

Fig. 131: PI stained (dead) scan of *E. coli* on the *S. striolatum* wing surface. Imaged with CLSM (see 3.8).

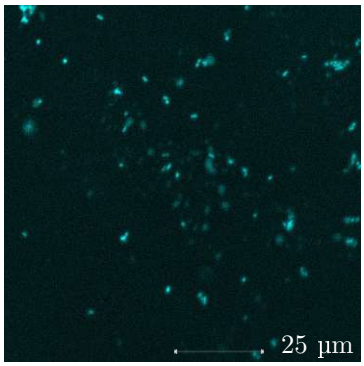

Fig. 132: Hoechst stained (viable) scan of *E. coli* on the *S. striolatum* wing surface. Imaged with CLSM (see 3.8).

The indication that the *S. striolatum* wings had no bactericidal properties because the missing nanopillars were incorrect (see section 4.1). Even if their effectiveness is not as high as on some cicada wings, the bactericidal properties are still definitely present.

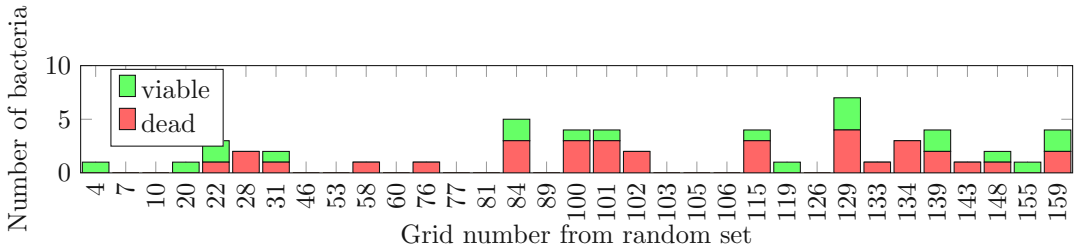

Fig. 133: Reference *E. coli* viability on a *S. striolatum* wing counted grid 0 until including 33

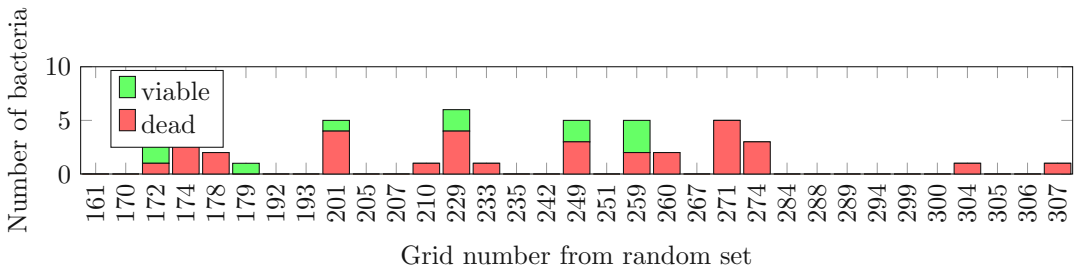

Fig. 134: Reference *E. coli* viability on a *S. striolatum* wing counted grid 34 until including 66

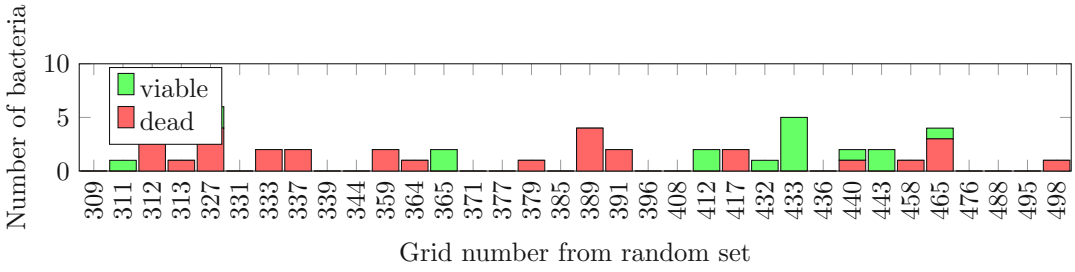

Fig. 135: Reference *E. coli* viability on a *S. striolatum* wing counted grid 67 until including 100

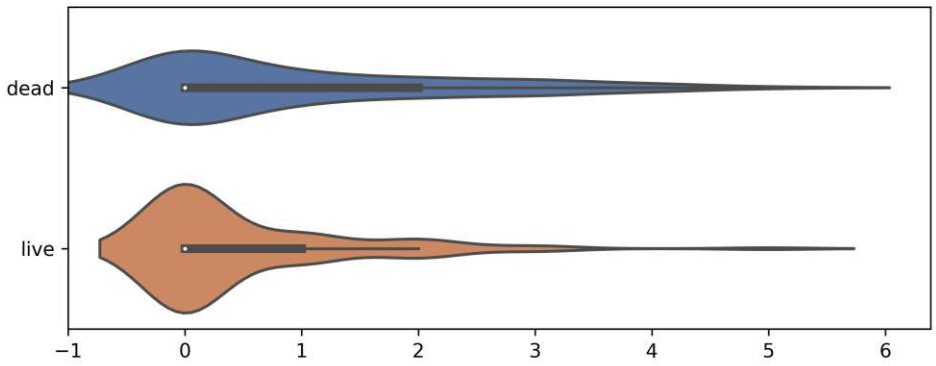

Fig. 136: # of viable and dead *E. coli* per 10×10 µm^2 grid area on a *S. striolatum* wing.

Dead *E. coli* per 10×10 µm^2 average: 0.97, σ: 1.30, SEM: 0.13. Live *E. coli* per 10×10 µm^2 average: 0.50, σ: 0.92, SEM: 0.09.

4.6 *S. aureus* survival on wing surface

The same experiments were executed using *S. aureus* bacteria, here we display only the results. The detailed data is available on demand (nieuwenhoven@iap.tuwien.ac.at).

4.6.1 Viable *S. aureus* on Poly-L-Lysin slides

The base reference of the *S. aureus* shows survival of the *S. aureus* bacteria on the Poly-L-Lysin slides.

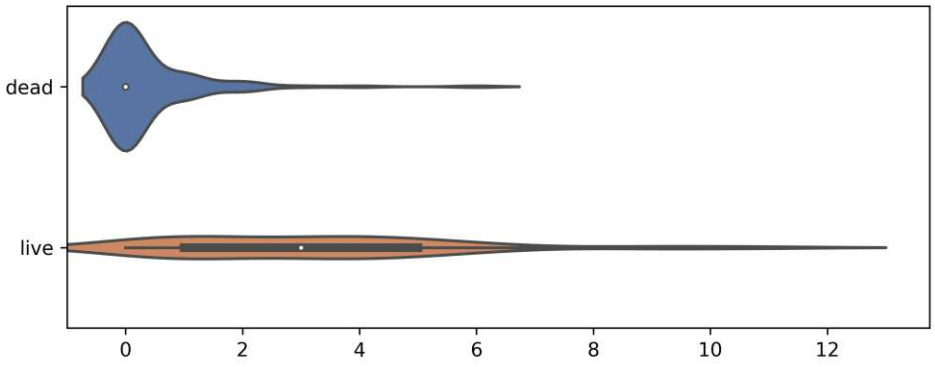

Fig. 137: Reference # of viable and dead *S. aureus* per per 10×10 µm^2 area on a Poly-L-Lysin microscope slide with viable *S. aureus*.

Dead *S. aureus* per 10×10 µm^2 average: 0.04, σ: 0.92, SEM: 0.09. Live *S. aureus* per 10×10 µm^2 average: 3.12, σ: 2.51, SEM: 0.25.

4.6.2 Dead *S. aureus* on Poly-L-Lysin slides

The base reference of the heat-killed *S. aureus* shows PI staining almost all of the *S. aureus* bacteria on the Poly-L-Lysin slides.

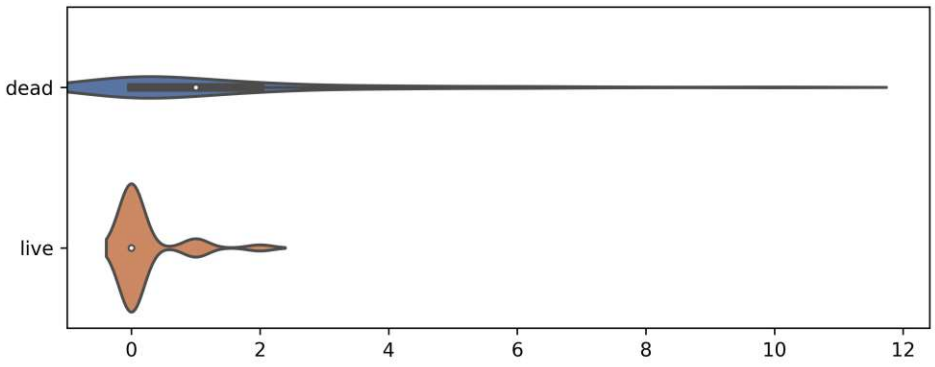

Fig. 138: Reference # of viable and dead *S. aureus* per 10×10 µm^2 grid area on a Poly-L-Lysin slide with killed *S. aureus*.

Dead *S. aureus* per 10×10 µm^2 average: 1.43, σ: 2.18, SEM: 0.22. Live *S. aureus* per 10×10 µm^2 average: 0.20, σ: 0.49, SEM: 0.05.

4.6.3 Viability of *S. aureus* on *A. cingulata* wing surface

Interestingly more *S. aureus* attaced to the *A. cingulata* wing surface as *E. coli* did Fig. 139. This increased attachment could be influenced by the mobility of *E. coli* bacteria. The overall killing efficiency of the wing surface is similar to the one of *E. coli*.

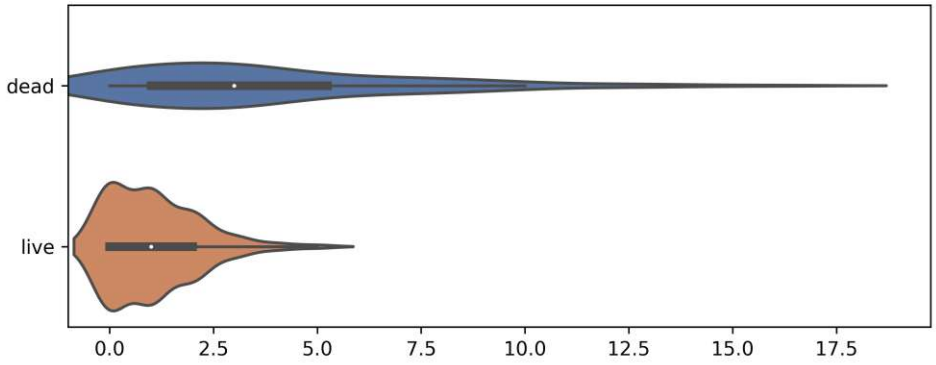

Fig. 139: # of viable and dead *S. aureus* per 10×10 µm^2 grid area on a *A. cingulata* wing.

Dead *S. aureus* per 10×10 µm^2 average: 3.77, σ: 3.39, SEM: 0.34. Live *S. aureus* per 10×10 µm^2 average: 1.04, σ: 1.08, SEM: 0.11.

4.6.4 Viability of *S. aureus* on *M. septendecim* wing surface

The *M. septendecim* wing surface marginally outperformed on *S. aureus* bacteria Fig. 140. However, the killing ratio was also higher for *S. aureus* bacteria.

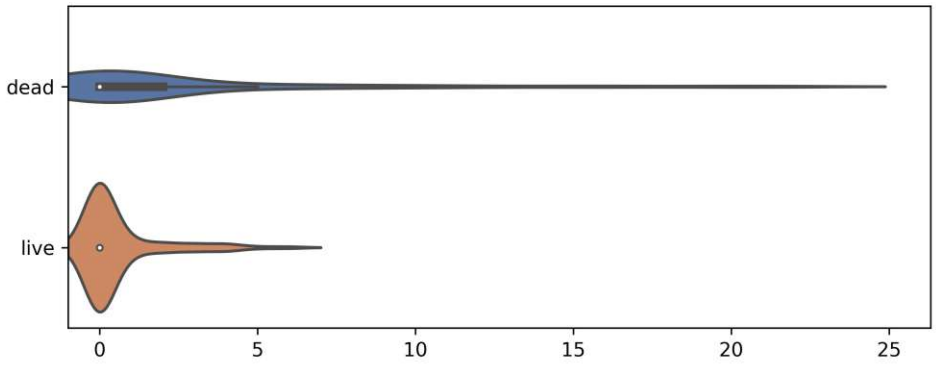

Fig. 140: # of viable and dead *S. aureus* per 10×10 µm^2 grid area on a *M. septendecim* wing.

Dead *S. aureus* per 10×10 µm^2 average: 2.50, σ: 4.87, SEM: 0.49. Life *S. aureus* per 10×10 µm^2 average: 0.56, σ: 1.26, SEM: 0.13.

4.6.5 Viability of *S. aureus* on *K. scutellaris* wing surface

The attachment rate of *S. aureus* the on *K. scutellaris* wing surface was again not very different from *E. coli* Fig. 141. However, the killing ratio was higher.

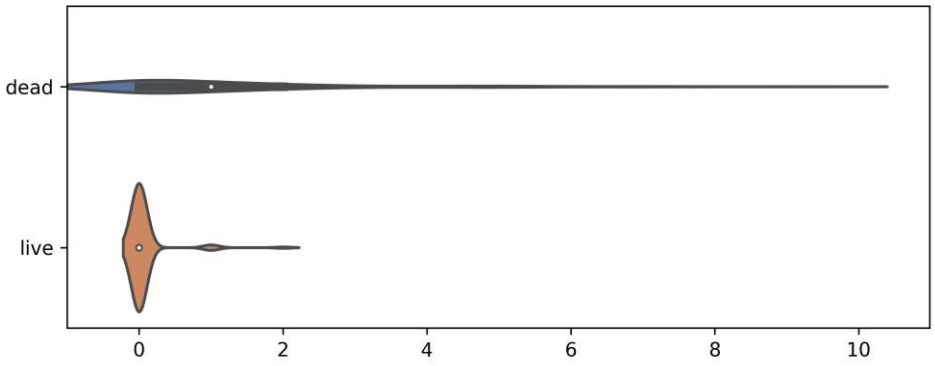

Fig. 141: # of viable and dead *S. aureus* per 10×10 µm^2 grid area on a *K. scutellaris* wing.

Dead *S. aureus* per 10×10 µm^2 average: 1.17, σ: 1.75, SEM: 0.18. Live *S. aureus* per 10×10 µm^2 average: 0.06, σ: 0.28, SEM: 0.03.

4.6.6 Viability of *S. aureus* on *S. striolatum* wing surface

The hairy nanostructures of the *S. striolatum* wing surface were also effective against *S. aureus* Fig. 142. Again, a slightly higher attachment rate and a higher killing ratio was noted.

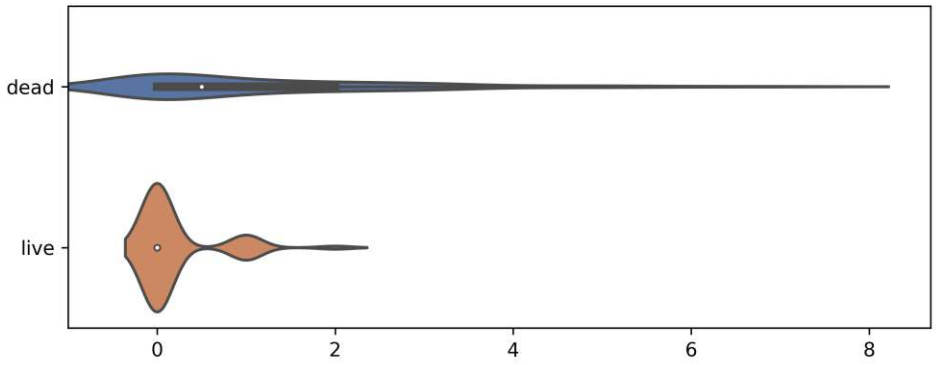

Fig. 142: # of viable and dead *S. aureus* per 10×10 µm^2 grid area on a *S. striolatum* wing.

Dead *S. aureus* per 10×10 µm^2 average: 1.14, σ: 1.53, SEM: 0.15. Live *S. aureus* per 10×10 µm^2 average: 0.20, σ: 0.45, SEM: 0.04.

4.7 *E. coli* survival on wing replica

The killing efficiency on the replica has the extra factor of material toxicity compared to the wing fragments. Therefore a scaffold was created (see Section 3.8.4), with the same composition as the replicas, instead of the Poly-L-Lysin slides as a reference, to be able to estimate the contribution of material toxicity to the results.

4.7.1 Viability of *E. coli* on resin scaffold

The material has some toxicity elements, shown in Fig. 143. However, the difference of the Poly-L-Lysin slide could also be caused by the topology of the scaffold. The topology allows for many more cavities for the bacteria to attach.

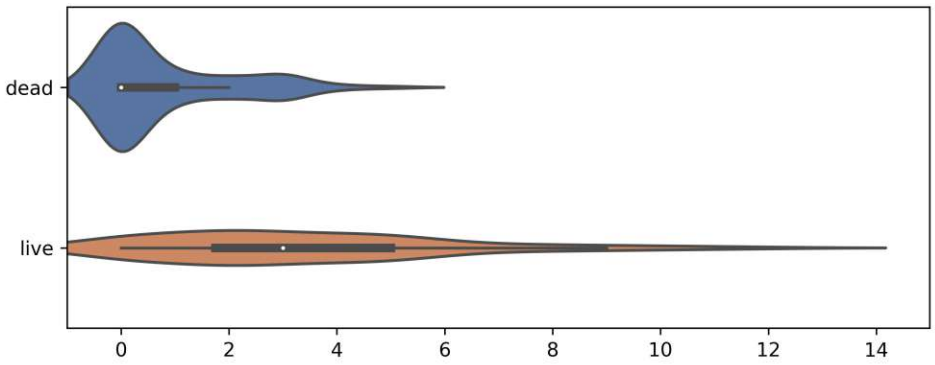

Fig. 143: # of viable and dead *E. coli* per 10×10 µm^2 grid area on a resin scaffold.

Dead *E. coli* per 10×10 µm^2 average: 0.79, σ: 1.23, SEM: 0.12. Live *E. coli* per 10×10 µm^2 average: 3.35, σ: 2.73, SEM: 0.27.

4.7.2 Viability of *E. coli* on *K. scutellaris* wing replica

The replica was effectively killing the *E. coli* as can be seen by comparing the Fig. 144 with the Fig. 143. The ratio between dead and living bacteria is turned around compared to scaffold.

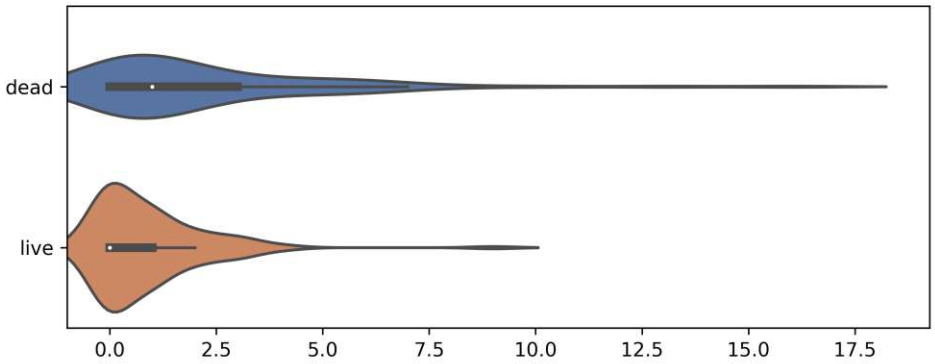

Fig. 144: # of viable and dead *E. coli* per 10×10 µm^2 grid area on a *K. scutellaris* wing replica.

Dead *E. coli* per 10×10 µm^2 average: 2.21, σ: 2.80, SEM: 0.28. Live *E. coli* per 10×10 µm^2 average: 0.90, σ: 1.33, SEM: 0.13.

4.8 Discussion viability experiments

First, we need to evaluate the reference slides (see Figs. 101 and 108). We can see that even the sample with the live bacteria shows some dead bacteria. They can be fixed bacteria stained with leftovers of the PI, or they are some of the first generations that died "naturally". The methanol very efficiently kills the bacteria. The number of attached bacteria indicates that they sink to the bottom and attach better to the slide. At the same time, it indicates that live bacteria are more easily flushed away.

The tests of this diploma thesis show no significant difference in the efficiency of the nanopillar surface between *E. coli* and *S. aureus*. More tests are necessary to confirm this finding because of the high variability in the collected data.

Particular focus was given to the wing of the Lesser Bronze Cicada because of the highest nanopillars. The counting of dead and live bacteria gives fascinating results. For example, more living bacteria are attached to the wing than dead bacteria. This relation lets us assume that the bacteria are sticking more efficiently to the wing surface than to the Poly-L-Lysin layer of the blank slide. Because the number of dead bacteria is much higher than on the blank slide, the conclusion was that the surface continuously catches bacteria and kills them in the process.

The replica of the Lesser Bronze Cicada is unexpectedly even more efficient in killing the bacteria than the original wing fragment. One could interpret that the bacteria are killed faster after connecting to the nanopillars. The faster killing mechanism would also explain why the number of living but attached (to the nanopillars) bacteria is lower than on the original wing. It could also be assumed that some bacteria can escape the attachment to the nono-pillars, but assuming the killing mechanism is faster, the timespan to disconnect becomes shorter.

4.9 Continuous live-dead experiment

The influence of the antibacterial wing surface on the growth of a whole bacteria culture would show the overall effectiveness of the nanopillars.

For this experiment, it is necessary to expose the bacteria solution constantly to a wing nanopillar structured surface. This diploma thesis realized this by replacing the bottom of a tube with a wing sample. The bottom of a 1.5 ml tube was cut off. The 5 mm wing specimen was put on top of a PVS blob. The tube was pressed down (bottom first) on the blob so that the 5 mm wing disk was afterward positioned in the middle of the newly formed PVS bottom of the tube. The 5 mm disk fills up most of the central part of the bottom, so any liquid in the tube would have constant contact with the wing sample.

By keeping 400 µl of bacteria solution in constant contact with a 5 mm diameter wing piece, the influence of the exposure on the growth can be measured. The growth conditions were constant at 37 °C and shaking at 800 rpm. In every measuring interval (at 0, 20, 50, 80, 125, 170, 215 minutes), 100 µl was extracted to do the OD_{600} measurement and replaced by fresh 110 µl LB-Medium. The ten µl extra compensates for the evaporation during the growth process.

Fig. 145: Preparation of wing exposing tubes.

During the experiment, the *A. cingulata* sample was damaged, so it had to be excluded from the experiment results.

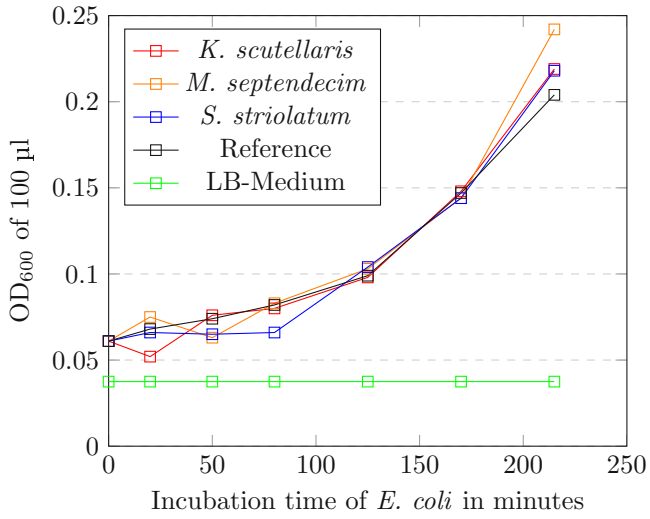

Fig. 146: *E. coli* incubation with differend exposed wing specimen (periodic OD_{600} measurements on 100 µl volume).

The grow curve of *E. coli* (Fig. 146) and *S. aureus* (Fig. 147) shows no significant difference between the reference sample with no exposed wing surface (black) and the probes with exposed wing surface. The antibacterial effect of the surface has no measurable effect on the growth curves, which implies that the effect is locally bound directly to the surface.

The results of this experiment can have different causes. One cause could be that the wing

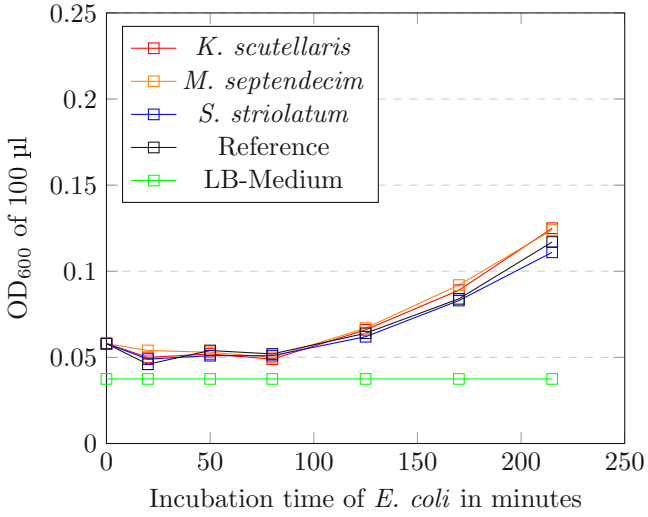

Fig. 147: *S. aureus* incubation with differend exposed wing specimen (periodic OD_{600} measurements on 100 µl volume).

piece was too small for the 400 µl culture to exert an influence. However, the limiting factor of this diploma thesis is the unavailability of enough wing material for tests with more extensive surfaces. Also, it could be that the shaking (which is necessary to provide the bacteria with oxygen and space to grow) is hindering the attachment of the bacteria to the surface. However, the cause could also be that the bacteria overgrow the surface (stacking). After the first layer of bacteria dies, the other bacteria live above the dead remains of the lower layer. They are no longer affected by the nanopillars that were covered by the debris of the dead bacteria.

4.10 Bactericidal efficiency in a wet environment

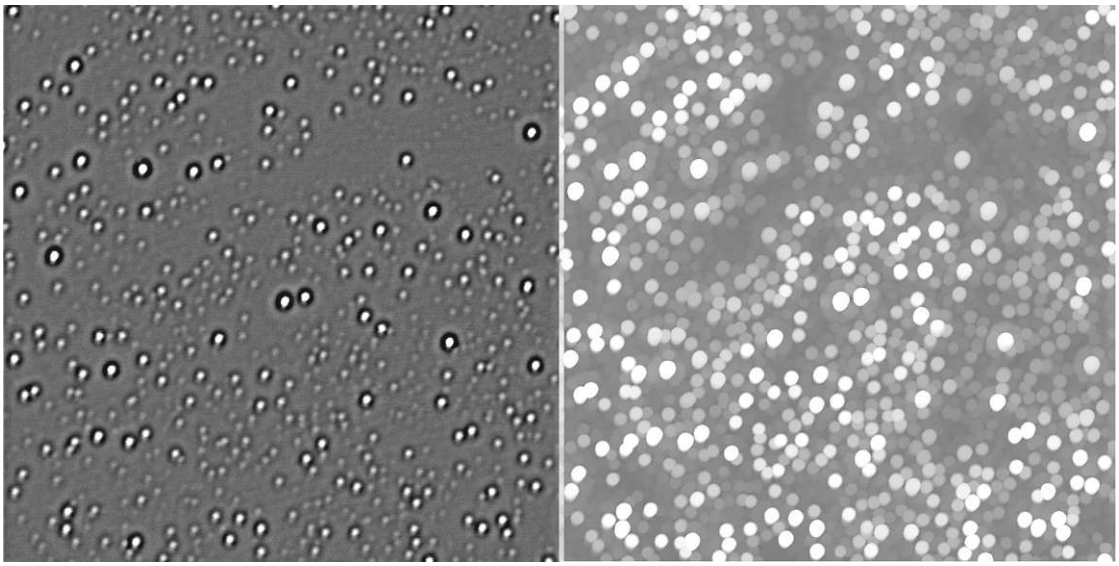

Fig. 148: (left) 100×100 µm^2 *E. coli* bacteria in incubation medium. (right) 100×100 µm^2 detected *E. coli* bacteria in incubation medium (same sample).

In this part of the study, the antibacterial tests simulated a static wet environment. The bacteria solution was incubated directly on top of the nanopillar surface. To evaluate the nanopillar killing efficiency, the number of interactions of the bacteria with the nanopillars should be put in reference to the number of killed bacteria.

The bacteria counting images of the area just above the nanopillars, represent three random spots with a total of 60562 µm^2 imaged area. By applying the Fiji [Sch+12] counting protocol above (see section 3.8.3) which results in 6621 counted bacteria. Assuming a homogeneous distribution of the bacteria, an estimation can be done of $\frac{15000\times15000}{60562} \times 6621 \approx 24.6 \times 10^6$ bacteria in the 15×15 mm^2 area between the two cover slips.

These experimental results indicate that 20 µl solution contains 24.6×10^6 bacteria. This method causes a disturbance in the layer of settled bacteria on the bottom of the incubation chamber, introduced by the pipette tip during entering the medium. The disturbance will remix some of the medium and probably reduce the concentration. Taking into account various possibilities of underestimating the absolute bacteria concentration, 1.2×10^9 per ml can be seen as a lower limit.

Using standard methods of calculating absolute bacteria concentrations from optical density, one can assume 1×10^9 *E. coli* per ml. Other studies used calculations with an exponential curve (x = OD_{600}, y = # bacteria) $y = 5.8137 \times x^{0.9969} \times 0.9979$[Zha+15]. This formula estimates 4×10^{11} bacteria in one ml at $\mathrm{OD}^{600} = 0.7$. One microliter of *E. coli* medium at an OD_{600}=0.7 contains between 1×10^6 and 4×10^8 bacteria.

The incubation container has a diameter of 7 mm and contains 350 µl of *E. coli* medium. Incubation is done in a resting environment so the bacteria will settle and concentrate to the bottom of the container. Especially *S. aureus* will settle and form colonies because they have no mechanical propulsion. The movement of *E. coli* will counter the settlement to a certain degree, but with the building of colonies, the movement will be reduced. The bottom of the well has

a surface of 38.5×10^6 µm^2. In a perfect resting environment, the bottom can be covered by $\approx2\times10^7$ packed bacteria (*E. coli* are approximately one µm by one µm by two µm in size).

In 350 µl there will be at least 3.5×10^8 bacteria, which are enough bacteria in the solution for the settlement of multiple layers with densely packed bacteria. Assuming a perfect settled environment, the nanopillars of the 100×100 µm^2 view window would be in continuous contact with $\approx5\times10^3$ bacteria.

Alternatively, we can assume an active environment and try to estimate the moving interactions with the nanopillars. Therefore, we now investigate at the height of one to two bacteria diameters above the pillars, for *E. coli* we select two micrometers. There is 2×10^4 µm^3 solution on top of the 100×100 µm^2 view window. Using the measured bacteria concentration of 1.2×10^9 per ml, we can assume $\frac{2\times10^4}{10^9}\times1.2\times10^6\approx24$ bacteria in this area during the whole incubation cycle.

E. coli can swim 35 times their length per second [Cha+06] . Using a reduced swimming speed of 20 µm/s and random orientation of the bacteria swimming direction, half of the bacteria would be swimming downward to the nanopillars. The swimming will result in $20\times12\approx240$ interactions with the nanopillar surface per second. During the incubation time of one hour, about 8.6×10^5 nanopillar interactions occur.

The highest bacteria killing efficiency we measured on the replica of the Lesser Bronze Cicada was 221 killed bacteria per 100×100 µm^2 field of view after the one-hour incubation cycle. Using the two approaches of calculating the nanopillar interactions, the resulting killing efficiency is between $\frac{221}{5000}=4\%$ for settled bacteria and $\frac{221}{8.6\times10^5}=0.026\%$ for swimming bacteria. The maximum number of bacteria attached to the nanopillars per 100×100 µm^2 field was 311 (dead and alive on the replica of the Lesser Bronze Cicada), so even assuming that the attached living bacteria will die eventually does not significantly affect the efficiency.

There are, of course, various further possibilities and combinations of estimating the number of bacteria that have interactions with the nanopillars. Nevertheless, the number of bacteria that are in proximity of the nanopillar surface is, in any case, extremely high in comparison to the number of killed bacteria.

4.11 Bactericidal efficiency in a dry environment

The situation is different in a dry (or nearly dry) environment. When bacteria attach to the surface in a dry environment, they are primarily contained in microdroplets of various compositions. Due to the surface tension of these microdroplets and their evaporation, the bacteria are most likely forced towards the nanopillar surface [Haw+22]. The bacteria will probably die as shown in the results for the wet environment (Section 4.10). It is recommended for further studies to investigate this behavior in more detail, especially the possibilities for the bacteria to make close contact with the nanopillars in a dry environment. Under these conditions, the stacking of bacteria on top of each other becomes a problem[Sen+21]. In a dry environment, the removal of the debris becomes a more important issue, as there is no easily available medium to dissolve into. There is no liquid in the vicinity that can help to flush the debris, and the answer to the question how ruptured membranes detach from the nanopillars is also not known.

4.12 Stacking of bacteria

The specimens for the SEM micrograph (Fig. 149) were prepared by drying an incubated wing specimen with dry air. We can see that the area covered by dead bacteria in Fig. 149 is not exposed to any nanopillars anymore. Therefore, it can be assumed that bacteria attaching to the dead bacteria will have no interactions with the nanopillars and therefore, probably, yield

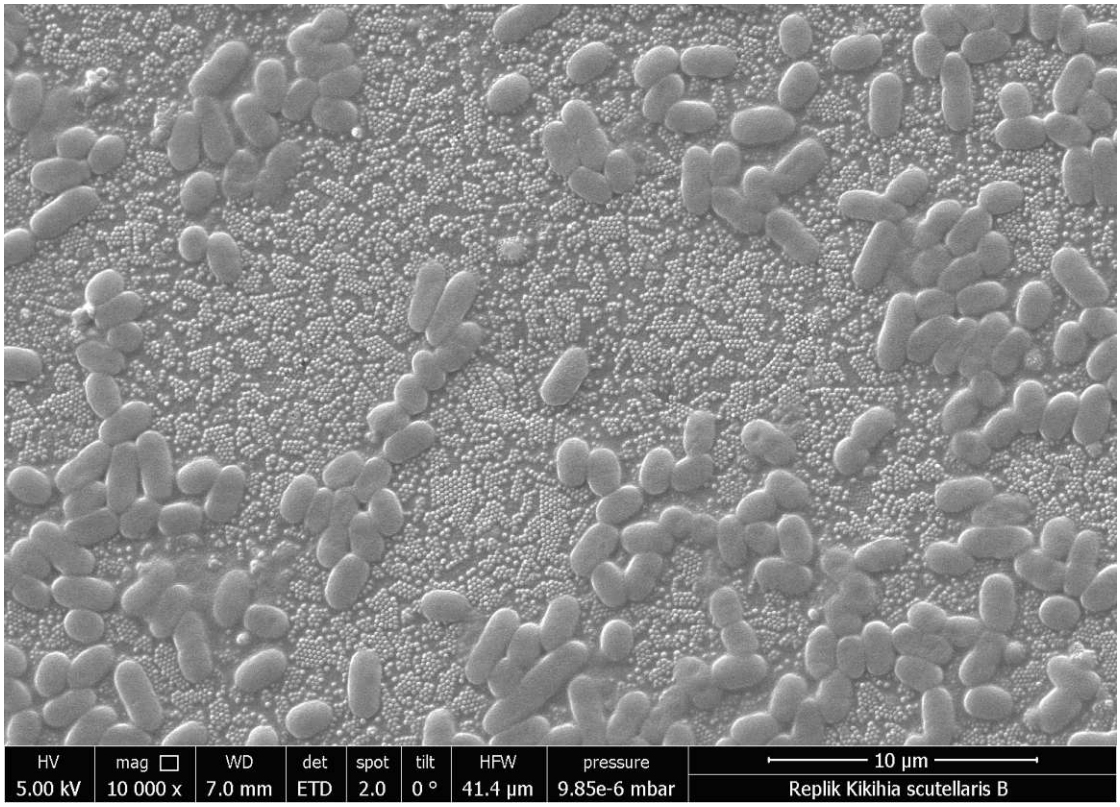

Fig. 149: SEM micrograph of a *K. scutellaris* wing surface dry air dried after one hour incubation.

typical survival ratios as any other bacteria on a dry surface. This diploma thesis did not look directly into this issue and the cleaning properties needed to remove the dead bacteria from the nanopillars. Nevertheless, the procedures needed to clean the wing surfaces from bacteria debris indicate that the dead bacteria are rather rigidly attached to the surface (cleaned wing disks were only reused for testing our developed protocols). As the surface gets more and more polluted with various debris, this will probably result in more and more loss of lethality of the nanopillars under the debris.

4.13 Lessons learned

Some ideas do not work the way one thinks. To help others, here is a list of failures and problems that occurred on the sidelines of this study. There is no explanation given for some points apart from the fact that it did not work. There is no particular order in this list.

4.13.1 Droplets of bacteria on the wings

In the early live-dead bacteria experiments, five µl of stained bacteria solution were deposited directly on the samples. The confocal microscope images were non-conclusive because there were no significant differences between layers near the wing surface and higher layers in the z-stack. A second problem was the droplet diffusion when incubating for extended periods.

4.13.2 Vacuum incubator

Especially when working with resin, a Vacuum incubator (No Name dome with a Pfeiffer vacuum DUO 10 air pump, Pfeiffer Vacuum GmbH, Asslar, Germany) is often used to extract the air bubbles from the resin. The wing nanopillars seem to be a case where a vacuum does not help. Even after a prolonged operation time (30 minutes or more), tiny bubbles formed in the mold near the impression of the wing surface. Suspicion was that some effect in or between the nanostructures influenced the bubbling.

Tests were done to see if the vacuum incubator would support the creation of PVS negative replicas. Nevertheless, the curing was too fast for the bubbles to escape the procedure.

4.13.3 Flat microscope slide as reference sample

A standard glass slide could not be used as a reference sample for live and dead bacteria on a neutral surface because the washing removes all bacteria from the surface. The bacteria do not adhere to the glass slide.

4.13.4 Formic acid to clean the PVS sample

Formic acid can dissolve the organic material of the wings. One possible problem with the molding technique was that the nanopillars could be damaged while separating the wing fragment and the PVS negative replica. Fragments of the nanopillars could be left over in the mold, disturbing the imprinting. However, it seems that formic acid also attacks the PVS material somehow. The mold lost some of its shininess, indicating some reaction. We did not successfully create a good copy from a formic acid-cleaned mold.

4.13.5 AFM images of the PVS negative replica

The PVS material is very soft and flexible, which is the probable reason why AFM imaging of PVS was not conclusive. Suspicion is that the material of the nanopillars somehow sticks to the tip and gets stretched by adhering to the AFM tip.

4.13.6 Speed, slow is better

Especially the UV-resin copies become much better if the resin can sink in over a few hours without hardening (in the dark). Using a high-power UV light source for hardening had negative effects during replication. These adverse effects could have been caused by the heat generated by UV curing, especially when the hardening happens too fast.

4.13.7 Nail top coat to glue the sample

A nail top coat was ideally suited to glue the sample to the slides. Nail top coat glue worked perfectly in all process stages apart from the last. Unter the fluorescence microscope, some nail top coats lit up so intensively that the bacteria were no longer visible.

4.13.8 Nail top coat mold

A nail top coat can also be used to create a single-usage mold. For this, the wing was fixed using double-sided adhesive tape to a microscope slide. Holding the microscope slide vertically, a droplet of top coat spreads slowly over the wing, resulting in a fragile mold. After 30 to 45 minutes, the coat had dried enough to be separated from the wing. Final hardening takes at least 6 hours. The negative replica was kept between two microscope slides during hardening to prevent curling.

The imprinting is done the same way as with PVS. However, the mold is not separable from the epoxy resin. Acetone was used to dissolve the nail top coat of the negative replica.

4.13.9 SuperFlex® resin mold

Following the surprising results of using directly applied photopolymer resin, we assumed that rubber-like photopolymer resin (SuperFlex® from 3dMaterials®, Gyeonggi-do, Republic of Korea) would be even better. Especially because the hardened SuperFlex® resin can be used as a mold for normal photopolymer resin. We failed in the effective separation of cured photopolymer resin and SuperFlex®.

4.13.10 Photopolymer resin mold

Resin for DLP printers needs to be very fluid to enable the printers to move the partly printed objects smoothly through the resin. The high fluidity of the resin also allows it to flow easily into tiny cavities. A surprise came from using the resin (ELEGOO ABS-like photopolymer resin from ELEGOO, Shenzhen, China) as mold, expecting to use formic acid to dissolve the wing from the mold. However, no formic acid was necessary, and the wing detached almost without force. The best results were achieved with an overnight resting phase to let the resin sink between the nanopillars. The resin was cured slowly in ambient light and hardened using a 405 mn lamp. The first results can be seen in Fig. 88. This diploma thesis did not look into the possibilities of creating a positive replica of the resin-based negative-replica.

4.13.11 Methanol killing

Making a reference image for dead bacteria is not as easy as it sounds. The bacteria have to be killed so that the results can be compared to the living bacteria. Heat-killing bacteria with two minutes at 95 °C had a few problems. The two minutes are almost too short for the heat to reach the center and kill the bacteria there. More prolonged exposure to the high temperature causes much evaporation, creating clumps of bacteria that were difficult to separate in the imaging/counting process. So we switched to methanol killing as the more effective method.

4.14 Art and Science

Art and science are tightly interconnected creative disciplines that give seeds of inspiration to each other. The profile of the nanopillar surface looks like the groove on a long-playing record. The profile led to the idea to use the topological data of the AFM scans (see Fig. 150) to create a music composition. Different geometrical profile paths like spirals, circles, and zig-zags (see Fig. 151) of the nanopillar wing surface were used to create sounds as if they were the grooves in a long-playing record. In the context of this study, a newly written java program extracted the profiles and converted them to wav audio files. Nina Bauer got inspiration from the triangle between the bactericidal properties, the sounds cicadas produce, and the created sounds to produce a music composition. Use the provided QR (see Fig. 152) or follow [BN21] to listen to the composition.

Fig. 150: *K. scutellaris* wing surface AFM image. Size 5000 × 5000 nm

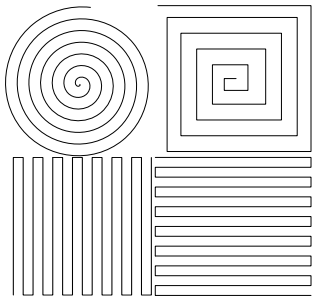

Fig. 151: geometrical profile paths through the nano topology of the wing surface

Fig. 152: QR code to cicada music

5 Conclusion and Outlook

In this work, the antibacterial properties of insect wings were evaluated and compared to the antibacterial properties of replicas with nanoscale precision produced using PVS-based stamping techniques. The *S. striolatum* wing has antibacterial properties, but the hairy-like structures were not replicable with the developed PVS replication technique.

The heights of the nanopillars varied not only between species but also between different parts of the wing. All wing surfaces show good killing efficiency. Even the shallow nanohills of the *M. septendecim* wing surface killed bacteria. The suspicion was that other influences like chemical composition were involved. Notable is that the *S. aureus* was also killed by the nanopillars. There were not enough tests to prove the efficiency compared to *E. coli*, but significantly more *S. aureus* was killed on the wing surface as on a Poly-L-Lysin slide. The variation of the nanopillars hinders the usage of basic statistical comparison tests between the replica with the original topology because two areas on the same wing will already have a statistically significant difference in the height parameter.

A difficulty is that a significant structure diversity of the bacteria colonies is visible on the tested fragments. In some places, many more bacteria were attached to the surface, and in others, only singular ones. These differences make comparing the surfaces impossible. Small colonies could be explained by normal bacteria behavior. When one bacterium out of a colony attaches to the surface, the others slowly roll down and spread to the nanopillars and attach themself. However, this does not explain why some areas are extraordinarily populated and others very sparsely. These areas could have been influenced by the local nano-structural differences and many other natural differences. Further studies should be done with artificially created nanopillars with the same topology as the wings of the cicadas in this study. The homogeneity of the artificial surface makes much better comparative and reproducible results possible.

A successful replication technique to transfer nanostructures from the insect wings to the resin replica was developed. These replicas were also effective as antibacterial material. Further studies could extend the replication technique to copy an artificially created nanopillar surface inexpensively.

The sparse resources of insect wings were a significant problem. Every experiment had to be evaluated very carefully not to waste wing fragments. Many more experiments could be done to fine-tune the replication technique. Further studies should do this fine-tuning using artificially created nanopillars surfaces.

Apart from the fact that the bacteria are killed more or less efficiently, there are more bacteria on the surface than on a flat surface like the poly-lysin slides. This higher number of bacteria should also be seen as a problem in itself. Primarily with a material surface that functions for bacteria as a hub, like a door handle. The bacteria can survive long enough on the surface to transfer to the next host. In the short period after incubation/infection, there are more bacteria alive on the surface with nanostructures than on a flat surface without anything for the bacteria to hold on to.

Reducing the temperature to 4 °C during casting and curing the PVS enables the creation of cicada wing surface replicas with nanoscale precision. Experiments, where the photopolymer resin is cooled during the curing process are ongoing and we expect even more detailed reproductions. The photopolymer replica was precise enough also to reproduce the functionality.

These results indicate that hydrophobicity of the surface hinders the bacteria from reaching the nanopillars in the first place. The same effect was detected on the wing and the photopolymer replica. When the bacteria overcome the hydrophobicity and make contact to the nanopillar surface they are destroyed. Considering the high concentration of bacteria used in the tests, in comparison to the one potentially occurring on insect wings in Nature, stacking of bacteria

on top of the bacterial debris is unlikely to regularly occur in a natural environment. Therefore, stacking and its related problems are improbable evolutionary selection criteria during the evolution of the nanopillar surfaces. As publications [Sen+21]; [Haw+22] state for the reproduction of the antibacterial effects by artificial surfaces, the reproduced surface needs to reduce its hydrophobicity and any self-cleaning mechnism that hinders stacking.

The testing procedures for the antibacterial properties have many variants and parameters. As already stated in other studies [Sen+21]; [Haw+22] these procedures should be harmonized to obtain more comparable results from different studies. We encourage further studies to discuss our results and look deeper into the topic of the overall efficiency of nanopillar surfaces as mechanical bactericides.

6 Acknowledgments

First of all, my thanks go to Alexander Buerger for the many hours of shared troubleshooting the many stones on our shared way in this study. Next, of course, Ille C. Gebeshuber, who did a great job as my supervisor and mentor by focusing the diploma thesis on the research target. Only lightly correcting when necessary on the way when the focus dimmed. Markus Valtiner must be thanked immensely for the many resources, like the hundreds of hours of AFM time he made available to this study. Heinz Redl is thanked for supporting this diploma thesis with Micro-CT scans. Special thanks go to Adelheid Elbe-Bürger and Philip Kienzl for the perfect introduction to Lab techniques and the protocols necessary for research on bacteria, not to forget the access to the confocal fluorescence microscope of the University Hospital Vienna.

The typesetting was done with LaTeX.

7 Appendix

7.1 OpenSACD scripts

7.1.1 reactor_well.scad

This is the script for generating the incubation contaigners (see Figs. 33 and 34).

```
$fn = 96;

/*
 * incubation container with outer radius and baseplate
 * with the side as side size.
 */
module container(radius,side) {
difference() {
    union() {
        cylinder(h=5, r1=radius, r2=radius, center=false);
        translate([-side/2,-side/2,0])
            cube([side,side,1],false);
        translate([-side/2,side/2-0.5,0.5])
            cube([side,1,2],false);
        translate([-side/2,-side/2 -0.5,0.5])
            cube([side,1,2],false);
        translate([side/2-0.5,-side/2,0.5])
            cube([1,side,2],false);
        translate([-side/2 -0.5,-side/2,0.5])
            cube([1,side,2],false);
    }
    translate([0,0,-0.1])
        cylinder(h=5.2, r1=radius-3, r2=radius-3, center=false);
    translate([0,0,2.1])
        cylinder(h=3, r1=radius-3.5, r2=radius-1, center=false);
}
}
/*
 * create a cap with the specified radius and height. around the
 * cap air holes are added that allow only indirect light entry.
 * connectr is the radius of the container, where the cap should fit.
 */
module cap(connectr,radius,height) {
difference() {
        cylinder(h=height, r1=radius, r2=radius, center=true);
        cylinder(h=height-4, r1=radius-2, r2=radius-2, center=true);
    translate([0,0,3])
          cylinder(h=height-4, r1=connectr, r2=connectr, center=true);
    rotate([0,0,0])
        translate([0,radius-2,0])
        rotate([0,90,0])
          cylinder(h=30, r1=.8, r2=.8, center=true);
```

```
43      rotate([0,0,90])
44          translate([0,radius-2,0])
45          rotate([0,90,0])
46            cylinder(h=30, r1=.8, r2=.8, center=true);
47      rotate([0,0,180])
48          translate([0,radius-2,0])
49          rotate([0,90,0])
50            cylinder(h=30, r1=.8, r2=.8, center=true);
51      rotate([0,0,240])
52          translate([0,radius-2,0])
53          rotate([0,90,0])
54            cylinder(h=30, r1=.8, r2=.8, center=true);
55      rotate([0,0,45])
56          translate([0,radius-2,-2])
57          rotate([0,90,0])
58            cylinder(h=30, r1=.8, r2=.8, center=true);
59      rotate([0,0,135])
60          translate([0,radius-2,-2])
61          rotate([0,90,0])
62            cylinder(h=30, r1=.8, r2=.8, center=true);
63      rotate([0,0,225])
64          translate([0,radius-2,-2])
65          rotate([0,90,0])
66            cylinder(h=30, r1=.8, r2=.8, center=true);
67      rotate([0,0,315])
68          translate([0,radius-2,-2])
69          rotate([0,90,0])
70            cylinder(h=30, r1=.8, r2=.8, center=true);
71      rotate([0,0,45])
72          translate([0,radius-2,2])
73          rotate([0,90,0])
74            cylinder(h=30, r1=.8, r2=.8, center=true);
75      rotate([0,0,135])
76          translate([0,radius-2,2])
77          rotate([0,90,0])
78            cylinder(h=30, r1=.8, r2=.8, center=true);
79      rotate([0,0,225])
80          translate([0,radius-2,2])
81          rotate([0,90,0])
82            cylinder(h=30, r1=.8, r2=.8, center=true);
83      rotate([0,0,315])
84          translate([0,radius-2,2])
85          rotate([0,90,0])
86            cylinder(h=30, r1=.8, r2=.8, center=true);
87
88  }
89  }
90
91  /*
```

```
 * create a container with 350 mul contend and 16 mm side length.
 */
container(7,16);
/*
 * add a cap to the container 15 mm radius and 12 mm heigth.
 */
translate([0,0,10])
    rotate([0,180,0])
        cap(7.25,15,12);
```

7.1.2 casting_forms.scad

This is the script for generating the casting forms (see Fig. 50).

```
$fn = 96;

/*
 * generate the form for the PVS wing form.
 */
module wingform(oside,iside) {
    thick=(oside-iside)/2;
    difference() {
        translate([0, 0, -2])
            cube([oside,oside*1.5,4]);
        translate([thick, thick*1.5, -.01])
            cube([iside,iside*1.5,3]);
        translate([thick+0.5, oside*2-thick, 1])
            rotate([90,0,0])
                cylinder(oside*2,0.5,0.5);
        translate([iside+thick-0.5, oside*2-thick, 1])
            rotate([90,0,0])
                cylinder(oside*2,0.5,0.5);
        translate([-10, thick*1.5+0.5, 1])
            rotate([90,0,90])
                cylinder(oside*2,0.5,0.5);
        translate([-10, thick*1.5+iside*1.5-0.5, 1])
            rotate([90,0,90])
                cylinder(oside*2,0.5,0.5);
    }
}

/*
 * generate the negative for the resin form.
 */
module pvsform(iside) {
    offset=(iside-10)/2;
    difference() {
        translate([-5, -5, 0.05])
            cube([30,40,5]);
        difference() {
```

```
37              translate([-offset*2, 0, 0])
38                  cube([2*iside,30,4]);
39              translate([4.5-offset, 7-offset*1.5, -0.1])
40                  cube([iside+1,iside*1.5+1,5]);
41              translate([2.5-offset, 5-offset*1.5, 2])
42                  cube([iside+5,iside*1.5+5,3]);
43          }
44          translate([0.5, 50, 3.5])
45              rotate([90,0,0])
46                  cylinder(60,0.5,0.5);
47          translate([19.5, 50, 3.5])
48              rotate([90,0,0])
49                  cylinder(60,0.5,0.5);
50          translate([9, 49, 3.5])
51              rotate([90,0,0])
52                  cylinder(20,0.5,0.5);
53          translate([9, 2, 3.5])
54              rotate([90,0,0])
55                  cylinder(10,0.5,0.5);
56          translate([-10, 0.5, 3.5])
57              rotate([90,0,90])
58                  cylinder(60,0.5,0.5);
59          translate([-10, 15, 3.5])
60              rotate([90,0,90])
61                  cylinder(12,0.5,0.5);
62          translate([18, 15, 3.5])
63              rotate([90,0,90])
64                  cylinder(12,0.5,0.5);
65          translate([-10, 29.5, 3.5])
66              rotate([90,0,90])
67                  cylinder(60,0.5,0.5);
68      }
69  }
70
71  /*
72   * for illustration negative of the pvs form.
73   */
74  module symbolic() {
75      translate([40, 40, 0])
76          wingform();
77      rotate([0,0,0])
78          difference(){
79              translate([-4, -4, 0.051])
80                  cube([28,38,4.8]);
81              pvsform();
82      }
83  }
84
85  // create a wing form with outer size 20 and inner size 10.
```

```
86 wingform(20,10);
87 // create a form for the resin curing form negative.
88 // fill this form with PVS to get the resin form.
89 translate([0, -10, 3])
90     rotate([180,0,0])
91         pvsform(10);
```

7.2 Python scripts

7.2.1 analyse_topology.py

This script generates the topological histograms (see Figs. 58 and 59).

```
from math import dist
import numpy as np
import csv
from itertools import combinations

#use nanometer as a base
nano_to_int=1000000000

#add to automatic expanding list
def set_list(l, i, v):
    try:
        l[i] = v
    except IndexError:
        for _ in range(i-len(l)+1):
            l.append(None)
        l[i] = v

#find the highest point in a area 5 by 5 around the center point (x,y)
def higest(height_matrix, x, y):
    result = -10000000
    for xx in range(-2,3):
        for yy in range(-2,3):
            if (x+xx>=0) and (y+yy>=0) and (x+xx < len(height_matrix)) and (y+yy <
 len(height_matrix[0])):
                height = float(height_matrix[x+xx][y+yy])
                result=max(height, result)
    return result

#add a distance to the minimum distances, only the 3 nearest are stored
def set_dist(data,pointnr,current):
    if len(data)>pointnr :
        oldmin1=data[pointnr][0]
        oldmin2=data[pointnr][1]
        oldmin3=data[pointnr][2]
    else:
        oldmin1=1000
        oldmin2=1000
        oldmin3=1000
    if (current<oldmin1):
        oldmin3=oldmin2
        oldmin2=oldmin1
        oldmin1=current
        set_list(data,pointnr,[oldmin1,oldmin2,oldmin3])
    elif (current<oldmin2):
        oldmin3=oldmin2
        oldmin2=current
        set_list(data,pointnr,[oldmin1,oldmin2,oldmin3])
    elif (current<oldmin3):
        oldmin3=current
        set_list(data,pointnr,[oldmin1,oldmin2,oldmin3])

#
# extra: filename.png 16 bit image of the pixel heights
# in: filename.txt ACII version of topological data in nano meter
# in: filename_xy.txt XY coordinates of pillar tops (output Fiji)
# out: filename_normal.txt average and std div of center-center dist and heights
```

```
# out: filename_xy.csv average distance of a pillar to the next 3 rows
# out: filename_z.csv height of the center pillar in comparison to lowes value
#
def analyse_topology(filename):
    height_matrix = []
    with open(filename+'.txt','r') as f:
        reader = csv.reader(f, delimiter='\t')
        for height_row in reader:
            height_matrix.append(height_row)

    minimum = 10000000
    for row in height_matrix:
        for cell in row:
            minimum=min(float(cell),minimum)

    height_list = []
    points = []
    counter = 0
    with open(filename+'_xy.txt','r') as f:
        reader = csv.reader(f, delimiter='\t')
        for row in reader:
            points.append([float(row[0]),float(row[1]),int(counter)])
            counter+=1
            current=higest(height_matrix,int(float(row[1])),int(float(row[0])))-
    minimum
            if (current == 1.3105429e-07):
                print(current)
            height_list.append(current)
    data = []

    for pair in combinations(points,2):
        current=dist([pair[0][0],pair[0][1]], [pair[1][0],pair[1][1]])
        pointnr=pair[0][2]
        set_dist(data,pointnr,current)
        pointnr=pair[1][2]
        set_dist(data,pointnr,current)

    aver=[]
    scale_value=5000.0/len(height_matrix)
    for row in data:
        aver.append(sum(row)*scale_value/len(row))

    with open(filename+'_xy_normal.txt','w') as f:
        writer = csv.writer(f, delimiter=',')
        writer.writerow([str(sum(aver)/len(aver))])
        writer.writerow([str(np.std(aver))])
        writer.writerow([str(len(aver))])
        writer.writerow([str(minimum*nano_to_int)])
        writer.writerow([str(sum(height_list)*nano_to_int/len(height_list))])
        writer.writerow([str(np.std(height_list)*nano_to_int)])

    with open(filename+'_xy.csv','w') as f:
        writer = csv.writer(f, delimiter=',')
        for row in aver:
            writer.writerow([str(row)])

    with open(filename+'_z.csv','w') as f:
        writer = csv.writer(f, delimiter=',')
        for height_elem in height_list:
            writer.writerow([str(height_elem*nano_to_int)])

    # just to check
```

```
117     print(height_list)
118     print(aver)
119
120 # analyze the topology of the following images
121 analyse_topology('/home/ritchie/git/bme-project/afm/dragonfly_0009')
122 analyse_topology('/home/ritchie/git/bme-project/afm/Ks_tapping_5my_2h0000')
123 analyse_topology('/home/ritchie/git/bme-project/afm/Ks_tapping_5my1hz0001')
124 analyse_topology('/home/ritchie/git/bme-project/afm/Ms_tap_wass_5my10000')
125 analyse_topology('/home/ritchie/git/bme-project/afm/
        X903_a_cing_wasse0006_superbild')
126 analyse_topology('/home/ritchie/LiClipse-Workspace/histogram/src/gradient')
127 analyse_topology('/home/ritchie/git/bme-project/afm/211118/abdruck_uv0003')
128 analyse_topology('/home/ritchie/git/bme-project/afm/220308/replic_k_uv_lila_0003')
```

7.2.2 violin_life_dead.py

This script prepares and generates the violin plot from the live-dead (see Figs. 43 to 46).

```
1  # Python program to generate the violin plots
2  import seaborn
3  import pandas as pd
4  import matplotlib
5  import matplotlib.pyplot as plt
6  import importlib
7
8  # generate a violin plot for the cvs file name.
9  def violin_plot(base_dir,name):
10     # set the styles and reset the initial data
11     importlib.reload(matplotlib); importlib.reload(plt); importlib.reload(seaborn)
12     seaborn.set(style="whitegrid")
13     seaborn.set(rc={"figure.dpi":600, 'savefig.dpi':600})
14     seaborn.set(rc={'figure.figsize':(8,3)})
15
16     # read the data sets and select the columns
17     datain = pd.read_csv(base_dir+"/life_dead/"+name+'.csv',sep=',')
18     datain = datain.drop(columns=['randomset','filename'])
19     datain = datain.drop(columns=['hoechst'])
20     datain.rename(columns = {'pi':'dead'}, inplace = True)
21 #     datain.rename(columns = {'live':'live'}, inplace = True)
22
23     # print the distribution data
24     print(name+" mean: ")
25     print(datain.mean())
26     print(name+" std: ")
27     print(datain.std())
28     print(name+" stderr: ")
29     print(datain.sem())
30
31     # reformat the date for the violin plot
32     datain = datain.melt(var_name='type', value_name='count')
33
34     # calculate the violin plot
35     plot = seaborn.violinplot(x="count", y="type", data=datain)
36     plot.set(xlim=(-1, None))
37     plot.set_xlabel("")
38     plot.set_ylabel("")
39     picture=name.replace("/", "_")
40     plot.figure.savefig(base_dir+"/pic/"+picture+".png")
41
42     # store the plot to a png image file.
43     print(base_dir+"/pic/"+picture+".png")
```

```
44
45 # generate all violin plots.
46 base_dir = "/home/ritchie/git/bme-project"
47 violin_plot(base_dir,"a_wing/ecoli_a_wing")
48 violin_plot(base_dir,"m_wing/ecoli_m_wing")
49 violin_plot(base_dir,"scafold/scafold_ecoli")
50 violin_plot(base_dir,"s_m_wing/saureus_m_wing")
51 violin_plot(base_dir,"ks_wing/ks_wing")
52 violin_plot(base_dir,"ref_dead/ecoli_dead_ref")
53 violin_plot(base_dir,"s_ref_dead/saureus_dead_ref")
54 violin_plot(base_dir,"ks_wing_replica/ks_wing_replica")
55 violin_plot(base_dir,"ref_live/ecoli_live_ref")
56 violin_plot(base_dir,"s_ks_wing/saureus_ks_wing")
57 violin_plot(base_dir,"s_ref_life/saureus_life_ref")
58 violin_plot(base_dir,"l_wing/ecoli_l_wing")
59 violin_plot(base_dir,"s_a_wing/saureus_a_wing")
60 violin_plot(base_dir,"s_l_wing/saureus_l_wing")
61 # example gradient
62 violin_plot(base_dir,"live_dead_example")
```

References

[Ada16] Shelley Anne Adamo. "Do insects feel pain? A question at the intersection of animal behaviour, philosophy and robotics". In: *Animal Behaviour* 118 (Aug. 2016), pp. 75–79. DOI: 10.1016/j.anbehav.2016.05.005. URL: https://doi.org/10.1016/j.anbehav.2016.05.005.

[AC01] Matthew J. Arduino and Janice Haney Carr. *Staphylococcus aureus*. en. Page Version ID: 1055768419. Jan. 2001. URL: https://en.wikipedia.org/w/index.php?title=Staphylococcus_aureus&oldid=1055768419 (visited on 10/19/2022).

[Aut+06] Kellar Autumn et al. "Frictional adhesion: a new angle on gecko attachment". In: *Journal of Experimental Biology* 209 (18) (Sept. 2006), pp. 3569–3579. ISSN: 0022-0949. DOI: 10.1242/jeb.02486. eprint: https://journals.biologists.com/jeb/article-pdf/209/18/3569/1256216/3569.pdf. URL: https://doi.org/10.1242/jeb.02486.

[Ban+17] Chaturanga D. Bandara et al. "Bactericidal effects of natural nanotopography of dragonfly wing on *Escherichia coli*". In: *ACS Applied Materials & Interfaces* 9 (8) (2017). PMID: 28139904, pp. 6746–6760. DOI: 10.1021/acsami.6b13666. eprint: https://doi.org/10.1021/acsami.6b13666. URL: https://doi.org/10.1021/acsami.6b13666.

[BB20] David Baracchi and Luigi Baciadonna. "Insect sentience and the rise of a new inclusive ethics". In: *Animal Sentience* 5 (29) (Jan. 2020). DOI: 10.51291/2377-7478.1604. URL: https://doi.org/10.51291/2377-7478.1604.

[BN21] Nina Bauer and Richard W. van Nieuwenhoven. "A.Z.O.O.O. - A zimmer of one's own a phantastic journey into nanostructures". en. In: *ResearchGate* (2021). DOI: 10.13140/RG.2.2.18085.17123. URL: https://rgdoi.net/10.13140/RG.2.2.18085.17123.

[Ben97] Janine Benyus. *Biomimicry : innovation inspired by nature*. New York: Morrow, 1997. ISBN: 978-0-060-53322-9.

[Ber51] G. Bertani. "Studies on lysogenesis I". In: *Journal of Bacteriology* 62 (3) (Sept. 1951), pp. 293–300. DOI: 10.1128/jb.62.3.293-300.1951. URL: https://doi.org/10.1128/jb.62.3.293-300.1951.

[Car21] Janice Haney Carr. *Enterobacteriaceae*. Page Version ID: 215282377. Sept. 2021. URL: https://de.wikipedia.org/w/index.php?title=Enterobacteriaceae&oldid=215282377 (visited on 10/19/2022).

[Cau+20] Abhishek Cauligi et al. "Design and development of a gecko-adhesive gripper for the astrobee free-flying robot". In: *CoRR* abs/2009.09151 (2020). arXiv: 2009.09151. URL: https://arxiv.org/abs/2009.09151.

[Cha+06] Suddhashil Chattopadhyay et al. "Swimming efficiency of bacterium *Escherichia coli*". In: *Proceedings of the National Academy of Sciences* 103 (37) (Sept. 2006), pp. 13712–13717. DOI: 10.1073/pnas.0602043103. URL: https://doi.org/10.1073/pnas.0602043103.

[Chi13] Made in China. *Trade Resources*. Nov. 2013. URL: https://resources.made-in-china.com/article/culture-life/SQandlOcYEiL/Ancient-Chinese-Oiled-Paper-of-Umbrella/ (visited on 11/01/2013).

[22a] *Chitubox, All-in-one SLA/DLP/LCD Slicer-All-in-one SLA/DLP/LCD Slicer - 3D printing preprocessing software*. 2022. URL: https://www.chitubox.com/en/index (visited on 09/05/2022).

[Cia+88] Gaetano Ciancio et al. "Measurement of cell-cycle phase-specific cell death using Hoechst 33342 and propidium iodide: preservation by ethanol fixation." In: *Journal of Histochemistry & Cytochemistry* 36 (9) (Sept. 1988), pp. 1147–1152. DOI: 10.1177/36.9.2457047. URL: https://doi.org/10.1177/36.9.2457047.

[Cle+96] Maarten van Cleef et al. "Polystyrene spheres on mica substrates: AFM calibration, tip parameters and scan artefacts". In: *Journal of Microscopy* 181 (1) (Jan. 1996), pp. 2–9. DOI: 10.1046/j.1365-2818.1996.74351.x. URL: https://doi.org/10.1046/j.1365-2818.1996.74351.x.

[Cor] Olympus Corporation. *Olympusimagejplugin*. URL: https://imagej.net/formats/olympus (visited on 10/19/2022).

[Dar59] Charles Darwin. *On the origin of species by means of natural selection*. or the preservation of favored races in the struggle for life. London: Murray, 1859.

[DG13] Manfred Drack and Ille C. Gebeshuber. "Comment on "Innovation through imitation: biomimetic, bioinspired and biokleptic research" by A. E. Rawlings, J. P. Bramble and S. S. Staniland, Soft Matter, 2012, 8, 6675". In: *Soft Matter* 9 (7) (2013), p. 2338. DOI: 10.1039/c2sm26722e. URL: https://doi.org/10.1039/c2sm26722e.

[Duk08] Reuven Dukas. "Evolutionary biology of insect learning". In: *Annual Review of Entomology* 53 (1) (Jan. 2008), pp. 145–160. DOI: 10.1146/annurev.ento.53.103106.093343. URL: https://doi.org/10.1146/annurev.ento.53.103106.093343.

[Fab75] Johann Christian Fabricius. *Systema entomologiae : sistens insectorvm classes, ordines, genera, species, adiectis synonymis, locis, descriptionibvs, observationibvs / Io. Christ. Fabricii*. In Officina Libraria Kortii, 1775. DOI: 10.5962/bhl.title.36510. URL: https://doi.org/10.5962/bhl.title.36510.

[Feu11] Christian Feuersänger. "Manual for package pgfplots". In: *URL http://www.ctan.org/tex-archive/help/Catalogue/entries/pgfplots.html. Probablement installé dans votre système sous le nom pgfplots.pdf* 17 (2011).

[FCS07] Kathryn M. Fontaine, John R. Cooley, and Chris Simon. "Evidence for paternal leakage in hybrid periodical cicadas (Hemiptera: Magicicada spp.)" In: *PLoS ONE* 2 (9) (Sept. 2007). Ed. by Wim Crusio, e892. DOI: 10.1371/journal.pone.0000892. URL: https://doi.org/10.1371/journal.pone.0000892.

[22b] *GitHub - sn4k3/UVtools: MSLA/DLP, file analysis, calibration, repair, conversion and manipulation*. 2022. URL: https://github.com/sn4k3/UVtools (visited on 09/04/2022).

[Gre78] Tammy Gregersen. "Rapid method for distinction of gram-negative from gram-positive bacteria". In: *European Journal of Applied Microbiology and Biotechnology* 5 (2) (1978), pp. 123–127. DOI: 10.1007/bf00498806. URL: https://doi.org/10.1007/bf00498806.

[Gri15] Ivan V. Grishagin. "Automatic cell counting with ImageJ". In: *Analytical Biochemistry* 473 (Mar. 2015), pp. 63–65. DOI: 10.1016/j.ab.2014.12.007. URL: https://doi.org/10.1016/j.ab.2014.12.007.

[Haa99] Mads Haahr. "random.org: Introduction to randomness and random numbers". In: *Statistics,(June)* (1999), pp. 1–4. URL: ftp://ftp.rediris.org/mirror/CRAN/web/packages/random/vignettes/random-essay.pdf.

[Hal+13] Barry Hall et al. “Growth rates made easy”. In: *Molecular Biology and Evolution* 31 (Oct. 2013). DOI: 10.1093/molbev/mst187.

[HWF20] Hannah G. Hampton, Bridget N. J. Watson, and Peter C. Fineran. “The arms race between bacteria and their phage foes”. In: 577 (7790) (Jan. 2020), pp. 327–336. DOI: 10.1038/s41586-019-1894-8. URL: https://doi.org/10.1038/s41586-019-1894-8.

[Has+12] Jafar Hasan et al. “Selective bactericidal activity of nanopatterned superhydrophobic cicada *Psaltoda claripennis* wing surfaces”. In: *Applied Microbiology and Biotechnology* 97 (20) (Dec. 2012), pp. 9257–9262. DOI: 10.1007/s00253-012-4628-5. URL: https://doi.org/10.1007/s00253-012-4628-5.

[Haw+22] Sara Hawi et al. “Critical review of nanopillar-based mechanobactericidal systems”. In: *ACS Applied Nano Materials* 5 (1) (Jan. 2022), pp. 1–17. DOI: 10.1021/acsanm.1c03045. URL: https://doi.org/10.1021/acsanm.1c03045.

[Hun07] John D. Hunter. “Matplotlib: A 2d graphics environment”. In: *Computing in Science & Engineering* 9 (3) (2007), pp. 90–95. DOI: 10.1109/MCSE.2007.55.

[Iva+12] Elena P. Ivanova et al. “Natural bactericidal surfaces: mechanical rupture of *Pseudomonas aeruginosa* cells by cicada wings”. In: *Small* 8 (16) (June 2012), pp. 2489–2494. DOI: 10.1002/smll.201200528. URL: https://doi.org/10.1002/smll.201200528.

[Iva+13a] Elena P. Ivanova et al. “Bactericidal activity of black silicon”. In: *Nature Communications* 4 (1) (Nov. 2013). DOI: 10.1038/ncomms3838. URL: https://doi.org/10.1038/ncomms3838.

[Iva+13b] Elena P. Ivanova et al. “Molecular organization of the nanoscale surface structures of the dragonfly *Hemianax Papuensis* wing epicuticle”. In: *PLoS ONE* 8 (7) (July 2013). Ed. by Nikolai Lebedev, e67893. DOI: 10.1371/journal.pone.0067893. URL: https://doi.org/10.1371/journal.pone.0067893.

[Iva+17] Elena P. Ivanova et al. “Bactericidal activity of self-assembled palmitic and stearic fatty acid crystals on highly ordered pyrolytic graphite”. In: *Acta Biomaterialia* 59 (Sept. 2017), pp. 148–157. DOI: 10.1016/j.actbio.2017.07.004. URL: https://doi.org/10.1016/j.actbio.2017.07.004.

[KB16] Colin Klein and Andrew B. Barron. “Insects have the capacity for subjective experience”. In: *Animal Sentience* 1 (9) (July 2016). DOI: 10.51291/2377-7478.1113. URL: https://doi.org/10.51291/2377-7478.1113.

[LFL10] Marie-Claude Larivière, Murray J. Fletcher, and André Larochelle. *Auchenorrhyncha (Insecta: Hemiptera): catalogue.* Vol. 63. 2010, p. 232. ISBN: 978-0-478-34720-3. URL: https://www.landcareresearch.co.nz/publications/fauna-of-new-zealand-series/.

[MCL84] James I. Mangels, Mike E. Cox, and Lois H. Lindberg. “Methanol fixatfion an alternative to heat fixation of smears before staining”. In: *Diagnostic Microbiology and Infectious Disease* 2 (2) (Apr. 1984), pp. 129–137. DOI: 10.1016/0732-8893(84)90008-7. URL: https://doi.org/10.1016/0732-8893(84)90008-7.

[MAT20] MATLAB. *Matlab version R2020b.* Natick, Massachusetts: The MathWorks Inc., 2020.

[Men07] M. J. Mendell. "Indoor residential chemical emissions as risk factors for respiratory and allergic effects in children: a review". In: *Indoor Air* 17 (4) (Aug. 2007), pp. 259–277. DOI: 10.1111/j.1600-0668.2007.00478.x. URL: https://doi.org/10.1111/j.1600-0668.2007.00478.x.

[Mer82] Connie Lange Merrill. "Biomimicry of the dioxygen active site in the copper proteins hemocyanin and cytochrome oxidase". PhD thesis. Houston, Texas, USA: Rice University, 1982. URL: https://hdl.handle.net/1911/15707.

[Mes55] George DE. Mestral. "Velvet type fabric and method of producing same". 2717437. Sept. 1955. URL: https://www.freepatentsonline.com/2717437.html (visited on 10/19/2022).

[Mic15] Joe Micallef. "Advanced techniques using blender". In: *Beginning Design for 3D Printing*. Apress, 2015, pp. 367–390. DOI: 10.1007/978-1-4842-0946-2_12. URL: https://doi.org/10.1007/978-1-4842-0946-2_12.

[Mut+17] Thirumahal Muthukrishnan et al. "Evaluating the reliability of counting bacteria using epifluorescence microscopy". In: *Journal of Marine Science and Engineering* 5 (1) (Jan. 2017), p. 4. DOI: 10.3390/jmse5010004. URL: https://doi.org/10.3390/jmse5010004.

[NK12] David Nečas and Petr Klapetek. "Gwyddion: an open-source software for SPM data analysis". In: *Open Physics* 10 (1) (Jan. 2012). DOI: 10.2478/s11534-011-0096-2. URL: https://doi.org/10.2478/s11534-011-0096-2.

[NSS22] Kirti Nirmal, Vikas Saini, and Narendra Pal Singh. "Antibacterial resistance menace: a global cause of concern?" In: *International Journal of Clinical Science and Medical Research* 2 (9) (Sept. 2022), pp. 71–77. DOI: 10.55677/IJCSMR/V2I9-01/2022. URL: http://journalofmedical.org/index.php/ijcsmr/article/view/26.

[Rom+20] Jessica Román-Kustas et al. "Molecular and topographical organization: influence on cicada wing wettability and bactericidal properties". In: *Advanced Materials Interfaces* 7 (10) (Apr. 2020), p. 2000112. DOI: 10.1002/admi.202000112.

[RB59] William Moy Stratton Russell and Rex Leonard Burch. *The principles of humane experimental technique*. en. Methuen, 1959. ISBN: 1441412697. URL: https://books.google.at/books?id=j75qAAAAMAAJ.

[Sch+12] Johannes Schindelin et al. "Fiji: an open-source platform for biological-image analysis". en. In: *Nat. Methods* 9 (7) (June 2012), pp. 676–682.

[Sch69] Otto H Schmitt. "Some interesting and useful biomimetic transforms". In: *Third Int. Biophysics Congress*. Vol. 1069. 1969, p. 197.

[Sci21a] Thermo Fisher Scientific. *BestProtocols: Viability staining protocol for flow cytometry*. Dec. 2021. (Visited on 10/19/2022).

[Sci21b] Thermo Fisher Scientific. *Invitrogen™ Hoechst 33258 manual*. Dec. 2021. (Visited on 10/19/2022).

[Sen+21] Senevirathne W. M. A. I. Senevirathne et al. "Bactericidal efficiency of micro- and nanostructured surfaces: a critical perspective". In: *RSC Advances* 11 (3) (2021), pp. 1883–1900. DOI: 10.1039/d0ra08878a. URL: https://doi.org/10.1039/d0ra08878a.

[Sha05] Yakov Shafranovich. *Common format and MIME type for comma-separated values (CSV) files*. RFC 4180. RFC Editor, Oct. 2005. URL: https://www.rfc-editor.org/rfc/rfc4180.txt.

[Tan19] Till Tantau. *The TikZ and PGF packages. Manual for version 3.1.1.* Feb. 2, 2019. URL: http://sourceforge.net/projects/pgf/.

[TSG96] Vigdis Torsvik, R. Sørheim, and J. Goksøyr. "Total bacterial diversity in soil and sediment communities - A review". In: *Journal of Industrial Microbiology & Biotechnology* 17 (3-4) (Sept. 1996), pp. 170–178. DOI: 10.1007/bf01574690. URL: https://doi.org/10.1007/bf01574690.

[VD09] Guido Van Rossum and Fred L. Drake. *Python 3 reference manual.* Scotts Valley, CA: CreateSpace, 2009. ISBN: 1441412697.

[Vin01] Julian F. V. Vincent. "Stealing ideas from nature". In: *Deployable structures.* Springer Vienna, 2001, pp. 51–58. DOI: 10.1007/978-3-7091-2584-7_3. URL: https://doi.org/10.1007/978-3-7091-2584-7_3.

[Vin+06] Julian F.V Vincent et al. "Biomimetics: its practice and theory". In: *Journal of The Royal Society Interface* 3 (9) (Apr. 2006), pp. 471–482. DOI: 10.1098/rsif.2006.0127. URL: https://doi.org/10.1098/rsif.2006.0127.

[Vin80] Leonardo da Vinci. *Leonardo da Vinci: Flying machine.* 1480. URL: https://www.codex-atlanticus.it/#/Detail?detail=858 (visited on 10/19/2022).

[WNB96] Thomas Wagner, Christoph Neinhuis, and Wilhelm Barthlott. "Wettability and contaminability of insect wings as a function of their surface sculptures". In: *Acta Zoologica* 77 (3) (July 1996), pp. 213–225. DOI: 10.1111/j.1463-6395.1996.tb01265.x. URL: https://doi.org/10.1111/j.1463-6395.1996.tb01265.x.

[Was21] Michael L. Waskom. "seaborn: statistical data visualization". In: *Journal of Open Source Software* 6 (60) (2021), p. 3021. DOI: 10.21105/joss.03021. URL: https://doi.org/10.21105/joss.03021.

[WCW10] Gregory S. Watson, Bronwen W. Cribb, and Jolanta A. Watson. "How micro/-nanoarchitecture facilitates anti-wetting: An elegant hierarchical design on the termite wing". In: *ACS Nano* 4 (1) (Jan. 2010), pp. 129–136. DOI: 10.1021/nn900869b. URL: https://doi.org/10.1021/nn900869b.

[Wat+08] Gregory S. Watson et al. "Putative functions and functional efficiency of ordered cuticular nanoarrays on insect wings". In: *Biophysical Journal* 94 (8) (Apr. 2008), pp. 3352–3360. DOI: 10.1529/biophysj.107.109348. URL: https://doi.org/10.1529/biophysj.107.109348.

[Zha+15] Xuelin Zhang et al. "Comparing Two Functions for Optical Density and Cell Numbers in Bacterial Exponential Growth Phase". In: *Journal of Pure and Applied Microbiology* 9 (Mar. 2015), pp. 299–305.

[Zob18] Sigrid Zobl. *Strukturfarben im Brennpunkt der Bionik Zwischen Kunst und Naturwissenschaften.* Wiesbaden: Springer Fachmedien Wiesbaden, 2018. ISBN: 978-3-658-20803-5.